



저작자표시-비영리-변경금지 2.0 대한민국

이용자는 아래의 조건을 따르는 경우에 한하여 자유롭게

- 이 저작물을 복제, 배포, 전송, 전시, 공연 및 방송할 수 있습니다.

다음과 같은 조건을 따라야 합니다:



저작자표시. 귀하는 원저작자를 표시하여야 합니다.



비영리. 귀하는 이 저작물을 영리 목적으로 이용할 수 없습니다.



변경금지. 귀하는 이 저작물을 개작, 변형 또는 가공할 수 없습니다.

- 귀하는, 이 저작물의 재이용이나 배포의 경우, 이 저작물에 적용된 이용허락조건을 명확하게 나타내어야 합니다.
- 저작권자로부터 별도의 허가를 받으면 이러한 조건들은 적용되지 않습니다.

저작권법에 따른 이용자의 권리는 위의 내용에 의하여 영향을 받지 않습니다.

이것은 [이용허락규약\(Legal Code\)](#)을 이해하기 쉽게 요약한 것입니다.

[Disclaimer](#)

공학박사 학위논문

Investigation on Li-ion Transport
in Ionic Liquids and
Polyelectrolytes by Polarizable
Molecular Dynamics Simulations

편극성 분자동역학 시뮬레이션을 이용한 이온성
액체 및 고분자 전해질내 리튬 이온 수송에 관한
분석

2022 년 8 월

서울대학교 대학원

화학생물공학부

김 슬 우

Investigation on Li-ion Transport in Ionic Liquids and Polyelectrolytes by Polarizable Molecular Dynamics Simulations

지도 교수 이 원 보

이 논문을 공학박사 학위논문으로 제출함
2022 년 8 월

서울대학교 대학원
화학생물공학부
김 슬 우

김슬우의 공학박사 학위논문을 인준함
2022 년 6 월

위 원 장 _____ 이 규 태 _____ (인)

부위원장 _____ 이 원 보 _____ (인)

위 원 _____ 남 재 욱 _____ (인)

위 원 _____ 김 소 연 _____ (인)

위 원 _____ 허 준 _____ (인)

Abstract

Investigation on Li-ion Transport in Ionic Liquids and Polyelectrolytes by Polarizable Molecular Dynamics Simulations

Seulwoo Kim
School of Chemical and Biological Engineering
The Graduate School
Seoul National University

The demands on the research area relevant to lithium-ion batteries are tremendously increased in recent days, and many studies have been conducted intensively and extensively to develop batteries with good performance, where the meaning of good performance ranges from electrical functionality to stability. Electrolytes, one of the crucial components in batteries, are the key materials to determine the performance of a battery. Liquid electrolytes have high ionic conductivities but poor stability both chemically and mechanically. On the other hand, solid electrolytes have no concern about stability, such as hydrolysis or leakage problems, but they have poor electrical conductivities. Therefore, developing novel electrolytes for lithium-ion batteries requires a deep understanding of both structural and dynamical aspects.

Polarizable molecular dynamics (MD) simulation is well known to describe precisely the behavior of electrolytes for lithium-ion batteries. Especially, a force field based on the induced point dipole model, called APPLE&P force field, is suitable for predicting the dynamics of lithium ions in the electrolytes with room temperature ionic liquids or polyelectrolytes compared to any other force fields. In this context, it is worthy to use the model despite the massive computational cost of

polarizable MD simulations because other models show poor simulation results to explain the electrolytes.

In this dissertation, lithium-ion transport mechanism in the electrolytes based on ionic liquids was investigated by many-body polarizable MD simulations with the APPLE&P force field. Both structural and dynamic properties were studied to elucidate ion transport mechanism in the two representative electrolytes: One was the electrolytes with nanopores, where poly-(ethylene oxide) (PEO) chains are branched, and ionic liquids ([1-butyl-1-methylpyrrolidinium][bis(trifluoromethanesulfonyl)imide], $\text{PYR}_{14}\text{TFSI}$) are filled; and the other was the ionic liquids electrolytes with zwitterions, a compound of covalent bonded PYR_{14} and TFSI as an additive. A thorough investigation was conducted to elucidate coordination structures of lithium-ion in the electrolytes via pair distribution function and cluster analysis. The third component of each electrolyte altered the structural properties, and the change influenced lithium-ion dynamics. In the nanopores, the presence of PEO chains suppressed $[\text{LiTFSI}_3]^{-2}$ clusters, and the new dominated clusters, $[\text{LiTFSI}_2]^{-}$ enable more lithium-ion transport by structural diffusion mechanism. With the zwitterions, the performance of the electrolytes with ionic liquids was improved because of their unique characteristics. For $\text{LiTFSI}/\text{PYR}_{14}\text{TFSI}$ binary electrolytes with zwitterions, the activation energy for the diffusion coefficients of lithium-ion was decreased hence the dynamics of lithium-ion was enhanced by more frequent anion exchange. This advantage was effective to some concentration and limited to specific anions. Accordingly, the optimal conditions were evaluated in this study.

In order to overcome the high computational cost of implementing induced dipole models, OpenMM software package was modified. Code transplant was

conducted to develop a new plugin for OpenMM, which enables to running of precise and swift MD simulations with the APPLE&P force fields.

Keywords: Lithium-ion Battery; Polarizable Force Field; Molecular Dynamics Simulation; Ionic Liquids; Polyelectrolytes; Transport Mechanism

Student Number: 2016-21012

Table of Contents

ABSTRACT	I
LIST OF FIGURES	VI
LIST OF TABLES	X
CHAPTER 1. INTRODUCTION	1
CHAPTER 2. THEORETICAL BACKGROUNDS	6
2.1. CHARGE MODELS FOR ELECTROLYTE SYSTEMS	6
2.1.1. Non-polarizable Molecular Model.....	7
2.1.2. Polarizable Molecular Model.....	9
2.2. Li^+ TRANSPORT MECHANISM IN ELECTROLYTES	14
2.2.1. Li^+ Transport in Ionic Liquids.....	15
2.2.2. Li^+ Transport in poly-(ethylene oxide).....	17
CHAPTER 3. TRANSPORT MECHANISM OF LI- ION IN POLYMER BRANCHED NANOPORES	19
3.1. COMPUTATIONAL METHOD	19
3.1.1 Polarizable Molecular Dynamics Simulation	19
3.2. STRUCTURAL PROPERTIES.....	23
3.2.1. First Coordination Shell of Li^+	24
3.2.2. Li-TFSI complex.....	35
3.3. TRANSPORT PROPERTIES	41
3.3.1. Diffusion Coefficient	41
3.3.2. Ionic Conductivity	45
3.4. LI ION TRANSPORT MECHANISM.....	49
3.4.1. Residual Time of Li^+ ions	49
3.4.2. Single Ion Trajectory Analysis.....	53
3.5. CONCLUSION.....	59
CHAPTER 4. LI- ION DYNAMICS IN IONIC LIQUIDS WITH ZWITTERION ADDITIVES	61
4.1. MATERIALS	62
4.1.1. Chemical Information	62
4.1.2. Procedure to Fit New Force Parameters	64
4.2. COMPUTATIONAL METHOD	69
4.2.1. Modification of OpenMM Software Package.....	69
4.2.2. Polarizable Molecular Dynamics Simulation	71
4.3. STRUCTURAL PROPERTIES.....	71
4.3.1. Density of the Electrolytes.....	72
4.3.2. Pair Distribution Functions	74
4.3.3. Net charge of ion clusters	81
4.4. TRANSPORT MECHANISM.....	90
4.4.1. Ion Coordination and Transport Mechanism	90

4.4.2. Diffusion Coefficient and Conductivity.....	94
4.4.3. Rotational Relaxation.....	102
4.5. CONCLUSION.....	109
CHAPTER 5. CONCLUDING REMARKS	111
5.1. SUMMARIZE OF STUDY	111
5.2. LIMITATION AND FUTURE WORKS.....	112
BIBLIOGRAPHY	114
요약 (국문초록).....	119

List of Figures

Figure 2-1. Correlation between polarizable simulation and their scale factors. [Schróder, 2012]	8
Figure 2-2. A schematic drawing of the induced point dipole model.	11
Figure 2-3. Illustration of two diffusion mechanisms of Li^+ with TFSI anions in ionic liquids: (a) Structural diffusion, and (b) Vehicular diffusion.	16
Figure 2-4. Coordination structures of Li^+ with oxygens of TFSI anions: (a) Mono dentate, and (b) Bidentate.	16
Figure 3-1. A schematic draw of the PEO_xLi_y systems for molecular dynamics simulations and visualizations.	21
Figure 3-2. Uniform fluid distribution functions according to the direction of pair vectors between ideal fluids obtained by Monte Carlo simulations for the corresponding geometries of PEO_xLi_y .	26
Figure 3-3. Heatmaps of angle-dependent radial distribution functions at 423 K for all PEO_xLi_y systems: (a) $g^{\text{Li}^+-\text{N}_{\text{TFSI}}}(r, \theta)$, (b) $g^{\text{Li}^+-\text{Li}^+}(r, \theta)$.	28
Figure 3-4. Angle-dependent radial distribution functions in longitudinal ($\theta = 0^\circ$) and radial ($\theta = 90^\circ$) directions: (a) $g^{\text{Li}^+-\text{N}_{\text{TFSI}}}(r, \theta)$, (b) $g^{\text{Li}^+-\text{Li}^+}(r, \theta)$.	29
Figure 3-5. Angle-dependent radial distribution functions $g^{\text{Li}^+-\text{O}_{\text{PEO}}}(r, \theta)$ for all systems at (a) 423, (b) 393, and (c) 363 K. (d) The magnitudes of the first peaks of $g^{\text{Li}^+-\text{O}_{\text{PEO}}}(r, \theta)$ as a function of θ .	30
Figure 3-6. Angle-dependent radial distribution functions at 393 K (a–d) and 363 K (e–h) for all systems. (a, e) Heatmaps for $g^{\text{Li}^+-\text{N}_{\text{TFSI}}}(r, \theta)$ (b, f) $g^{\text{Li}^+-\text{N}_{\text{TFSI}}}(r, \theta)$, in longitudinal and radial directions. Left: the large systems, right: the small systems. (c, g) Heatmaps for $g^{\text{Li}^+-\text{Li}^+}(r, \theta)$ (d, h) $g^{\text{Li}^+-\text{Li}^+}(r, \theta)$ in longitudinal and radial directions. Left: the large systems, right: the small systems.	31
Figure 3-7. Angle-dependent radial distribution functions $g^{\text{N}_{\text{TFSI}}-\text{N}_{\text{PYR}}}(r, \theta)$ for all systems at (a, d) 423 K, (b, e) 393 K, and (c, f) 363 K. (a–c) Heatmaps for $g^{\text{N}_{\text{TFSI}}-\text{N}_{\text{PYR}}}(r, \theta)$ and (d–f) $g^{\text{N}_{\text{TFSI}}-\text{N}_{\text{PYR}}}(r, \theta)$ in longitudinal and radial directions. Left: the large systems, right: the small systems.	32
Figure 3-8. Fraction of $[\text{Li}_x(\text{TFSI})_n]^{(n-x)}$ complexes in each group divided into the number of attached PEO chains from the result of cluster analysis at 423 K. The inner pie charts exhibit the number of Li^+ ions of each group, and the yellow outer pie charts exhibit the number of attached TFSI anions to Li^+ ions in each group. The color of each group distinguishes each percentage within rectangles; Red: Li^+ ions totally coordinated with TFSI anions, Blue: Li^+ ions coordinated to 1 PEO chain, and Green: Li^+ ions coordinated to 2 PEO chains. (a) $\text{PEO}_{12}\text{Li}_{160}$ (b) $\text{PEO}_6\text{Li}_{130}$	

c) PEO ₁₂ Li ₄₀ (d) PEO ₆ Li ₂₀ (e) Binary electrolyte.	37
Figure 3-9. Five Representative structures that Li ⁺ ions could have in PEO _x Li _y electrolytes. Fluorene, hydrogen, and electron lone pairs are now shown in this figure. (a) [LiTFSI ₂] ⁻ . Two bidentate structures comprise the complex. (b) [LiTFSI ₃] ⁻ . Two bidentate and one monodentate structure comprise the complex. (c) The Li ⁺ ion totally coordinated with a PEO chain. Almost six EOs are surrounding the Li ⁺ ion. (d) The Li ⁺ ion coordinated with one PEO chain and one TFSI ⁻ anion. Four EOs and one oxygen atom of a TFSI anion are surrounding the Li ⁺ ion. The TFSI ⁻ anion forms a monodentate structure. (e) The Li ⁺ ion coordinated with one PEO chain and two TFSI anions. Two EOs and three oxygen atoms of TFSI anions are surrounding the Li ⁺ ion. The TFSI anions form one monodentate and one bidentate structure, respectively. The PEO chain is almost linear.	38
Figure 3-10. Fraction of monodentate structure compared to bidentate structure for all systems as well as binary electrolyte from the result of cluster analysis.	40
Figure 3-11. Longitudinal diffusion coefficients as a function of temperature for all systems as well as binary electrolytes. Note that the values for binary electrolytes are isotropic diffusion coefficients.	43
Figure 3-12. Mean square displacement of Li ⁺ ions in PEO _x Li _y electrolytes categorized by their coordination site: Black – with TFSI, Red – with 1 PEO, and Blue – with 2 PEO.	44
Figure 3-13. Longitudinal ionic conductivities of solution (dashed lines) and Li ⁺ ions (solid lines) as a function of temperature. Note that the values for binary electrolytes are isotropic conductivities.	48
Figure 3-14. Normalized autocorrelation function of neighbor function of Li ⁺ -PEO (purple lines) and Li ⁺ -TFSI (cyan lines) for all systems; Top: PEO ₁₂ Li ₆₀ and PEO ₆ Li ₃₀ , Bottom: PEO ₁₂ Li ₄₀ and PEO ₆ Li ₂₀ . Each pair in the same figures have the same relative amount of Li ⁺ ions to PEO chains.	51
Figure 3-15. Residual times for Li ⁺ ions to PEO chains (dashed lines) and TFSI anions (solid lines) as a function of temperature for all systems as well as binary electrolytes.	52
Figure 3-16. Probability distribution of displacement of Li ions (a–d) in PEO _x Li _y systems along the longitudinal direction and (e) binary electrolyte.	54
Figure 3-17. Coordination maps for the representative of (a) fast and (b) slow Li ⁺ ions in the PEO ₁₂ Li ₆₀ system at 423 K. (c) Coordination map for the fastest ion in the binary electrolyte at 423 K.	56
Figure 3-18. Probability distributions for radial density of Li ⁺ ions in nanopores at 423 K. <i>r</i> = 0.0 means the ions are located at the center of nanopores. 10 fastest and slowest ions were used in averaging for the large systems (PEO ₁₂ Li ₆₀ and PEO ₁₂ Li ₄₀), and 5 ions were used for the small systems (PEO ₆ Li ₃₀ and PEO ₆ Li ₂₀).	58
Figure 4-1. An illustration of anions used in the present chapter: (a) bis(trifluorom	

ethanesulfonyl)imide (TFSI), (b) bis(fluorosulfonyl)imide (FSI).	63
Figure 4-2. (a) Chemical structure and information of the zwitterion. (b), (c) Illustrations of the zwitterion conformers used in partial charge optimization. The anionic functional group forms: (b) <i>cis</i> conformer and (c) <i>trans</i> conformer.	63
Figure 4-3. (a) Information about missing force parameters. (b), (c) Torsional potential of NSCH and NSCC, respectively, which parameters fitted to the results of <i>ab initio</i> calculation.	68
Figure 4-4. Benchmark and validation results for the modified OpenMM: (a) Benchmark result and information (b) Comparison of radial distribution functions of Li-X and PYR ₁₄ -X	70
Figure 4-5. Density of the electrolytes as the function of temperatures. Left: LTz, and Right: LFz.	73
Figure 4-6. Radial distribution functions between Li ⁺ ions to other molecules in LTz electrolytes. Insets: Radial distribution functions between Li ⁺ ions to zwitterions.	76
Figure 4-7. Radial distribution function between Li ⁺ ions to other molecules in LFz electrolytes. Insets: Radial distribution functions between Li ⁺ ions to zwitterions.	77
Figure 4-8. Ratio of second peaks to first peaks of radial distribution functions of Li-TFSI (solid lines) and Li-FSI (dashed lines). The grey line indicates that the two peaks are identical.	79
Figure 4-9. Radial distribution functions of Li-Li at 423 K for LTz electrolytes (Left) and LFz (Right) electrolytes.	80
Figure 4-10. Probability distribution array of a_{ij} for [Li _x TFSI _n] ^(n-^x) clusters in LTz electrolytes at 423 K.	83
Figure 4-11. Probability distribution array of a_{ij} for [Li _x TFSI _n] ^(n-^x) clusters in LTz electrolytes at 393 K.	83
Figure 4-12. Probability distribution array of a_{ij} for [Li _x TFSI _n] ^(n-^x) clusters in LTz electrolytes at 363 K.	84
Figure 4-13. Probability distribution array of a_{ij} for [Li _x TFSI _n] ^(n-^x) clusters in LTz electrolytes at 333 K.	84
Figure 4-14. Probability distribution array of a_{ij} for [Li _x FSI _n] ^(n-^x) clusters in LFz electrolytes at 423 K.	85
Figure 4-15. Probability distribution array of a_{ij} for [Li _x FSI _n] ^(n-^x) clusters in LFz electrolytes at 393 K.	85
Figure 4-16. Probability distribution array of a_{ij} for [Li _x FSI _n] ^(n-^x) clusters in LFz electrolytes at 363 K.	86
Figure 4-17. Probability distribution array of a_{ij} for [Li _x FSI _n] ^(n-^x) clusters in LFz electrolytes at 333 K.	86
Figure 4-18. Average size and net charge of [Li _x TFSI _n] ^(n-^x) clusters as the function of the number of zwitterions in LTz electrolytes.	88
Figure 4-19. Average size and net charge of [Li _x FSI _n] ^(n-^x) clusters as the function of the number of zwitterions in LFz electrolytes.	89
Figure 4-20. Normalized autocorrelation function of neighbor function at 423 K of Li-TFSI of Li FSI (red lines) and Li-Zwitterions (black lines) for LTz and LFz electrolytes; Left: LTz electrolytes	

, Right: LFz electrolytes.	93
Figure 4-21. Diffusion coefficients as a function of temperatures for each component. Left: LTz, and Right: LFz.	97
Figure 4-22. Activation energies for diffusions of Li^+ ions. Left: LTz, and Right: LFz.	98
Figure 4-23. Ionic conductivities of electrolytes and Li ions for LTz electrolytes	100
Figure 4-24. Ionic conductivities of electrolytes and Li ions for LFz electrolytes	101
Figure 4-25. Representative vectors of TFSI, FSI, PYR ₁₄ , and zwitterion to calculate the second order Legendre polynomials	104
Figure 4-26. Second order Legendre polynomial of each component in LTz electrolytes as temperatures and the fraction of zwitterions.	105
Figure 4-27. Second order Legendre polynomial of each component in LTz electrolytes as temperatures and the fraction of zwitterions.	106

List of Tables

Table 3-1. System information for MD simulations of PEO _x Li _y systems.	22
Table 3-2. Running coordination numbers from MD simulations of PEO _x Li _y systems. The values were determined near the end of the first coordination shells from the results of radial distribution functions.....	34
Table 3-3. Degrees of ion dissociation of each system	47
Table 4-1. Partial charge set optimized by induced point dipole polarization mode 1	66
Table 4-2. The degree of ion dissociation for LTz electrolytes.....	100
Table 4-3. The degree of ion dissociation for LFz electrolytes	101

Chapter 1. Introduction

Lithium-ion secondary batteries (LIBs) have been adopted for many applications ranging from portable electronic devices to electric vehicles. This is why they have been extensively and intensively investigated in recent decades [1–6]. Electrolytes are one of the key components of a battery system because the choice of electrolyte determines the performance of LIBs in electrical aspects [7–9]. Recently, the significance of mechanical properties has been pronounced in evaluating electrolytes with the advent of solid electrolytes [10]. A good electrolyte exhibits the following characteristics: high electrical conductivity, high cationic transference number, and high chemical and mechanical stability. The last feature is related to how much degradation of electrolytes near electrodes or the formation of Li^+ dendrite is suppressed [11]. In liquid electrolytes, a protective film called SEI (solid electrolyte interphase) can prevent such catastrophe, whereas this problem is insignificant in solid electrolytes. In this respect, many kinds of electrolytes have been suggested and studied, from simple liquid electrolytes to complex solid electrolytes.

Since the first commercial LIB was fabricated with LiPF_6 salt and ethylene carbonate (EC) in the 1990s, organic solvents based on carbonate groups have been commonly used until recent days because of their high electrical conductivities. However, the critical drawbacks relevant to stability issues, such as hydrolysis, leakage of liquids, or flammability, resulted in the exploration into next-generation electrolytes. One solution was suggested to use room temperature ionic liquids (RTILs) as electrolytes of LIBs. RTILs have been used in the extensive area of research as solvents because of their unique properties [12,13]; viscous, non-volatile, and non-flammable, but it is recent to be used in electrochemical systems [14].

Various combinations of many anions and cations are possible [7]. Anions with fluorene-based functional groups such as PF₆, bis(fluorosulfonyl)imide (FSI), or bis(trifluoromethanesulfonyl)imide (TFSI) are commonly used due to charge delocalization, and cations of cyclic ammonium with alkyl chains such as imidazolium (C_xC_yIm⁺), pyrrolidinium (PYR) are generally used. Even though the electrical conductivities of LIB with ionic liquid solvents are lower than those of organic solvents, the use of the materials is considerable because of the advantages which come from their high stabilities.

Polyelectrolytes also have been studied broadly to replace previous liquid electrolytes because of their good mechanical properties producing stable battery operations compared to liquid electrolytes [15,16]. Poly-(ethylene oxide) (PEO) has been broadly used because of its flexibility and safety. Polyelectrolytes also have relatively low electrical conductivities, hence researchers introduced various treatments to improve battery performance. Interestingly, it was found that the performance of LIB based on PEO electrolytes was improved when RTIL was introduced as an additive by Passerini and coworkers [17]. They suggested RTIL assisted in accelerating the dynamics of the ethylene oxide as a plasticizer without changing the transport mechanism or interaction with Li⁺ ions. Yang and coworkers also used ceramic fillers in their battery, which was based on PEO doped with LiTFSI salt, to increase both ionic conductivity and electrochemical stability window [18,19]. Recently, polyelectrolytes prepared using microphase separation have been suggested to enhance both ionic conductivities and mechanical properties [20,21]. Anh and Kim developed a thermally and mechanically stable polyelectrolyte membrane as an example. The polyelectrolyte was composed of a matrix domain and ion channels, which were constructed by microphase separation. The matrix

maintained its structural strength, and ion channels allowed fast Li-ion transport [22]. In order to enhance mechanical properties and chemical windows of LIBs, zwitterionic ionic liquids (zwitterions) were included in electrolytes with ionic liquids or polyelectrolytes [23,24].

It is important to understand ion correlations in electrolytes to elucidate the dynamics of Li^+ ions because they never move alone but with correlated to other molecules like solvents or anions. However, it is not clear to investigate detailed phenomena related to ion transport or correlations on an atomic scale by experiments alone. Recent advances in computational power have allowed *ab initio* calculations on Li^+ ions with electrolytes, and many studies have supported the idea of experiments. Still, *ab initio* calculations have problems in terms of the lack of understanding of dynamic behavior and the requirement of massive computational power for complex systems, and these problems can be solved by molecular dynamics (MD) simulations. MD simulations have been extensively used to understand the molecular behaviors of electrolyte systems [25–28]. In MD simulations for electrolyte systems, one additional concept should be considered, ‘polarization’. The polarization is ignored in most cases of MD simulations, and the error from it is trivial to predict thermodynamic or kinetic observations. However, for dielectric molecules, such as electrolytes, the significance of the polarization is raised in that the electrostatic interactions become prominent. In this context, many charge models are suggested, and the details are discussed in the following chapter. In early 2000s, Padua and Lopes developed a force field, called CL&P for several RTILs based on the OPLS-AA force field hence many researchers conducted their studies on electrolytes with RTILs with the force field [29]. Advanced molecular charge models to consider polarization were subsequently applied to MD simulations

to more precisely predict the properties of electrolytes, called polarizable molecular models. Borodin and Smith developed a force field named APPLE&P based on Applequist's induced point dipole models with Thole screening function [30]. With the force field, Borodin and coworkers investigated many electrolyte systems with RTIL, polymers, and even organic solvents in their extensive studies [31,32]. Maitra and Heuer suggested a quantitative Li ion transport model in PEO electrolytes [33], and Diddens extended the research with various additives [34,35].

In this dissertation, polarizable MD simulations with the APPLE&P force field are conducted to precisely investigate Li^+ transport in a polyelectrolyte and RTILs with zwitterions, respectively. The first system of polyelectrolytes consists of LiTFSI/PYR₁₄TFSI solution in PEO branched nanopores, which seem to be similar to the ion channels designed by Anh and Kim. In order to elucidate Li^+ transport phenomena in the nanopores, the local environment of Li^+ ions is investigated quantitatively as well as transport properties. Single ion trajectory analysis, an imperative procedure for revealing the atomistic behaviors of various systems [36], was also performed to determine the transport mechanism from the perspective of thermodynamics and kinetics. In the second system, binary electrolytes^① of different anions with zwitterions are investigated by polarizable MD simulations conducted by an in-house modified OpenMM software package. The modification enabled one to faster implement MD simulations with the APPLE&P force field by GPU. The influence of the zwitterions is elucidated by structural and dynamical analysis, and the evaluation suggests an optimal condition of the electrolytes.

The outline of this dissertation is following: In Chapter 1, research motivation

^① Composed of Li^+ salts and ionic liquids, such as LiTFSI/PYR₁₄TFSI

and several previous studies are presented; Chapter 2 introduces theoretical backgrounds to help understand this dissertation; Chapter 3 presents the research about polarizable MD simulations for LiTFSI/PYR₁₄TFSI in PEO branched nanopores, and the readers can find the related publication in *Battery Energy 2022, 1, 2, 20210013* [37]; Chapter 4 presents the research about polarizable MD simulations for binary electrolytes (LiTFSI/PYR₁₄TFSI and LiFSI/PYR₁₄FSI) with varied fractions of zwitterion additives, which will be published in the future; and finally overall conclusive remarks are given in Chapter 5.

Chapter 2. Theoretical Backgrounds

2.1. Charge Models for Electrolyte Systems

As mentioned in the previous chapter, there are many charge models to describe electrostatic interaction between electrolytes for MD simulations. Though a recent review paper introduced the models in detail [38], here a brief summary is presented to help understand the concept of polarizable force fields.

The multipole expansion of electrostatic potential is following:

$$V(r) = \frac{1}{4\pi\epsilon_0 r} \int_{V'} \rho(r') \left(1 - \frac{\hat{r} \cdot r'}{r} + \frac{1}{2r^2} (3(r \cdot r')^2 - r'^2) + O\left(\frac{r'}{r}\right)^3 \right) dV' \quad (1)$$

, where the first term in parentheses is called the monopole moment, the second term is called the dipole moment, the third term is called the quadrupole moment, and the higher terms (octopole, hexadecapole, and ...) are skipped. The electrostatic potential of classical MD simulations discards the higher terms than the monopole moment to calculate potentials and forces between two atoms, and the monopoles are approximated to constant point charges. The approximation is enough to predict various observations of many complex systems, but not for the systems comprised of high dielectric molecules such as electrolytes because this ignores polarization effects including charge transfer. This results in an overestimation of electrostatic interactions, and the dynamics of the systems are significantly decreased compared to those of reality. Non-polarizable molecular models are based on the method of modifying force parameters to resolve the problem without further calculation. In contrast, with polarizable molecular models, MD simulations are implemented with additional polarization calculations.

2.1.1. Non-polarizable Molecular Model

The only way to improve the interaction without additional terms for electrostatic interaction is to modify the partial charges. One of the popular methods is to scale down the partial charges at a constant rate, called 'scaled charge model'. Schröder demonstrated in his paper that polarizabilities are linearly dependent to charge scaling factors [39].

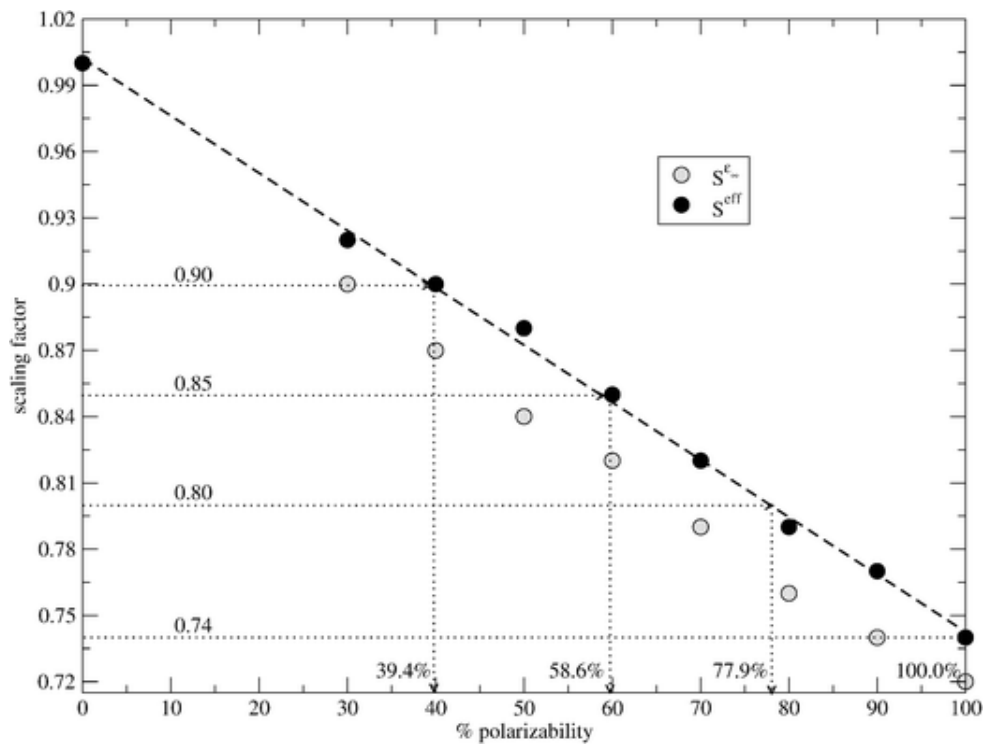


Figure 2-1. Correlation between polarizable simulation and their scale factors. [Schröder, 2012]

As the values of the charge set are scaled down, the dynamics of each compound are enhanced as the electrostatic interactions become weaker. It is known that the scaled charge model is suitable for predicting the behavior of RTILs, especially with 0.8 scaling factor, but showed poor results when other molecules were introduced to the systems. Despite the disadvantages, these non-polarizable force fields are commonly used in many studies because they are attractive in that fast implementation is available.

One of the representative non-polarizable force fields is CL&P force field [29]. The force field was broadly used in many studies because it could be compatible with OPLS-AA force field. In addition, the authors sophisticatedly developed partial charge sets for many RTILs hence the force field showed better performances in predicting thermodynamic and dynamic observations of the RTILs than other non-polarizable force fields. They obtained the partial charge sets by fitting the electrostatic potential from the charge to *ab initio* calculations at the points near each gas-phase ion, so-called ESP charge fitting method [40]. This method is extensively used in other force fields because the molecular dipole moment from the fitted charge set is consistent with the result of *ab initio* calculations. In order to implement MD simulations with CL&P, almost famous open-source software packages are available such as GROMACS, LAMMPS, DL_POLY, or OpenMM. However, it is convenient to use GROMACS because the developers offer an official guideline and some pre-processing packages to make topology files automatically.

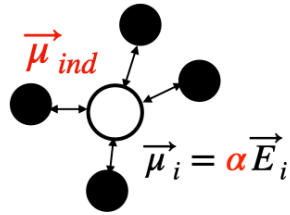
2.1.2. Polarizable Molecular Model

In contrast to non-polarizable force fields, where the potentials are described as

pairwise interactions, polarization effects in nature are more complex. Also, the force parameters are fixed during simulation time with non-polarizable force fields. Thus, it is inevitable to consider additional force calculations to obtain precise results. There are some approaches that combine *ab initio* calculation and molecular dynamics simulations to reassign force parameters as in nature, such as AIMD (*ab initio* molecular dynamics) or QM/MM^②. However, contemporary computing power is insufficient to conduct such simulations of the system with many atoms. Therefore, the force fields that enable MD simulations to explicitly calculate polarization effects are named polarizable force fields. The objective of the force fields is to include dipolar moments assigned to each atom site in electrostatic interactions responding to the local environments. In 1981, Applequist established the induced point dipole model [41], and Thole modified the model by introducing screening functions to prevent polarization catastrophe [42]. Figure 2-2 shows the scheme of the induced point dipole model.

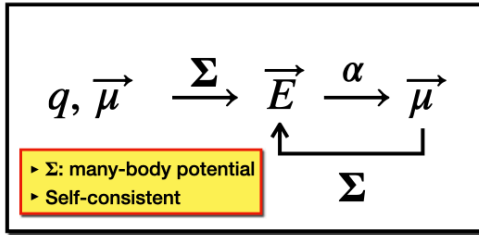
^② QM: quantum mechanics, MM: molecular mechanics

Induced Point Dipole Model



$$\begin{aligned}
 U_{\text{ind}} &= U_{\mu q} + U_{\mu\mu} + U_{\text{pol}} \\
 &= -\sum_i \vec{\mu}_i \cdot \vec{E}_i^q - \frac{1}{2} \sum_i \vec{\mu}_i \cdot \vec{E}_i^\mu + \frac{1}{2} \sum_i \vec{\mu}_i \cdot \vec{E}_i^t \\
 &= -\frac{1}{2} \sum_i \alpha_i \vec{E}_i^q
 \end{aligned}$$

Calculation



Thole Screening Function

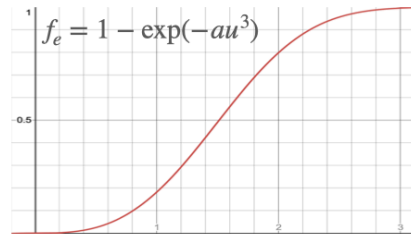


Figure 2-2. A schematic drawing of the induced point dipole model.

As point dipoles are obtained at once by solving linear equations of local electric fields and dipole tensors of each atom in a system, the induced point dipole model is considered a many-body potential. However, it takes too much time to calculate each point dipole every timestep analytically. Another way to calculate the point dipoles in practical simulations is to perform iterations until the dipoles converge in the self-consistent relationship as shown in Figure 2-2. Once the point dipoles are obtained from the many-body calculations, electrostatic interactions of charge-charge, charge-point dipole, and point dipole-point dipole are calculated by the following equations:

$$\begin{aligned}
 U_{\text{ind}} &= U_{\mu q} + U_{\mu\mu} + U_{\text{pol}} \\
 &= - \sum_i \vec{\mu}_i \cdot \vec{E}_i^\mu - \frac{1}{2} \sum_i \vec{\mu}_i \cdot \vec{E}_i^\mu + \frac{1}{2} \sum_i \vec{\mu}_i \cdot \vec{E}_i^t \\
 &= -\frac{1}{2} \sum_i \alpha_i \vec{E}_i^q
 \end{aligned} \tag{2}$$

, where q denotes partial charges; $\vec{\mu}$ denotes induced point dipoles; \vec{E} denotes local electric fields on a specific site; and α denotes polarizabilities.

There are several polarizable force fields based on the induced point dipole model. APPLE&P force field, which stands for ‘Atomistic Polarizable Potential for Liquids, Electrolytes & Polymers’, was originally developed by Oleg Borodin and has been modified by Wasatch Molecular Incorporated (WMI) [30]. As the full name connotes, the development of this force field began to precisely describe the behavior of electrolytes as well as polymers. Since 2004, Borodin and coworkers have verified that their force field is correct by comparison with experimental results and explained the behavior of ions in many electrolytes with polarizable MD simulations [43–45]. In addition, the force parameters were developed to be transferable. Thus, the reliability of the force field is indubitable. It is noted that the Buckingham potential, called exp-6 potential as well, was introduced to depict non-bonded

interactions other than electrostatic interactions to produce better results for polymers^③. The critical drawback of this force field is that it is not free of charge for all databases. For the reasons mentioned above, implementing MD simulations with the APPLE&P force field is limited to particular methods. WMI-MD, developed by WMI and formerly known as Lucretius, is the only way to run MD simulations with the APPLE&P force field without any modifications, but the software runs only on CPU. In order to resolve the problem of massive computational cost, modification of OpenMM was conducted in Chapter 4 of this dissertation, which allows the MD simulations with the APPLE&P force field to be GPU accelerated.

Another force field to implement polarizable MD simulations with the induced point dipole model is AMOEBA (Atomic Multipole Optimized Energetics for Biomolecular Applications) force field [46]. The force field has the purpose in its name itself to describe biomolecular systems. With the bigger molecules in biomolecular systems compared to others, the AMOEBA force field considers the higher permanent multipoles than monopoles. In other words, the higher terms in Equation (2) for molecular dipoles or even more quadrupoles are considered in the electrostatic interactions. However, the calculation of polarization would be more complicated considering multipole tensors. Fortunately, the AMOEBA force field can be implemented by several open-source MD software packages, such as Tinker or OpenMM, and most of the software packages are available to accelerate the implementation of MD simulations by GPU.

^③ Technically, non-bonded interactions cannot be separated from electrostatic interactions in the real world. This circumstance is more remarkable in the induced point dipole model as dispersion force in Buckingham potential ($\sim r^{-6}$) is relevant to the interaction between induced dipole moments. According to Borodin's study [], the force constants for the dispersion force are slightly smaller when polarization is considered than it is not.

The core-shell model is also commonly used in many research areas as well as electrolyte systems. The advantage of this model is the less computational cost compared to the induced point dipole model, and representative MD software packages these days, such as LAMMPS or GROMACS, can implement MD simulations with this model. Drude oscillator model is one of the famous polarizable molecular models of the core-shell model [47]. With a tiny particle connected to each heavy atom by harmonic potentials, called a Drude particle or a satellite atom, the charge distribution of the atoms can be changed during the simulation time, and the effective point dipoles can be obtained. One crucial point to implementing MD simulations with this model is that different ensembles should be applied to the Drude particles. Structural properties predicted by this model are in good agreement with both experiments and simulations with the induced point dipole model. However, it is known that the dynamics of the electrolyte systems is still underestimated if the hydrogen atoms are included because the hydrogen cannot have a Drude particle intrinsically.

2.2. Li^+ Transport Mechanism in Electrolytes

In contrast with neutral particles such as colloids, ion dynamics cannot be separated from the concept of ion correlation with oppositely charged components. For example, protons are transported in water with ion-hopping which could be considered exchanging their correlation sites as time passes. Like protons, Li^+ ions move in solutions or electrolytes with other molecules, especially negatively charged particles. Here, Li^+ ion transport mechanisms with two kinds of molecules are introduced; ionic liquids and poly-(ethylene oxide), which are used here.

2.2.1. Li⁺ Transport in Ionic Liquids

With ionic liquids as a solvent, Li⁺ ions inevitably coordinate with anions. It is known as Li⁺ ions are transported by two representative transport mechanisms: (i) structural diffusion; and (ii) vehicular diffusion. The structural diffusion represents a transport mechanism that anion coordination sites of Li⁺ ions are transferred to other sites, which seems like ion hopping. On the other hand, the vehicular diffusion represents that Li⁺ ions transport with their coordinated anions as an ion cluster. Both diffusion mechanisms are closely related to the concept of ion correlation lifetime. In general, structural diffusion contributes more than vehicular diffusion. In other words, if ion correlation lifetime decreases, the diffusivities of Li⁺ ions are expected to increase.

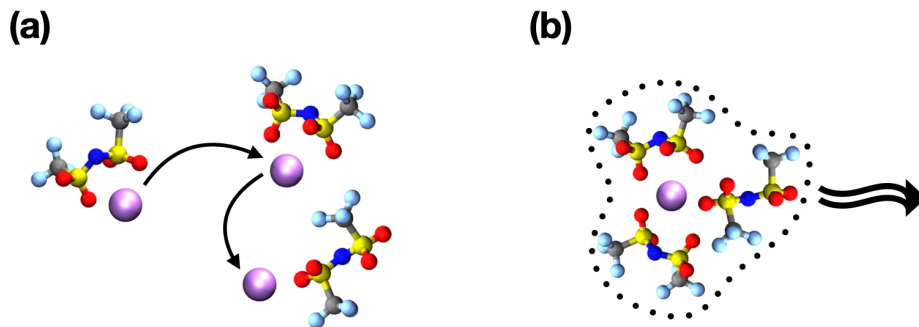


Figure 2-3. Illustration of two diffusion mechanisms of Li^+ with TFSi anions in ionic liquids: (a) Structural diffusion, and (b) Vehicular diffusion.

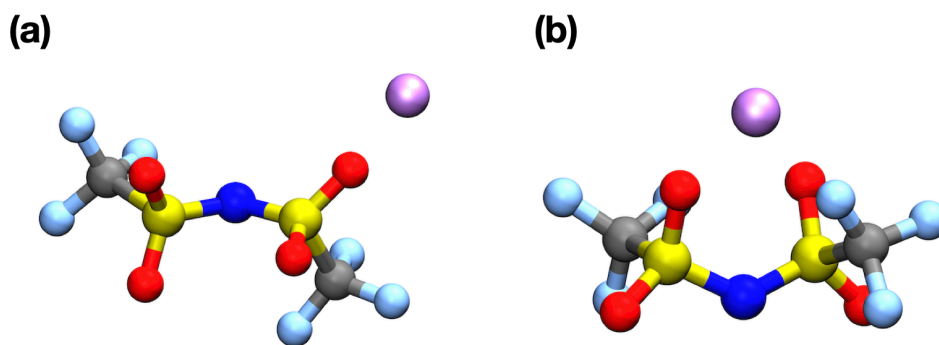


Figure 2-4. Coordination structures of Li^+ with oxygens of TFSi anions: (a) Monodentate, and (b) Bidentate.

There are two types of binding structures between Li^+ ions and bis(trifluoromethanesulfonyl)imide (TFSI) anions which are intensively studied in this dissertation. One is monodentate (κ_1), one of four oxygen in a TFSI anion makes coordination with a Li^+ ion, and the other is bidentate (κ_2), two oxygens make the coordination. The fraction of κ_1 and κ_2 is important in the dynamics of electrolytes. Once monodentate phases are formed, only one $-\text{SO}_2$ functional group of TFSI anions participate in coordination with a Li^+ ion, and the other $-\text{SO}_2$ is not influenced by the Li^+ ion. Therefore, unlike in bidentate phases, new coordination with another Li^+ ion can be constituted, and other TFSI anions are assembled in the vicinity of the Li^+ ion. In other words, the possibility of forming large ion clusters increases with the fraction of monodentate phases, and the large clusters induce the electrolytes to be more viscous. In general, the high friction force of viscose electrolytes suppresses the dynamics of each compound. In addition, the formation of large clusters increases ion correlation lifetime, which indicates the structural diffusion is suppressed. Thus, binding structures between Li^+ ions and TFSI anions are significant in investigating Li^+ ion dynamics in electrolytes.

2.2.2. Li^+ Transport in poly-(ethylene oxide)

As mentioned in Chapter 1, Maitra and Heuer studied Li^+ ion transport in poly-(ethylene oxide) (PEO) matrix and developed a transport model [33]. According to the study, Li^+ ions move under three major transport mechanisms: (i) intrachain ionic motion; (ii) segmental motion of PEO chains; and (iii) interchain jumps. Each mechanism has its characteristic timescale, notated as τ_1 , τ_2 , and τ_3 . Under the intrachain ionic motion, Li^+ ions move along the coordinated PEO chain and continuously exchange their coordinated sites (ethylene oxides) within the chain. τ_1

is simply calculated from the one-dimensional diffusion coefficient along the PEO chain as the principal axis. The subject of the segmental motion is a PEO chain rather than a Li^+ ion. However, it is significant to understand the segmental motion since the dynamics of Li^+ ions, which are tightly bound to ethylene oxides of PEO chains, are governed by that of PEO segments. The two mechanisms cannot be separated because the two motions occur in the same PEO chain. After τ_3 ^④, Li^+ ions hop to another chain, and the dynamics begin as a new event, which is also verified by the equivalence of backward and forward dynamics at the moment of hopping. Therefore, once a Li^+ ion coordinates to a PEO chain, the Li^+ ion has mixed behavior of (i) and (ii) for τ_3 . As the values of τ_3 is higher than those with ionic liquids, the contribution of two former mechanisms increases.

^④ The residual time of Li^+ with PEO chains

Chapter 3. Transport Mechanism of Li-ion in Polymer branched Nanopores

In this chapter, the transport mechanism of Li^+ ions is investigated in $\text{PYR}_{14}\text{TFSI}$ ionic liquids solution confined by PEO branched nanopores. This electrolyte seems to be similar Ahn and Kim designed in their previous study [22]. Since the study was not supported by detailed information at an atomic level, here the modeling of electrolytes is given for polarizable molecular dynamics simulation with the APPLE&P force field. In order to figure out the transport mechanism, the impact of pore sizes and relative amount of Li^+ ions compared to PEO chains on the dynamics of Li^+ ions are evaluated. Furthermore, a comparison with bulk binary electrolytes composed of $\text{LiTFSI}/\text{PYR}_{14}\text{TFSI}$ with the same fraction of Li^+ ion to ionic liquids was performed to show the better performance of our electrolytes.

3.1. Computational Method

3.1.1 Polarizable Molecular Dynamics Simulation

Molecular dynamics simulations were conducted for the $\text{LiTFSI}/\text{PYR}_{14}\text{TFSI}$ solution in PEO branched nanopores with the many-body polarizable force field based on the induced point dipole moment model. All force parameters were adopted from the APPLE&P force field. The nanopores were modeled as zigzag carbon nanotubes (CNTs) by the buildCstruct software package, and the positions of the CNTs were fixed during simulation time. 12 or 6 PEO chains with 25 repeat units were hexagonally branched to the wall of the corresponding CNT. The CNTs were located in the center of each simulation box with periodic boundary conditions,

which had a length of 200 Å in the radial (xy-) direction. LiTFSI/PYR₁₄TFSI solutions with a composition of LiTFSI:PYR₁₄TFSI=1:6 were filled into CNTs with different ratios of Li⁺ to PEO chains, denoted as PEO_xLi_y; (x, y) = (12, 60), (12, 40), (6, 30), and (6, 20). The initial configurations were built by the Packmol software package. PEO₁₂Li₆₀ and PEO₁₂Li₄₀ had twice the total number of atoms and longer diameters for the CNT channels (denoted as the ‘large’ systems) than PEO₆Li₃₀ and PEO₆Li₂₀ (denoted as the ‘small’ systems), respectively. Prior to performing simulations for the PEO_xLi_y systems, simulations of bulk solutions with the same composition as the corresponding confined systems were performed at each temperature to obtain density values and determine the dimensions of the nanopores. Schematic introduction of the materials and configurations in this chapter are presented in Figure 3-1, and the detailed quantitative information for each system is presented in Table 3-1.

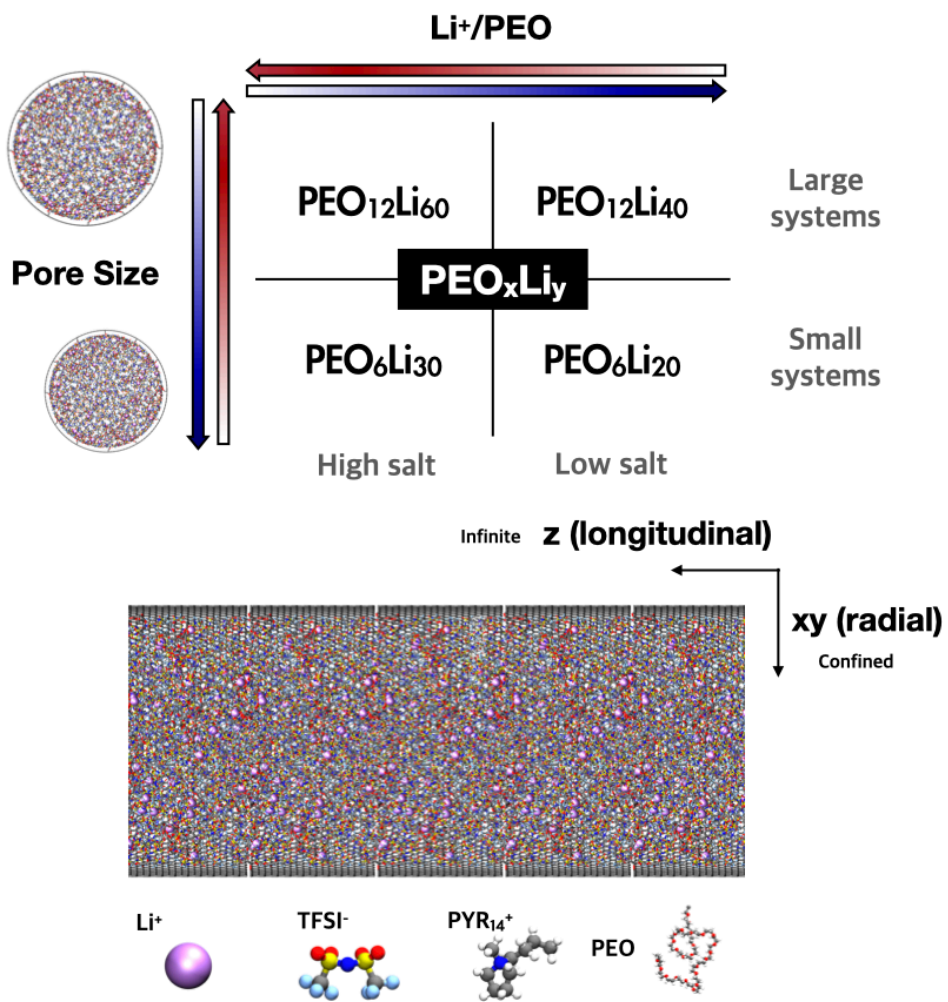


Figure 3-1. A schematic draw of the PEO_xLi_y systems for molecular dynamics simulations and visualizations.

Table 3-1. System information for MD simulations of PEO_xLi_y systems.

System	N _{Li} ⁺	N _{TFSI} ⁻	N _{PYR} ⁺	N _{PEO}	d _{CNT} [Å] ^{†,§}	h _{CNT} [Å] ^{†,§}	Simulation Time [ns] [‡]	Equilibration Time [ns] [‡]
PEO ₁₂ Li ₆₀	60	420	360	12	87.965 (115)	41.622, 40.840, 40.218	56, 60, 90	9, 12, 15
PEO ₁₂ Li ₄₀	40	280	240	12	74.197 (97)	41.622, 41.0264, 40.236	60, 60, 90	9, 10.5, 9
PEO ₆ Li ₃₀	30	210	180	6	63.488 (83)	41.622, 40.840, 40.218	60, 60, 90	9, 12, 12
PEO ₆ Li ₂₀	20	140	120	6	53.544 (70)	41.622, 41.0264, 40.236	60, 60, 60	9, 10.5, 18

[†]Considered the effective diameter $d_{\text{eff}} = 3.328$ Å. Indices n of the zigzag CNTs presented in parentheses.

[‡]In order of 423K, 393K, and 363K.

[§]Determined by the density values of each corresponding bulk solution.

Ewald summation method and a tapering function with a reaction-field approximation were introduced to calculate long-range interactions of charge–charge and charge–induced dipole interactions and for induced dipole–induced dipole interactions, respectively. The reversible reference system propagator algorithm (rESPA) was employed to perform time integration. Three different timescales were adopted for the integrator: short, with a timestep of 0.5 fs for bonding and bending motions; medium, with a timestep of 1.5 fs for torsions and nonbonded interactions within 7.0 Å; and long, with a timestep of 3.0 fs for nonbonded interactions between 7.0 and 11.0 Å and long-range electrostatics.

Once initial configurations were obtained from Packmol, energy minimization process was conducted with the steepest descent algorithm to avoid overlap of atoms. In order to start simulations with proper initial points, short NVT simulations with a Nosé-Hoover thermostat were performed at a high temperature of 600 K. Subsequently, at least 50 ns NVT simulations were performed to produce data at 423, 393, and 363 K, respectively. The first few nanoseconds of data were truncated to predict macroscopic observations, the details of which are also presented in Table 3-1. All the simulations were performed using the WMI-MD software package, which was modified to enable energy minimization, remove the rotational momentum of the center of mass, and apply positional constraints.

3.2. Structural Properties

As mentioned in Chapter 2, Li^+ ions are transported in the form of complexes in electrolytes. Therefore, understanding the local environment of Li^+ is crucial for specifying the transport mechanism. In present systems, there are two coordination

sites for Li^+ ions, one is the oxygen atoms of PEO chains (O_{PEO}), and the other is those of TFSI anions (O_{TFSI}), which constitute the first coordination shell of Li^+ . A quantitative analysis of Li^+ ion complexes was conducted via angle-dependent radial distribution functions (ARDF) and cluster analysis.

In order to investigate the impact of the PEO chains on the solutions, additional MD simulations for binary electrolytes ($\text{LiTFSI}/\text{PYR}_{14}\text{TFSI}$) were performed for comparison. Three-dimensional periodic isotropic simulation boxes consisted of 20 LiTFSI salt and 120 $\text{PYR}_{14}\text{TFSI}$ molecules. The optimized dimension of the simulation boxes had the equivalent length to the height of CNTs. All simulation conditions were identical to the above, except the simulation time of 45 ns.

3.2.1. First Coordination Shell of Li^+

In order to investigate the molecular coordination structure of the systems, angle-dependent radial distribution functions (ARDFs, $g(r, \theta)$) for each pair of atoms were calculated:

$$g(r, \theta) = \frac{1}{\langle \rho \rangle_{\text{local}, \theta}} \sum_i^N \sum_j^N \frac{\delta(r_{ij} - r) \delta(\theta_{ij} - \theta)}{2\pi r^2 \sin \theta} \quad (3)$$

, where θ is the angle between the given axis (z-axis) and a pair vector^⑤, and $\langle \rho \rangle_{\text{local}, \theta}$ denotes the ensemble-averaged local density for the corresponding θ within the maximal distance, r_{max} .

The ARDFs were renormalized by uniform fluid distribution $g_c(r, \theta)$ because $g(r, \theta)$ of the present systems cannot converge to unity due to the excluded volume effect occurring near the wall of the nanopores. One method to resolve this problem

^⑤ $\theta = 0^\circ$ means the pair vector is aligned in the longitudinal direction, and $\theta = 90^\circ$ indicates the radial direction.

is to renormalize the ARDFs into the uniform fluid distribution function, $g_c(r, \theta)$.

$$\tilde{g}(r, \theta) = g(r, \theta) / g_c(r, \theta) \quad (4)$$

, where $\tilde{g}_c(r, \theta)$ is renormalized ARDF considering the excluded volume effects. In order to obtain $g_c(r, \theta)$, atomistic Monte Carlo (MC) simulations^⑥ were performed for the same geometries as the previous work did [48]. Atomistic MC simulations were performed by Cassandra-1.2.5. The systems for MC simulations consist of a repulsive carbon nanotube with the same geometry as each corresponding system for MD simulations and 1,000 particles with no pair potential with each other like ideal gases. After sufficient sampling over 100,000 frames, the ARDFs were normalized by $g_c(r, \theta)$ of corresponding geometry as Equation (4), and the distribution functions are plotted in Figure 3-2.

^⑥ Without interatomic potentials, the atoms continue uniform motion through molecular dynamics. That's why the stochastic sampling should be applied.

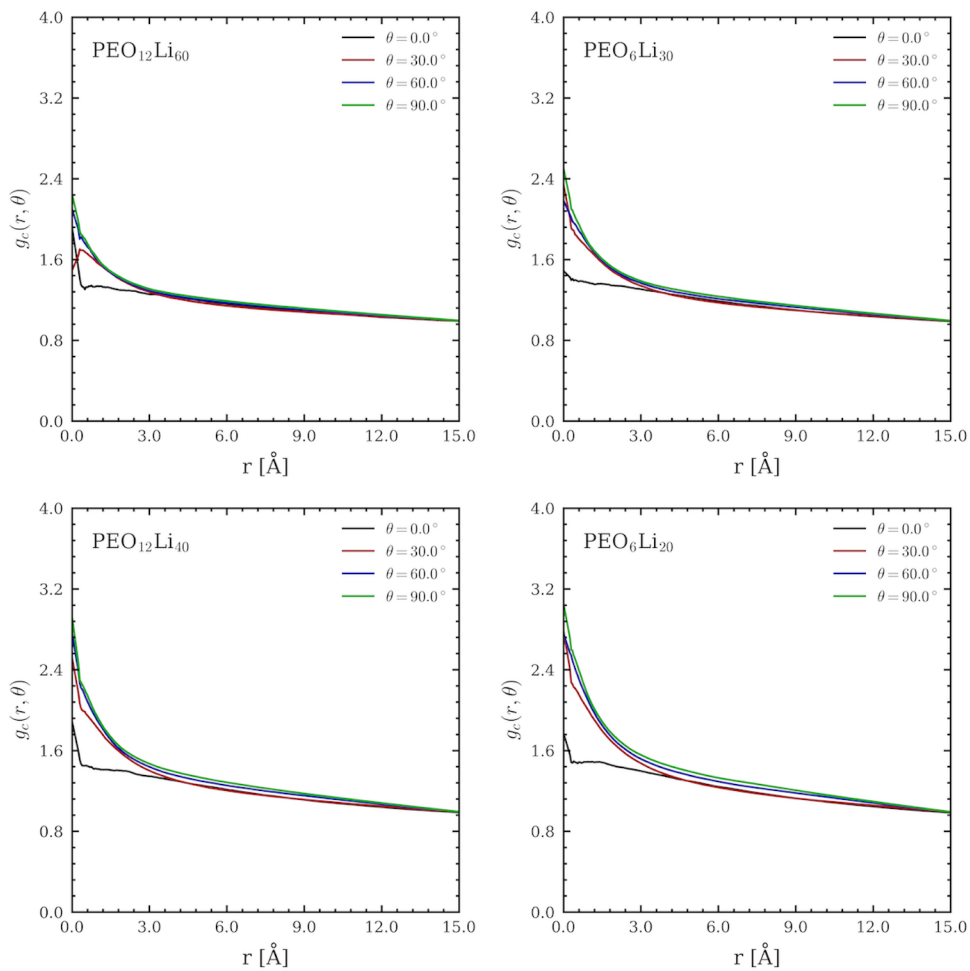


Figure 3-2. Uniform fluid distribution functions according to the direction of pair vectors between ideal fluids obtained by Monte Carlo simulations for the corresponding geometries of PEO_xLi_y.

Figure 3-3 shows the ARDFs for the $\text{Li}^+\text{-N}_{\text{TFSI}}$ and $\text{Li}^+\text{-Li}^+$ pairs at 423 K, and in particular, RDFs of longitudinal ($\theta = 0^\circ$) and radial ($\theta = 90^\circ$) directions are given in Figure 3-4. In addition, Figure 3-5(a-c) show the ARDFs for the $\text{Li}^+\text{-O}_{\text{PEO}}$ pair. As the first coordination shell of Li^+ consists of TFSI and PEO chains, $g^{\text{Li}^+\text{-N}_{\text{TFSI}}}(r, \theta)$ and $g^{\text{Li}^+\text{-O}_{\text{PEO}}}(r, \theta)$ exhibit distinct peaks near 3.5 Å and 2.5 Å, respectively. It is noteworthy that the magnitude of the first peak of $g^{\text{Li}^+\text{-N}_{\text{TFSI}}}(r, \theta)$ decreases with the angle. This indicates that the coordination energy between Li^+ and TFSI in the longitudinal direction is lower than in the radial direction, which means that Li^+ ions have a preferential direction for their movement. Compared to the $\text{PEO}_{12}\text{Li}_{40}$ systems, the $\text{PEO}_{12}\text{Li}_{60}$ have higher peak intensities for $g^{\text{Li}^+\text{-N}_{\text{TFSI}}}(r, \theta)$ due to the high ratio of TFSI anions to PEO chains. The fact that the small systems ($\text{PEO}_6\text{Li}_{30}$ and $\text{PEO}_6\text{Li}_{20}$) show a similar tendency to the large systems shows that the effect of the pore size is limited. The opposite trend can be expected for $g^{\text{Li}^+\text{-O}_{\text{PEO}}}(r, \theta)$ as well. However, it is not trivial to directly compare the ARDFs because the peak intensities are not dependent on the direction of the pairs (Figure 3-5 (d)), so further calculation should be accompanied. The ARDFs at other temperatures shown in Figure 3-6(a, b, e, f) suggest nothing special regarding temperature dependency.

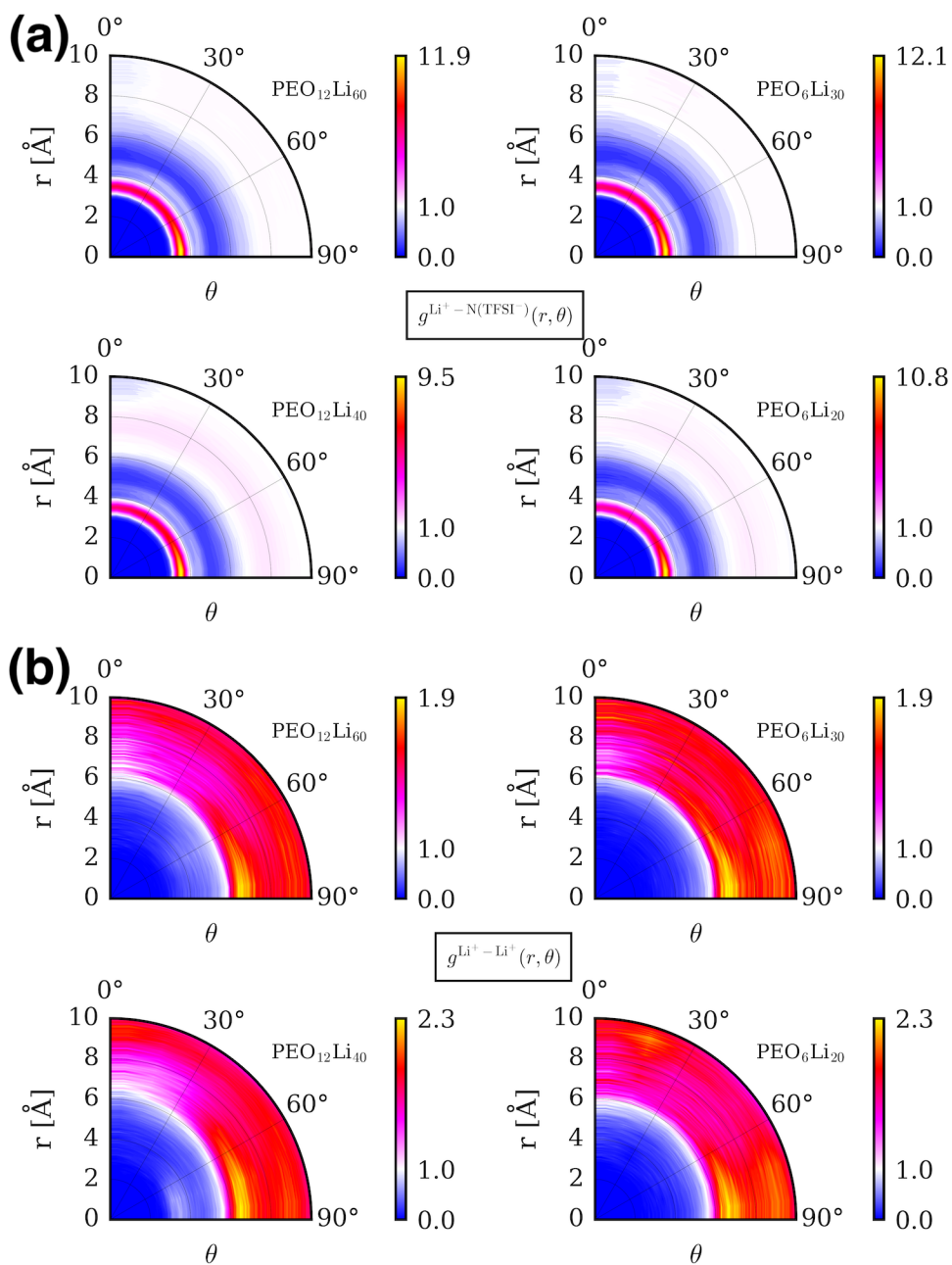


Figure 3-3. Heatmaps of angle-dependent radial distribution functions at 423 K for all PEO_xLi_y systems: (a) $g^{\text{Li}^+ - \text{N}(\text{TFSI}^-)}(r, \theta)$, (b) $g^{\text{Li}^+ - \text{Li}^+}(r, \theta)$.

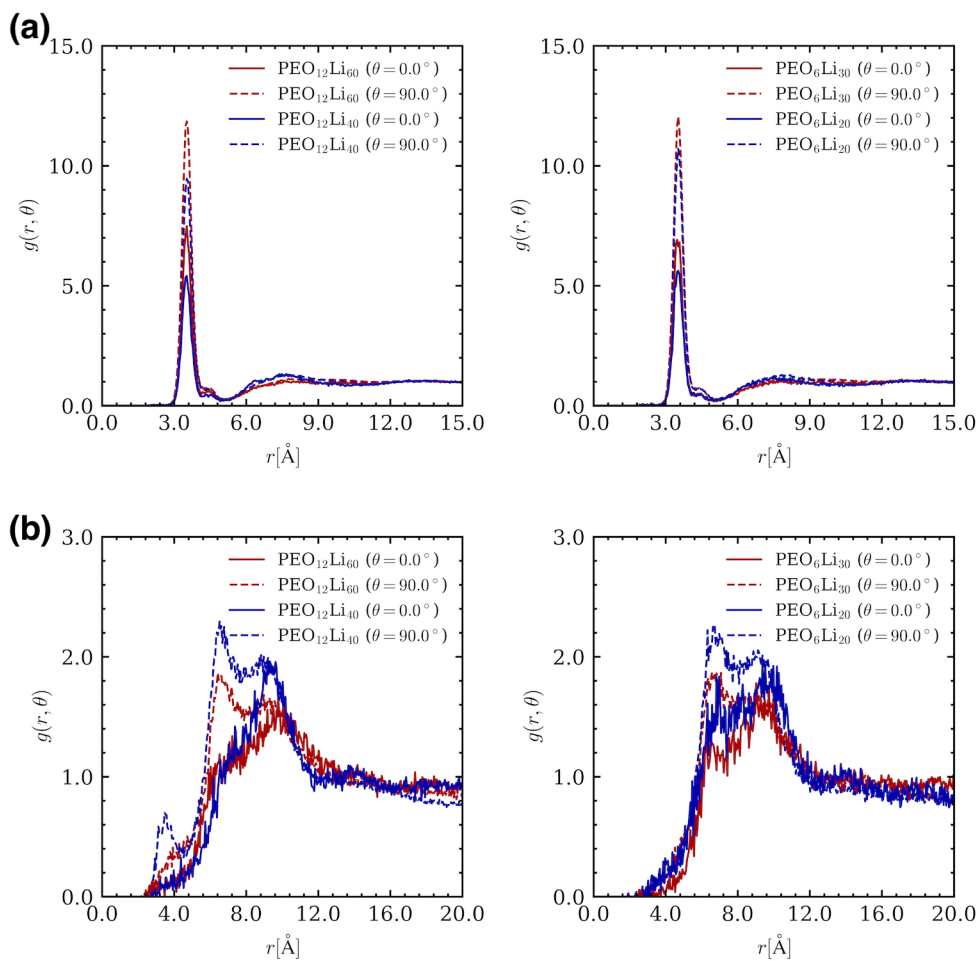


Figure 3-4. Angle-dependent radial distribution functions in longitudinal ($\theta = 0^\circ$) and radial ($\theta = 90^\circ$) directions: (a) $g^{\text{Li}^+-\text{N}_{\text{TFSL}}}(r, \theta)$, (b) $g^{\text{Li}^+-\text{Li}^+}(r, \theta)$.

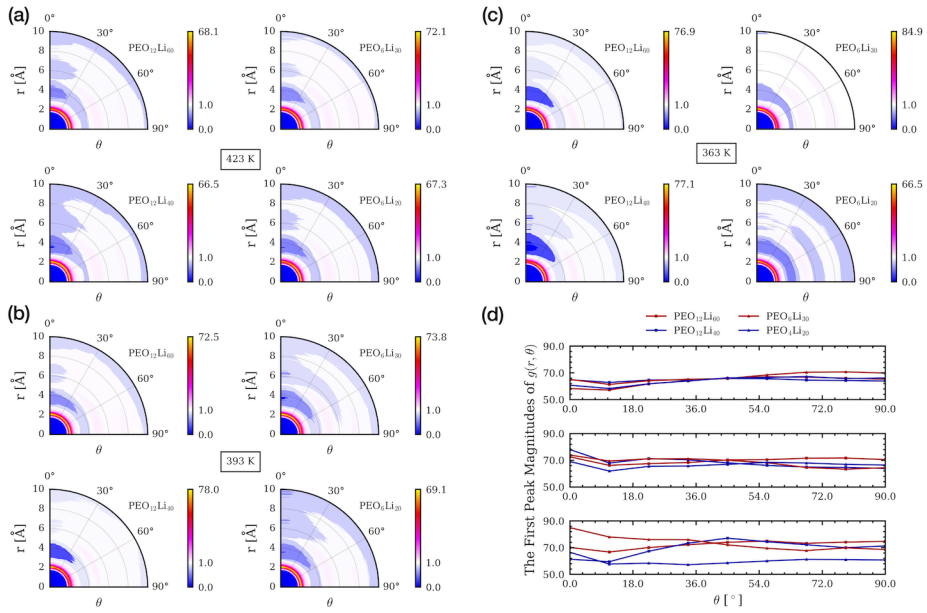


Figure 3-5. Angle-dependent radial distribution functions $g^{\text{Li}^+-\text{O}_{\text{PEO}}}(r, \theta)$ for all systems at (a) 423, (b) 393, and (c) 363 K. (d) The magnitudes of the first peaks of $g^{\text{Li}^+-\text{O}_{\text{PEO}}}(r, \theta)$ as a function of θ .

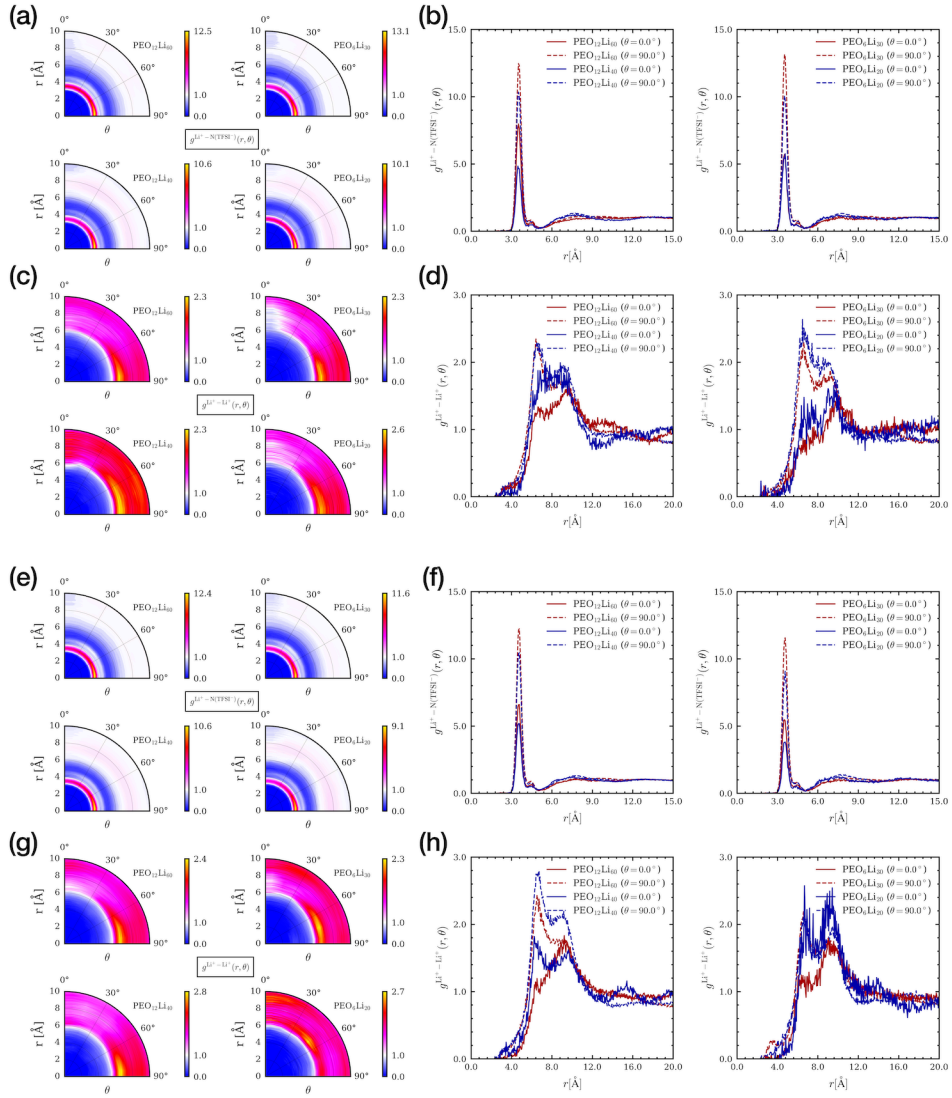


Figure 3-6. Angle-dependent radial distribution functions at 393 K (a–d) and 363 K (e–h) for all systems. (a, e) Heatmaps for $g^{\text{Li}^+-\text{N}_{\text{TFSI}}}(r, \theta)$ (b, f) $g^{\text{Li}^+-\text{N}_{\text{TFSI}}}(r, \theta)$ in longitudinal and radial directions. Left: the large systems, right: the small systems. (c, g) Heatmaps for $g^{\text{Li}^+-\text{Li}^+}(r, \theta)$ (d, h) $g^{\text{Li}^+-\text{Li}^+}(r, \theta)$ in longitudinal and radial directions. Left: the large systems, right: the small systems.

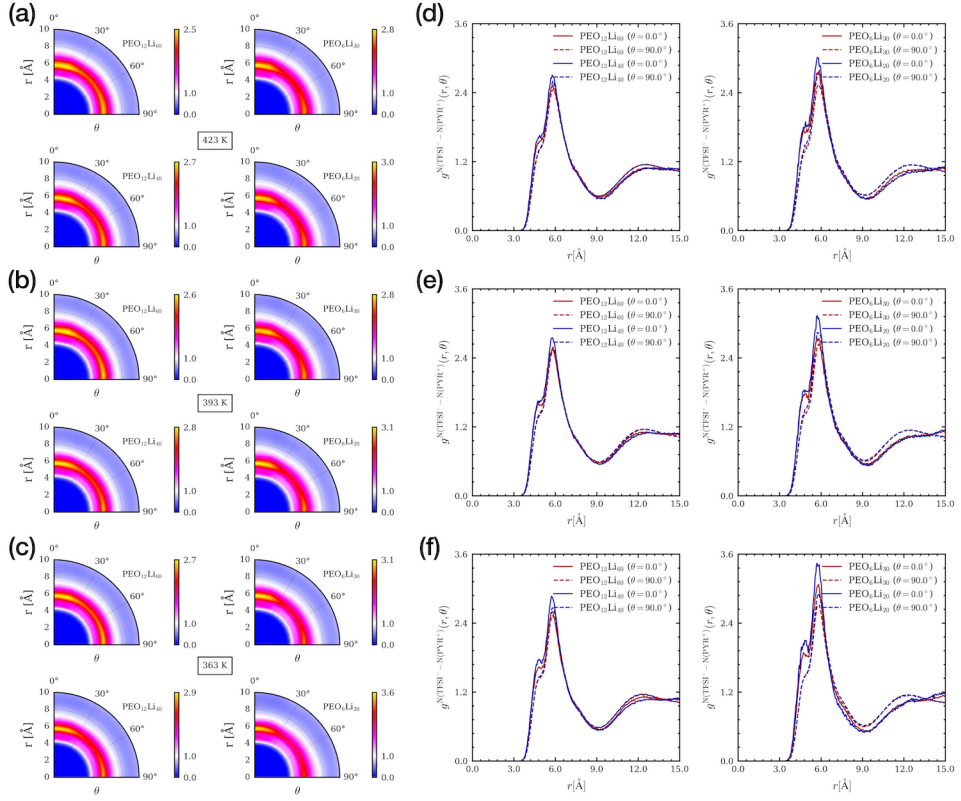


Figure 3-7. Angle-dependent radial distribution functions $g^{\text{N}_{\text{TFSI}}-\text{N}_{\text{PYR}}}(r, \theta)$ for all systems at (a, d) 423 K, (b, e) 393 K, and (c, f) 363 K. (a–c) Heatmaps for $g^{\text{N}_{\text{TFSI}}-\text{N}_{\text{PYR}}}(r, \theta)$ and (d–f) $g^{\text{N}_{\text{TFSI}}-\text{N}_{\text{PYR}}}(r, \theta)$ in longitudinal and radial directions. Left: the large systems, right: the small systems.

The average number of atoms in the first coordination shell of Li^+ was calculated through the volume integration of the ARDF and defined as a running coordination number (CN). $n^{\text{Li}^+}(\text{O}_{\text{PEO}})$, $n^{\text{Li}^+}(\text{N}_{\text{TFSI}})$, and $n^{\text{Li}^+}(\text{O}_{\text{TFSI}})$ are listed in Table 3-2. As expected previously, $n^{\text{Li}^+}(\text{O}_{\text{PEO}})$ of $\text{PEO}_{12}\text{Li}_{60}$ is smaller than that of $\text{PEO}_{12}\text{Li}_{40}$, and the small systems also show a similar pattern. According to CNs for Li^+ with O_{PEO} and O_{TFSI} , a total of 4–5 oxygen atoms are located near Li^+ , of which 2–3 are O_{PEO} and the others are O_{TFSI} . However, these values are underestimated compared to the actual numbers of each oxygen binding to a Li^+ because their coordination structures are not homogeneous^⑦. Hence the values should be normalized with the fraction of each structure, which is discussed in Section 3.2.2. Li-TFSI complex. The values of $n^{\text{Li}^+}(\text{N}_{\text{TFSI}})$ indicate that there are 1–2 TFSI anions near Li^+ . In addition, it is noted that approximately 1.7 O_{TFSI} are coordinated with Li^+ within a single TFSI anion for all the solutions based on the ratio of $n^{\text{Li}^+}(\text{O}_{\text{TFSI}})$ to $n^{\text{Li}^+}(\text{N}_{\text{TFSI}})$. This suggests that Li^+ with two O_{TFSI} of a TFSI anion (bidentate) is more prevalent than Li^+ with one O_{TFSI} of a TFSI anion (monodentate), the structures of which are shown in the previous chapter (Figure 2-4).

^⑦ There are Li^+ ions binding to PEO or TFSI solely

Table 3-2. Running coordination numbers from MD simulations of PEO_xLi_y systems. The values were determined near the end of the first coordination shells from the results of radial distribution functions.

System	423 K			393 K			363 K		
	$n^{\text{Li}^+}(\text{O}_{\text{PEO}})$	$n^{\text{Li}^+}(\text{N}_{\text{TFSI}})$	$n^{\text{Li}^+}(\text{O}_{\text{TFSI}})$	$n^{\text{Li}^+}(\text{O}_{\text{PEO}})$	$n^{\text{Li}^+}(\text{N}_{\text{TFSI}})$	$n^{\text{Li}^+}(\text{O}_{\text{TFSI}})$	$n^{\text{Li}^+}(\text{O}_{\text{PEO}})$	$n^{\text{Li}^+}(\text{N}_{\text{TFSI}})$	$n^{\text{Li}^+}(\text{O}_{\text{TFSI}})$
PEO ₁₂ Li ₆₀	2.01	1.49	2.65	2.02	1.56	2.77	2.14	1.56	2.74
PEO ₁₂ Li ₄₀	2.80	1.17	2.06	2.94	1.13	2.00	2.82	1.23	2.16
PEO ₆ Li ₃₀	2.00	1.51	2.71	2.02	1.55	2.76	2.30	1.48	2.61
PEO ₆ Li ₂₀	2.68	1.22	2.16	2.82	1.20	2.11	3.02	1.16	2.01

The predominance of the bidentate structure is also confirmed by the fact that $g^{\text{Li}^+-\text{N}_{\text{TFSI}}}(r, \theta)$ exhibit a marginal increment at 4.5 Å, which refers to a monodentate structure, whereas the first peak refers to a bidentate structure [49]. This would be favorable for Li^+ transport because the monodentate structures may provide a possibility for the Li^+ to coordinate with more other TFSI anions, as discussed in Chapter 2. The absence of a distinct peak (>1.0) for $g^{\text{Li}^+-\text{Li}^+}(r, \theta)$ also supports this argument (Figure 3-3 (b), Figure 3-4 (b), and Figure 3-6 (c, d, h, g)). According to the previous work [50] involving the simulation of the binary electrolytes (LiTFSI/PYR₁₄TFSI) with relatively high salt concentrations, pair distribution of Li^+-Li^+ pair exhibited significant peaks near 5.0 Å, which indicated that large Li clusters^⑧ were formed. Therefore, it may be thought that the existence of PEO chains suppresses the formation of large Li^+ clusters, and Li-TFSI complexes can be transported faster in the present systems.

3.2.2. Li-TFSI complex

Li^+ ions in RTIL electrolytes are transported in the form of $[\text{Li}_x(\text{X})_n]^{-(n-x)}$ ($\text{X} = \text{anions}$) complexes. As the average size of the complexes increases, the ion conductivity of the system decreases due to the large hydrodynamic radius of the complexes [51]. Therefore, identifying the states of Li-anion complexes in a system can help figure out the ion transport mechanism. The Li^+ ions are classified into two major groups: bonded to the PEO chains or not.

Cluster analysis was conducted with NetworkX 2.5 [52] to quantify the amounts of $[\text{Li}_x\text{TFSI}_n]^{-(n-x)}$ complexes in each group. The detailed procedure is following. First, Li^+ ions were categorized depending on the number of attached PEO chains. Second,

^⑧ The clusters with more than two Li^+ ions and five TFSI anions.

distance arrays were constructed between Li^+ ions and TFSI anions. The distance arrays were calculated from MDAnalysis-2.0.0. Finally, graphs for $[\text{Li}_x\text{TFSI}_n]^{-(n-x)}$ complexes of each group were obtained from the distance arrays. When the weight of an edge was 2, the structure was considered 'bidentate', and 'monodentate' when it was 1. The number of nodes of each graph was considered the number of TFSI anions in each ion cluster. The large Li^+ clusters were classified separately.

Figure 3-8 and Figure 3-9 show the results of the cluster analysis and their representative conformations, respectively. Approximately half of the Li^+ ions are attached to the PEO chains in the $\text{PEO}_{12}\text{Li}_{60}$ and $\text{PEO}_6\text{Li}_{30}$ systems, and two-thirds of the Li^+ ions are attached to the PEO chains of the $\text{PEO}_{12}\text{Li}_{40}$ and $\text{PEO}_6\text{Li}_{20}$ systems. Interestingly, the fraction of Li^+ bound to the PEO chains is equivalent to the ratio of the number of O_{PEO} to the number of oxygen atoms in each system, which means there are no energy-preferred binding sites for Li^+ . Considering the fraction of Li^+ bound to PEO chains and $n^{\text{Li}^+}(\text{O}_{\text{PEO}})$, it could be found that approximately four EOs surrounded a single Li^+ ion. This result is reasonable because over half of the Li^+ ions bound to the PEO chains are coordinated to EOs only (5–6 O_{PEO} per Li^+). Other ions in that group form complexes with 1 or 2 TFSI anions. Thus, the Li^+ ions could hop from the PEO chain to TFSI.

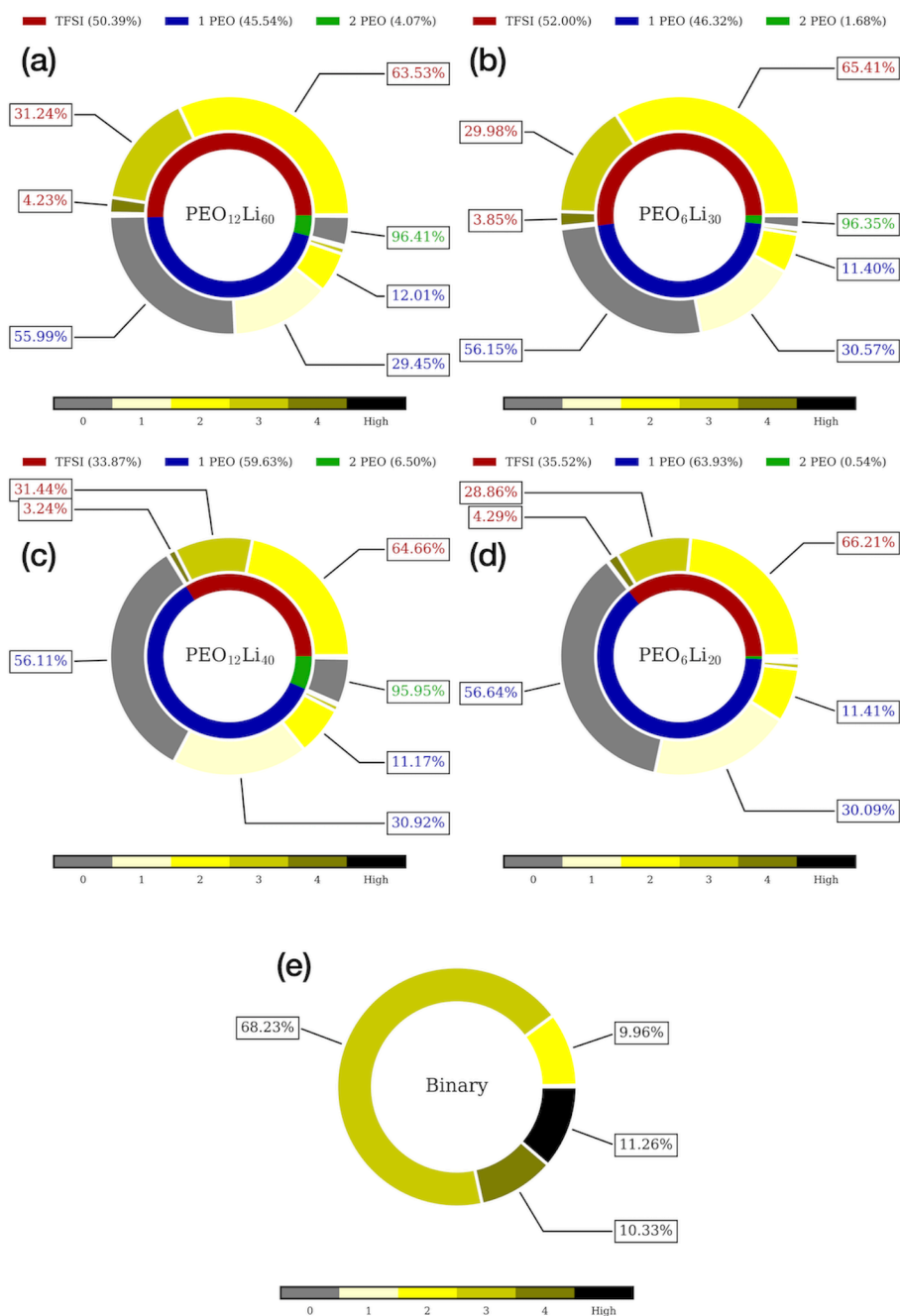


Figure 3-8. Fraction of $[\text{Li}_x(\text{TFSI})_n]^{-(n-x)}$ complexes in each group divided into the number of attached PEO chains from the result of cluster analysis at 423 K. The inner pie charts exhibit the number of Li^+ ions of each group, and the yellow outer pie charts exhibit the number of attached TFSI anions to Li^+ ions in each group. The color of each group distinguishes each percentage within rectangles; Red: Li^+ ions totally coordinated with TFSI anions, Blue: Li^+ ions coordinated to 1 PEO chain, and Green: Li^+ ions coordinated to 2 PEO chains. (a) PEO₁₂Li₆₀ (b) PEO₆Li₃₀ (c) PEO₁₂Li₄₀ (d) PEO₆Li₂₀ (e) Binary electrolyte.

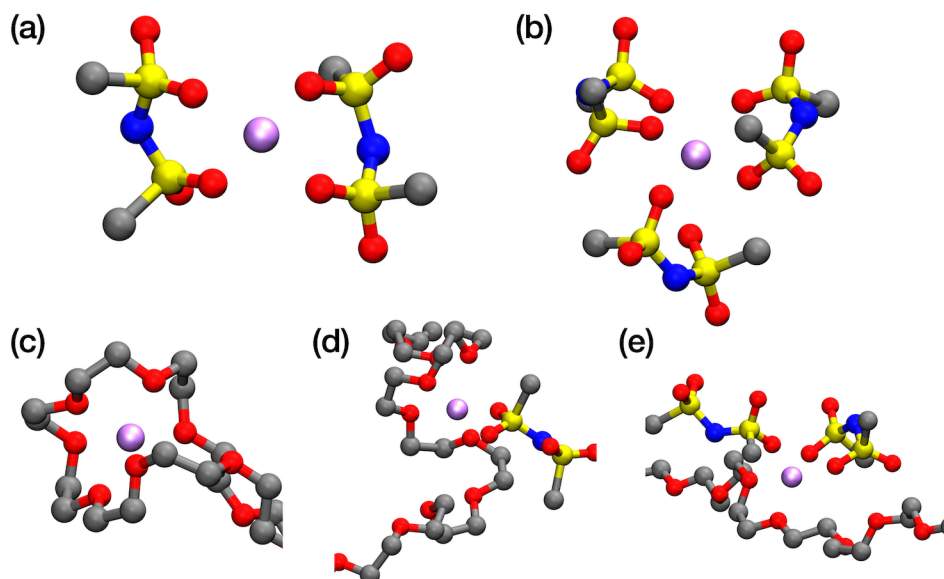


Figure 3-9. Five Representative structures that Li^+ ions could have in PEO_xLi_y electrolytes. Fluorene, hydrogen, and electron lone pairs are now shown in this figure. (a) $[\text{LiTFSI}_2]^-$. Two bidentate structures comprise the complex. (b) $[\text{LiTFSI}_3]^{2-}$. Two bidentate and one monodentate structure comprise the complex. (c) The Li^+ ion totally coordinated with a PEO chain. Almost six EOs are surrounding the Li^+ ion. (d) The Li^+ ion coordinated with one PEO chain and one TFSI⁻ anion. Four EOs and one oxygen atom of a TFSI⁻ anion are surrounding the Li^+ ion. The TFSI⁻ anion forms a monodentate structure. (e) The Li^+ ion coordinated with one PEO chain and two TFSI⁻ anions. Two EOs and three oxygen atoms of TFSI⁻ anions are surrounding the Li^+ ion. The TFSI⁻ anions form one monodentate and one bidentate structure, respectively. The PEO chain is almost linear.

Once a Li^+ ion is entirely detached from the PEO chains, they form $[\text{LiTFSI}_n]^{(n-1)-}$ complexes, of which $[\text{LiTFSI}_2]^-$ is the most. According to the previous studies [49,50], this phase emerged when the solution was sufficiently dilute, whereas the $[\text{LiTFSI}_3]^{2-}$ phase was dominant at a practical salt concentration ($x = 0.1\text{--}0.3$). The emergence of $[\text{LiTFSI}_2]^-$ in the present systems is due to the PEO chains contributing to the coordination with Li^+ , which causes the effective salt concentration of the electrolyte to become low. Interestingly, the fractions of complexed TFSI anions within the groups show similar trends regardless of the pore sizes and the ratios of Li^+ to the PEO chains of the systems, except for a fraction of Li^+ bound to two PEO chains. This results from the shorter distance between adjacent branched chains in the large systems than in the small ones.

Figure 3-10 indicates that there are few monodentate structures, which is in good agreement with the results of ARDFs. This suggests that bidentate structure is more stable than monodentate structure, which is consistent with the previous study [53]. Hence, $[\text{LiTFSI}_2]^-$ complexes consist of two bidentate structures with four O_{TFSI} of a Li^+ ion, whereas $[\text{LiTFSI}_3]^{2-}$ complexes inevitably form at least one or more monodentate structures. Once a TFSI anion forms a monodentate structure with one Li^+ ion by one of its $-(\text{SO}_2\text{CF}_3)$ functional groups, the other group can form another monodentate structure, resulting in the formation of large Li-clusters. Compared with the result of the binary electrolyte, a much smaller fraction of large Li-clusters is observed than in the PEO_xLi_y systems. In this regard, PEO chains suppress Li^+ ion aggregation and provide better performance in terms of dynamics.

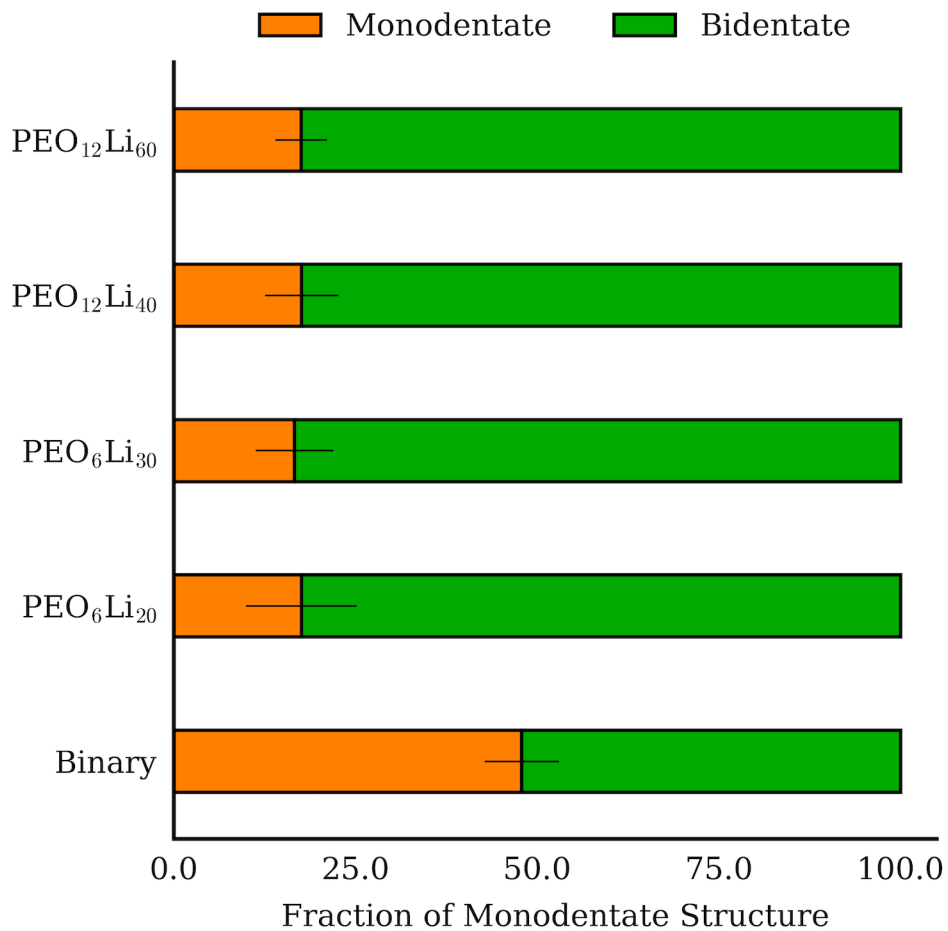


Figure 3-10. Fraction of monodentate structure compared to bidentate structure for all systems as well as binary electrolyte from the result of cluster analysis.

3.3. Transport Properties

Transport properties of each system were evaluated, which are directly relevant to the performance of LIBs. In particular, the diffusion coefficients and ionic conductivities of the electrolytes were estimated, and how the system conditions influenced the dynamic properties was studied. Similar to the structural properties, a comparison with the binary electrolytes was also conducted.

3.3.1. Diffusion Coefficient

Self-diffusion coefficient D_i of molecules i can be calculated using the Einstein relation:

$$D_i = \lim_{t \rightarrow \infty} D_i^{\text{app}} = \lim_{t \rightarrow \infty} \frac{1}{2nt} \sum_i^N \langle [r_i(t) - r_i(0)]^2 \rangle \quad (5)$$

, where D_i^{app} denotes the time-dependent apparent diffusion coefficients, $r_i(t)$ denotes the center of mass position at time t , n denotes the number of dimensions, and $\langle \rangle$ denotes the ensemble average. Here, $\langle [r_i(t) - r_i(0)]^2 \rangle$ is the mean square displacement (MSD) of each component. Diffusion coefficients in the longitudinal direction of the channel, D_z , were only considered because of the confinement in the radial direction. Figure 3-11 plots the diffusion coefficients of each component according to the temperature for all systems, including binary electrolyte systems, for reference. D_{z, Li^+} shows the following order: $\text{PEO}_6\text{Li}_{30} \geq \text{PEO}_{12}\text{Li}_{60} > \text{PEO}_6\text{Li}_{20} \geq \text{PEO}_{12}\text{Li}_{40} > \text{Binary}$. With an increase in the ratios of Li^+ to the PEO chains, the diffusion coefficients tend to be higher. This result may be related to the Li^+ coordination. As mentioned in Section 3.2.2. Li-TFSI complex, the Li^+ ions in the systems were classified depending on whether they were bound to the PEO chains. Li^+ ions without PEO chains are transported by the surrounding TFSI, whereas Li^+

with PEO chains travel along the chains and in the segmental motion of the chains [33]. The Li^+ ions linked to the PEO chains are relatively slower than other ions because of the fixed endpoint and high molecular weight of the PEO chains. As the number of Li^+ bound to the PEO chains increases with a decrease in the ratio of O_{TFSI} to O_{PEO} , it is reasonable that the $\text{PEO}_{12}\text{Li}_{40}$ and $\text{PEO}_6\text{Li}_{20}$ have smaller diffusion coefficients than the $\text{PEO}_{12}\text{Li}_{60}$ and $\text{PEO}_6\text{Li}_{30}$, respectively. This is also confirmed by tracking MSD values of Li^+ ions categorized by their coordination sites, PEO or TFSI. (Figure 3-12) The Li^+ ions in the small systems are slightly faster than those in the large systems, which is attributed to the existence of Li-PEO_2 complexes in the $\text{PEO}_{12}\text{Li}_{60}$ and $\text{PEO}_{12}\text{Li}_{40}$. All the diffusion coefficients for the PEO_xLi_y systems are greater than those for the binary electrolytes by a factor of 1–2. This is attributed to the high friction induced by the large hydrodynamic diameters of the $[\text{Li}_x\text{TFSI}_n]^{(n-x)}$ ($x \geq 2$) complexes, which are almost absent when the PEO chains are introduced.

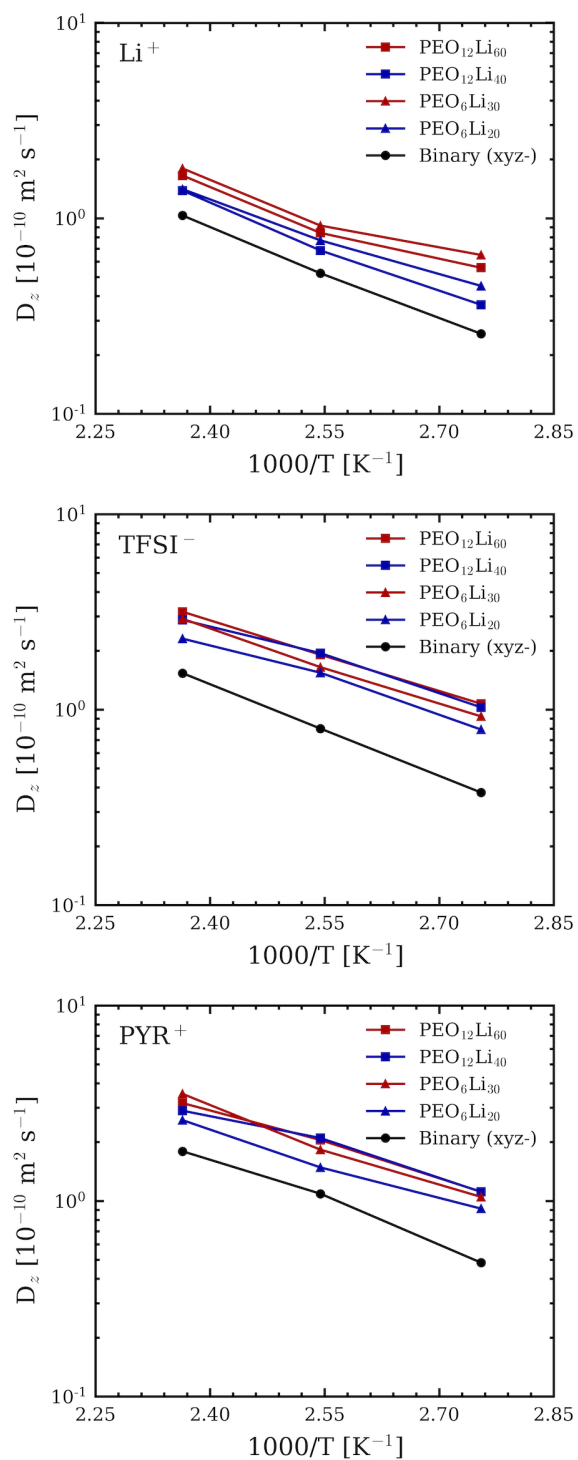


Figure 3-11. Longitudinal diffusion coefficients as a function of temperature for all systems as well as binary electrolytes. Note that the values for binary electrolytes are isotropic diffusion coefficients.

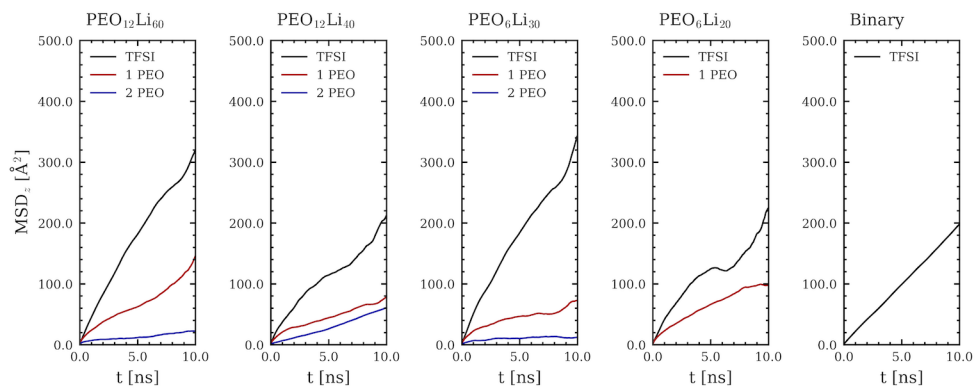


Figure 3-12. Mean square displacement of Li^+ ions in PEO_xLi_y electrolytes categorized by their coordination site: Black – with TFSI, Red – with 1 PEO, and Blue – with 2 PEO.

The magnitudes of the diffusion coefficients for each ion are in order of $D_{z, \text{PYR}} \geq D_{z, \text{TFSI}} > D_{z, \text{Li}^+}$. Interestingly, while D_{z, Li^+} is increased in the small systems, $D_{z, \text{PYR}}$ and $D_{z, \text{TFSI}}$ are decreased. This may be attributed to the confinement effects from smaller pore sizes in the small systems on the relatively bulky PYR and TFSI, but not on Li^+ , than in the large systems. The results correspond to the higher magnitudes of ARDFs for the PYR-TFSI pair in the small systems compared to those of the large systems. (Figure 3-7). Consequently, the contribution of Li^+ ions increases to the system dynamics. Hence, enhanced charge and discharge performances could be expected for the electrolyte with a decrease in the size of the ion transport channel [54].

3.3.2. Ionic Conductivity

One of the most important properties of LIBs is their ionic conductivity. The ionic conductivities were calculated from the MD simulation results using the following equation, which is based on the Einstein relationship:

$$\lambda = \lim_{t \rightarrow \infty} \lambda^{\text{app}} = \lim_{t \rightarrow \infty} \frac{e^2}{6tV k_{\text{B}} T} \sum_{ij}^N z_i z_j \langle [r_i(t) - r_i(0)] [r_j(t) - r_j(0)] \rangle \quad (6)$$

, where λ^{app} is the apparent time-dependent conductivity; e is the electron charge; V is the system volume; k_{B} is Boltzmann's constant; T is the temperature; i and j are all the charged molecules; z_i and z_j are the charges for molecules i and j , respectively; and r_i is the Cartesian coordinate along the trajectory of molecule i . However, because λ^{app} considers correlations between all ion pairs, this value has poor statistics. Thus, it cannot be determined accurately for the long-time limit. Instead, the ionic conductivity can be calculated from the diffusion coefficients under conditions where the ions in the system are sufficiently dissociated. The degree of

ion dissociation, α , which is also called the degree of uncorrelated ion motion, is defined by the following equation:

$$\alpha = \lambda/\lambda_{\text{ideal}} = \lim_{t \rightarrow \infty} \frac{\sum_{ij}^N z_i z_j \langle [r_i(t) - r_i(0)] [r_j(t) - r_j(0)] \rangle}{\sum_i^N z_i^2 \langle [r_i(t) - r_i(0)]^2 \rangle} \quad (7)$$

, where the calculation of ideal conductivity λ_{ideal} corresponds to the Nernst-Einstein equation. Here, $\alpha = 1$ means that all the ion pairs move independently, whereas $\alpha = 0$ means that all the ions move collectively. The values listed in Table 3-3 for α_z , the degree of ion dissociation along the longitudinal direction of the nanopores, are in the range of 0.6–0.8 at various temperatures. Because the values of α_z are high enough for an ionic liquid electrolyte, the ionic conductivities of each system could be calculated by combining Equation (7) and the following equation:

$$\lambda^{\text{ideal}} = \frac{e^2}{V k_B T} (n_{\text{Li}^+} D_{\text{Li}^+} + n_{\text{PYR}} D_{\text{PYR}} + n_{\text{TFSI}} D_{\text{TFSI}}) \quad (8)$$

Figure 3-13 shows the temperature-dependent ionic conductivities, λ_z , for each electrolyte, as well as $\lambda_z^{\text{Li}^+}$. Because all the ions within the systems were considered, the values of λ_z are equivalent for all cases except PEO₆Li₂₀ due to the abnormally low values for $D_{z, \text{TFSI}}$ and $D_{z, \text{PYR}}$, which are attributed to the reinforced confinement effect from the reduced pore sizes on bulky RTIL molecules. Nevertheless, the preferential movement to the longitudinal direction in nanopores facilitates higher λ values than binary electrolytes. $\lambda_z^{\text{Li}^+}$ is as crucial as λ for electrolytes in the battery cycle, as previously mentioned. The temperature dependencies are similar to those of the diffusion coefficients that increase according to the ratios of Li⁺ to the PEO chains and the reduction of pore sizes, exceeding the values for binary electrolytes.

Table 3-3. Degrees of ion dissociation of each system

Temperature	PEO₁₂Li₆₀	PEO₁₂Li₄₀	PEO₆Li₃₀	PEO₆Li₂₀	Binary
423	0.60	0.75	0.65	0.68	0.70
393	0.73	0.58	0.66	0.62	0.59
363	0.71	0.77	0.74	0.68	0.64

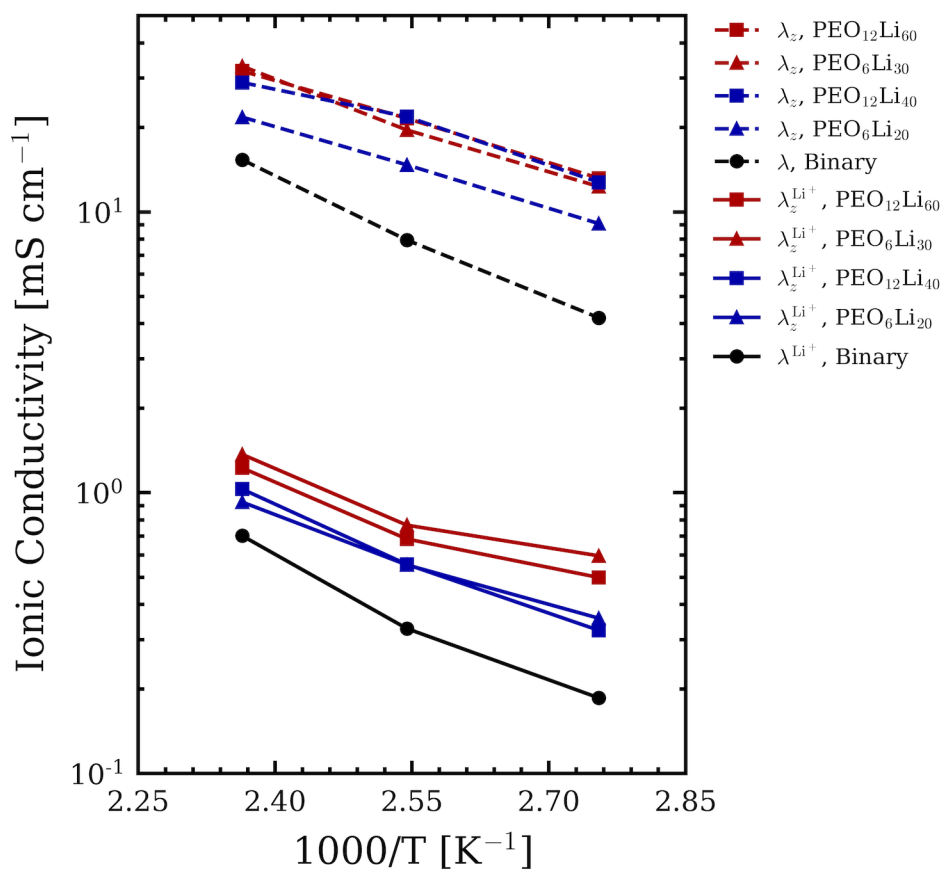


Figure 3-13. Longitudinal ionic conductivities of solution (dashed lines) and Li^+ ions (solid lines) as a function of temperature. Note that the values for binary electrolytes are isotropic conductivities.

3.4. Li ion Transport Mechanism

The residual times of Li⁺ ions at each molecule could be obtained from the result of polarizable MD simulations. From the results, one could directly compare how often the structural diffusion occurred in PEO_xLi_y and binary electrolytes. In addition, single ion trajectory analysis was conducted to elucidate how the Li⁺ coordination structures are distributed and transition to others during the simulation.

3.4.1. Residual Time of Li⁺ ions

The values of residual time τ of Li⁺ ions for the PEO chains and TFSI were calculated, which was defined as the mean lifetime of individual coordination [31], to investigate the transport mechanism of Li⁺ ions. In order to calculate the residual time, the autocorrelation function of the neighbor function, $H(r_{ij}, t)$, should be obtained for all possible coordination as follows:

$$H(r_{ij}, t) = \begin{cases} 0, & \text{if } r_{ij} \geq r_{ij}^c \\ 1, & \text{if } r_{ij} < r_{ij}^c \end{cases} \quad (9)$$

, where r_{ij} is the pair distance between i and j , and r_{ij}^c indicates cutoff distances, which were determined to be 3.0 Å (O_{PEO}) and 5.0 Å (N_{TFSI}) using the endpoints of the first peaks of $g^{\text{Li}^+-\text{O}_{\text{PEO}}}(r, \theta)$ and $g^{\text{Li}^+-\text{N}_{\text{TFSI}}}(r, \theta)$, respectively. Then, the persistence of specific coordination can be demonstrated by the autocorrelation of the neighbor function

$$C(t) = \frac{\sum_{ij}^N \langle H(r_{ij}, t) H(r_{ij}, 0) \rangle}{\sum_{ij}^N \langle H(r_{ij}, 0) H(r_{ij}, 0) \rangle}. \quad (10)$$

Because the Li⁺ ions transition from one binding site to another within the simulation time, the autocorrelation function decays from 1 to 0, which can be fitted to a stretched exponential function, $A \exp(t/\tau_{\text{KWW}})^\beta$, also called Kohlrausch-Williams-

Watts (KWW) function (Figure 3-14). Once the function is confirmed to converge to 0 at a finite time, the residual time τ can be obtained from the integration of this function. Figure 3-15 shows τ^{PEO} and τ^{TFSI} as functions of the temperature in each system. Note that τ^{PEO} is the average time needed for Li^+ to completely detach from the PEO chain, not limited to the oxygen atoms. The magnitudes of τ^{TFSI} increase with the ratio of Li^+ to the PEO chains, while τ^{PEO} decrease. However, the τ^{TFSI} values for all the systems are smaller than the τ^{TFSI} values for the binary electrolytes by a factor of 2. This suggests that the structural diffusion mechanism contributes more to Li^+ dynamics in the nanopores than the binary electrolytes. The magnitudes of τ^{PEO} are greater than those of τ^{TFSI} for the binary electrolytes by a factor of 2–3. The Li^+ ions bound to the PEO chains participate in the diffusion by migration with the PEO chains. More details are discussed in the following section.

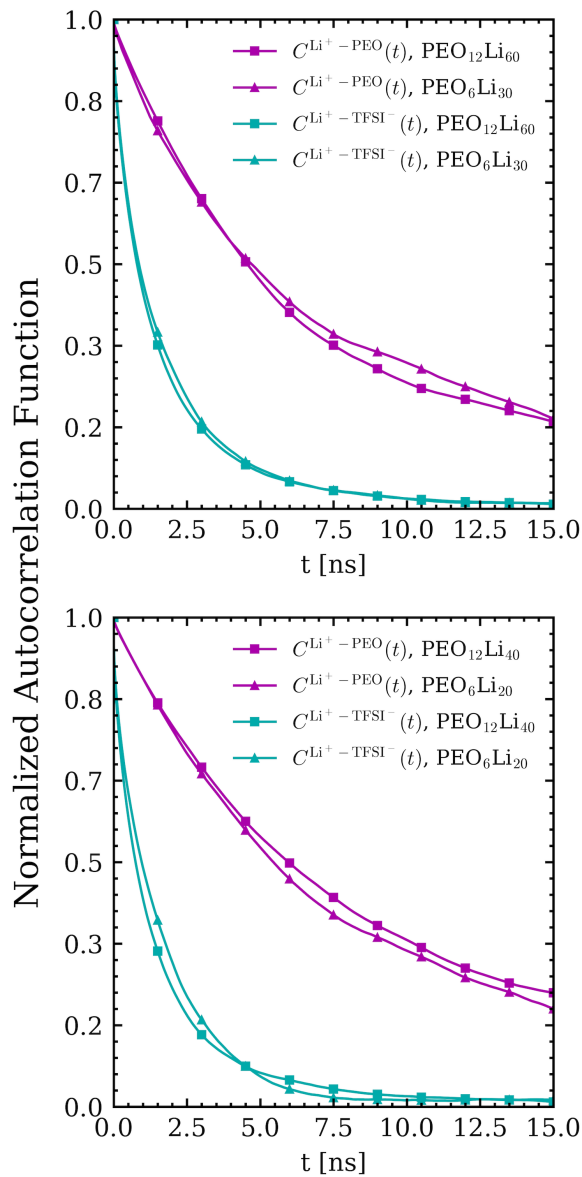


Figure 3-14. Normalized autocorrelation function of neighbor function of Li^+ -PEO (purple lines) and Li^+ -TFSI (cyan lines) for all systems; Top: $\text{PEO}_{12}\text{Li}_{60}$ and $\text{PEO}_6\text{Li}_{30}$, Bottom: $\text{PEO}_{12}\text{Li}_{40}$ and $\text{PEO}_6\text{Li}_{20}$. Each pair in the same figures have the same relative amount of Li^+ ions to PEO chains.

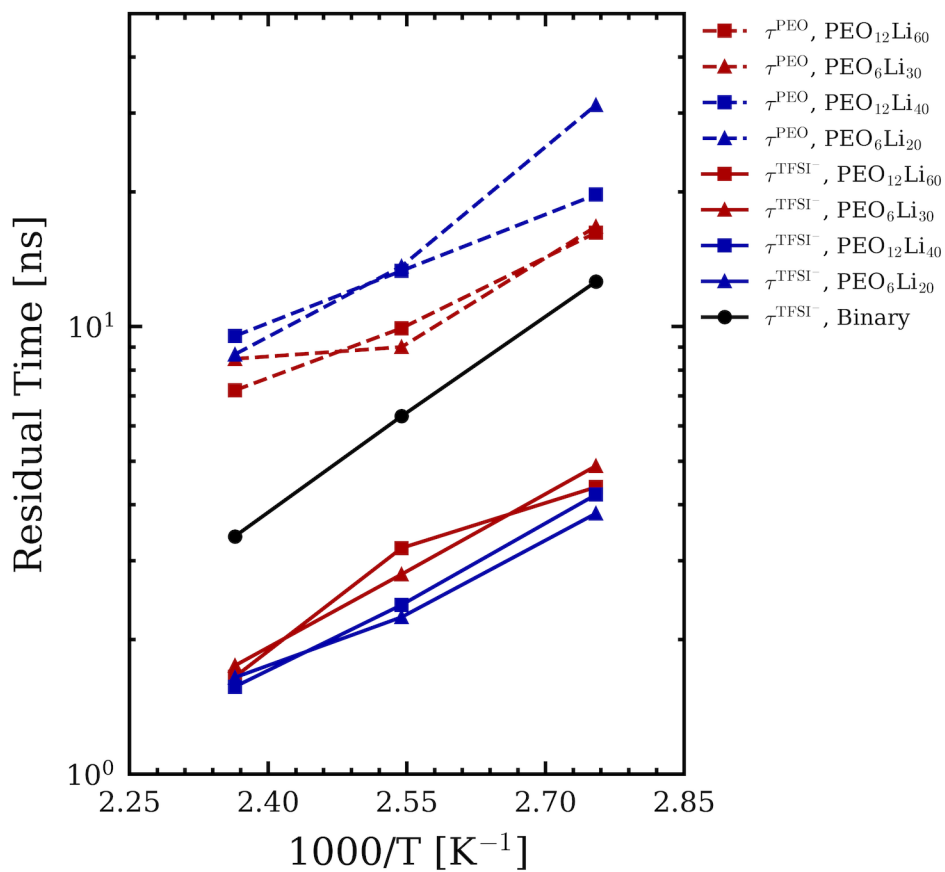


Figure 3-15. Residual times for Li⁺ ions to PEO chains (dashed lines) and TFSI anions (solid lines) as a function of temperature for all systems as well as binary electrolytes.

3.4.2. Single Ion Trajectory Analysis

Single ion trajectory analysis was conducted on Li^+ by tracing the indices of the coordinated species at each frame. According to Brownian dynamics, the probability distribution of the jump displacements over one dimension follows a Gaussian distribution. The distributions of the longitudinal displacements of Li^+ at $\Delta t = 150$ ps also follow a normal distribution (Figure 3-16). According to Figure 3-16, the distribution of displacements in the longitudinal direction is a single normal distribution, which indicates that the Li^+ ion dynamics are governed by a single transport mechanism. It is also noteworthy that the Li^+ ion hopping from one molecule to another is a dynamically refreshing process from the consistency of the ensemble-averaged displacements. By comparing each distribution to a single ion trajectory, the Li^+ ions can be ordered in order of standard deviation of the distribution. We considered the ions with high standard deviation as fast ions and those with low standard deviation as slow ions.

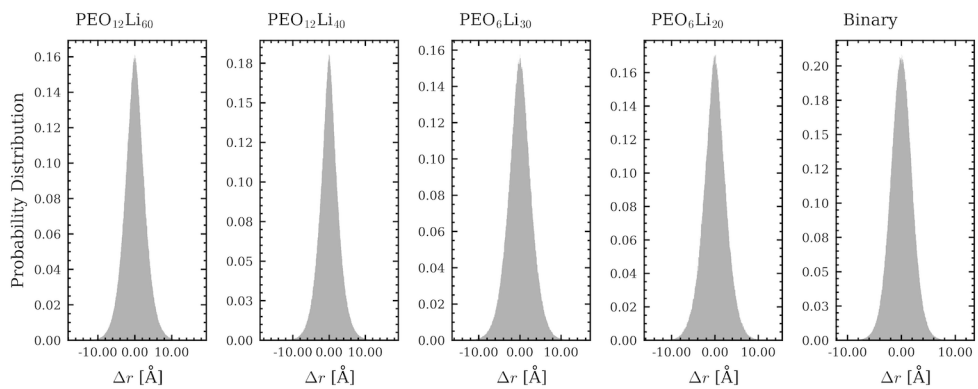


Figure 3-16. Probability distribution of displacement of Li ions (a–d) in PEO_xLi_y systems along the longitudinal direction and (e) binary electrolyte.

Figure 3-17 (a) and (b) show coordination maps for each representative of fast and slow Li^+ ions that indicate which sites the Li^+ ions are bound to during the simulation at 423 K, where ‘binding’ was defined as coordination lasting at least 150 ps. Both fast and slow ions pass through several PEO chains and TFSI anions. Specifically, one of the fast ions in Figure 3-17 (a) migrates as follows: (i) transported with two TFSI anions for 2 ns, (ii) attached to a single PEO chain for 7 ns without TFSI anions, (iii) frequently exchanging many TFSI anions over 20 ns, (iv) attached to another single PEO chain for 5 ns, and (v) exchanging many TFSI anions until the end of the simulation. The slow ion is transported similarly, but the residual time of each segment is longer than that of the fast ion. In particular, more frequent anion exchange occurs before and after binding to the PEO chains. A comparison of the results showed that the Li^+ ions in the binary electrolyte are bound to the same TFSI anions for a longer time, though the ion is fastest in the electrolytes (Figure 3-17 (c)). As a result, the average number of TFSI anions encountered by Li^+ for a unit time at 423 K is greater in the nanopore systems than in the binary electrolyte, with 1.79, 3.08, 2.08, and 2.71 anions for 1 ns for $\text{PEO}_{12}\text{Li}_{60}$, $\text{PEO}_{12}\text{Li}_{40}$, $\text{PEO}_6\text{Li}_{30}$, and $\text{PEO}_6\text{Li}_{20}$, respectively, and 1.18 anions for 1 ns for the binary system. Based on the single ion trajectory analysis results, two distinct features of Li^+ ion transport in nanopores are identified. One is that the Li^+ ions are completely separated into PEO chains or TFSI, except when they transition from PEO chains to TFSI for a short time and *vice versa*. The other is that more frequent anion exchanges for Li^+ ions occur in the nanopores than in the binary electrolytes, which supports the idea that the dynamics of Li^+ ions are accelerated in the nanopores by structural diffusion.

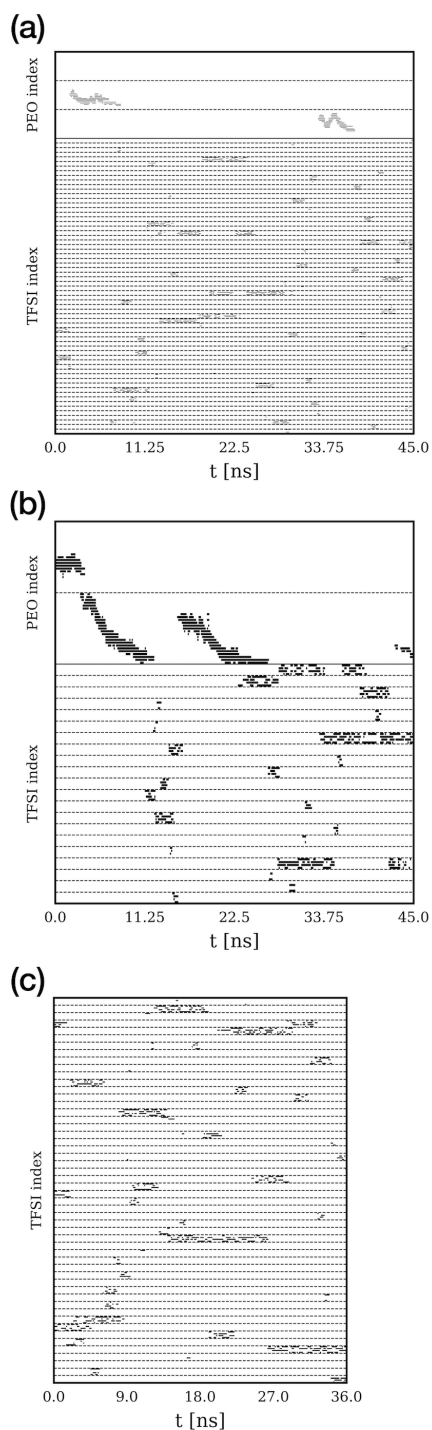


Figure 3-17. Coordination maps for the representative of (a) fast and (b) slow Li^+ ions in the $\text{PEO}_{12}\text{Li}_{60}$ system at 423 K. (c) Coordination map for the fastest ion in the binary electrolyte at 423 K.

An interesting feature was also observed: positional dependency. Figure 3-18 shows the probability distributions of the radial density for fast and slow Li^+ ions. Both profiles exhibit a distinct peak at a few angstroms from the interface between the nanopores and electrolytes, related to forming an electric double layer near the surface. In contrast to slow ions, fast ions can be located at the center of nanopores. This means that anion exchanges frequently occur near the center of the channels, which is favorable in terms of Li^+ transport. A distinct difference in the distributions between the fast and slow ions is observed for $\text{PEO}_{12}\text{Li}_{60}$ and $\text{PEO}_6\text{Li}_{30}$ compared to $\text{PEO}_{12}\text{Li}_{40}$ and $\text{PEO}_6\text{Li}_{20}$ because many Li^+ ions could be present without the PEO chains in the large systems as a result of the higher ratios of Li^+ to the PEO chains.

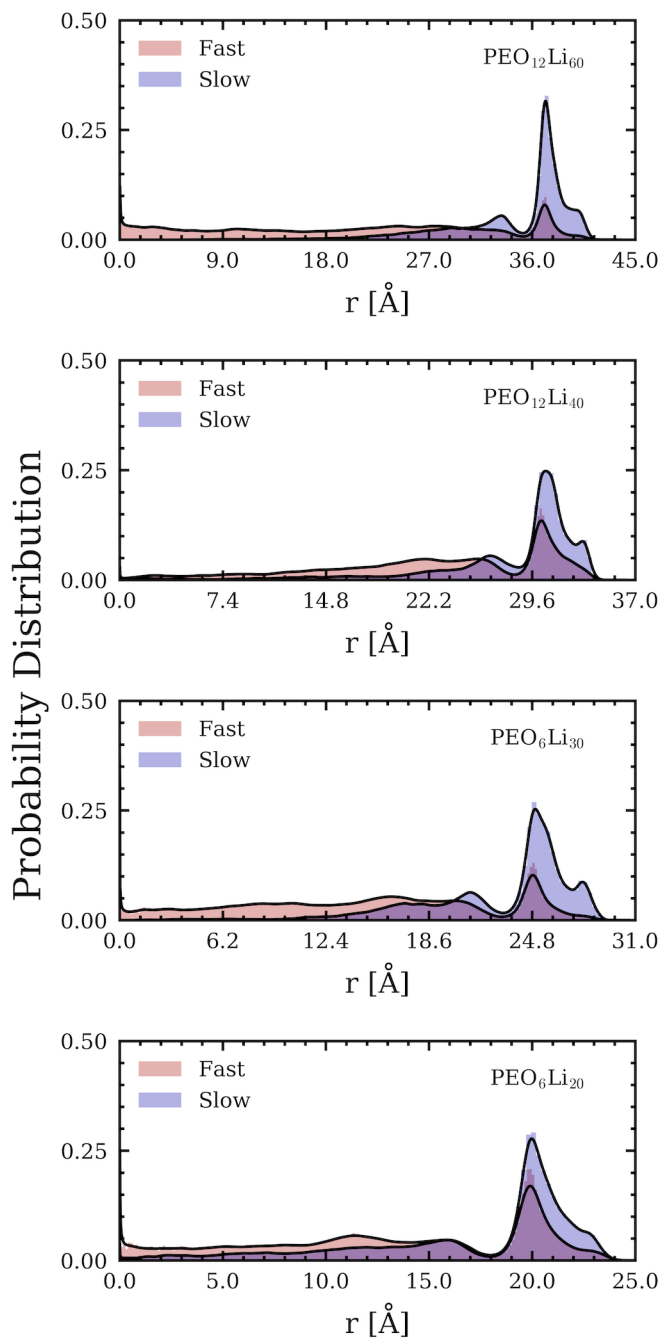


Figure 3-18. Probability distributions for radial density of Li⁺ ions in nanopores at 423 K. $r = 0.0$ means the ions are located at the center of nanopores. 10 fastest and slowest ions were used in averaging for the large systems (PEO₁₂Li₆₀ and PEO₁₂Li₄₀), and 5 ions were used for the small systems (PEO₆Li₃₀ and PEO₆Li₂₀).

3.5. Conclusion

In the present chapter, we have performed many-body polarizable molecular dynamics simulations of a LiTFSI/PYR₁₄TFSI solution in a nanopore where PEO chains were branched and investigated the local environment and transport mechanism of Li⁺. The first coordination shell structure of Li⁺ consisted of TFSI anions and PEO chains. The strength of the Li⁺-TFSI binding directionally depended on the geometry of the nanopores, whereas it did not for Li-PEO. Smaller magnitudes of the peaks of $g^{\text{Li}^+-\text{N}_{\text{TFSI}}}(r, \theta)$ were observed in the longitudinal direction than in the radial direction. The high values for $g^{\text{Li}^+-\text{N}_{\text{TFSI}}}(r, \theta)$ peaks at 3.5 Å suggested the dominant existence of bidentate structures in the Li-TFSI complexes rather than monodentate structures. Therefore, the number of large Li⁺ clusters comprising two or more Li⁺ ions was suppressed compared with the binary electrolytes, and this was confirmed by cluster analysis of $[\text{Li}_x\text{TFSI}_n]^{-(n-x)}$ complexes. In addition, the amount of $[\text{LiTFSI}_2]^-$ complex was greater than that of $[\text{LiTFSI}_3]^-$. Thus, the smaller hydrodynamic radius facilitated the fast Li⁺ ion transport. A sufficiently high ion dissociation in the longitudinal direction allowed for selective charge transfer. Although the ionic conductivities of the electrolytes, λ_z , were equivalent to each other, with the exception of PEO₆Li₂₀, the Li⁺ ion conductivities, $\lambda_z^{\text{Li}^+}$, showed differences. With an increase in the ratios of Li⁺ to the PEO chains and a decrease in the pore sizes, the Li⁺ ion conductivity, $\lambda_z^{\text{Li}^+}$, increased. An examination of residual times τ^{PEO} and τ^{TFSI} showed that more frequent anion exchanges occurred than in the binary electrolytes, which corresponded to the structural diffusion mechanism. The details of this mechanism were confirmed using single ion trajectory analysis. Finally, the Li⁺ ions near the center of nanopores were faster than the ions stuck to

the electric double layer formed at the surface of nanopores.

Chapter 4. Li-ion Dynamics in Ionic Liquids with Zwitterion Additives

In order to obtain better performance of LIBs with ionic liquids, extensive studies have been attempted in various approaches. Adding proper additives to electrolytes is one of the simple methods and increases the heterogeneity of the systems hence the performance of the electrolytes could be expected to be enhanced electrochemically or mechanically. In this chapter, polarizable MD simulations are conducted for binary electrolytes that consist of Li^+ salt and ionic liquids ($\text{LiTFSI/PYR}_{14}\text{TFSI}$ and $\text{LiFSI/PYR}_{14}\text{FSI}$) with the compound containing a PYR_{14} cation and a TFSI anion in the same molecule, denoted as a 'zwitterion'. Since there have been no theoretical studies on the zwitterions, molecular modeling for polarizable MD simulations is also conducted, and the procedure is introduced. As the zwitterions have the same functional groups of $\text{PYR}_{14}\text{TFSI}$ ionic liquids, it is expected to solvate well for the zwitterions in $\text{PYR}_{14}\text{TFSI}$ compared to $\text{PYR}_{14}\text{FSI}$. In addition, the compound has a strong molecular dipole moment that affects to rotational relaxation of electrolytes, which could lead to variations in the system dynamics. In order to estimate the impact of zwitterions on the electrolytes, structural and dynamical observations are obtained and discussed as in Chapter 3. In contrast with the previous chapter, the polarizable MD simulations were conducted through a different software package to enable GPU acceleration, enabling the implementation of APPLE&P force field through in-house modification. This chapter introduces the details of modification and how faster the implementation is compared to before.

4.1. Materials

In contrast with Chapter 3, the zwitterion in the present study has not been conventionally used. Here, the structural and chemical information of this compound is briefly introduced as well as anions. In addition, the procedure of fitting force parameters for polarizable force field is summarized for some missing parameters near the covalent bond of the zwitterion in APPLE&P force field.

4.1.1. Chemical Information

Figure 4-1 and Figure 4-2 illustrate the chemical structures of the anions and the zwitterion, respectively. The anions are commonly used in previous studies because of their high charge delocalization effect and the fluorene-based functional groups.

The compound shown in Figure 4-2 (a) consists of a covalent bond between a carbon atom at the end of the butyl chain of PYR_{14} cations and a carbon atom of one of the $(-\text{CF}_3)$ group of TFSI anions in that it can be called a ‘zwitterion’. Unlike other zwitterions, such as amino acids, the two ions from aprotic ionic liquids prevent this compound from having an either positive or negative charge. Therefore, the zwitterions behave as charge-neutral molecules in electrolytes, and at the same time, their molecular dipole moment is significantly greater than any other compounds in the electrolytes.

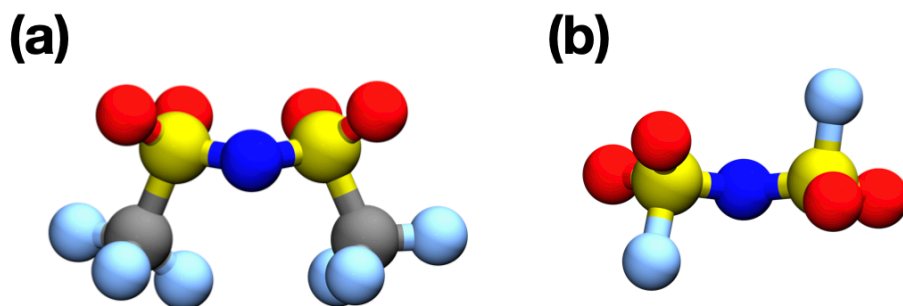


Figure 4-1. An illustration of anions used in the present chapter: (a) bis(trifluoromethanesulfonyl)imide (TFSI), (b) bis(fluorosulfonyl)imide (FSI).

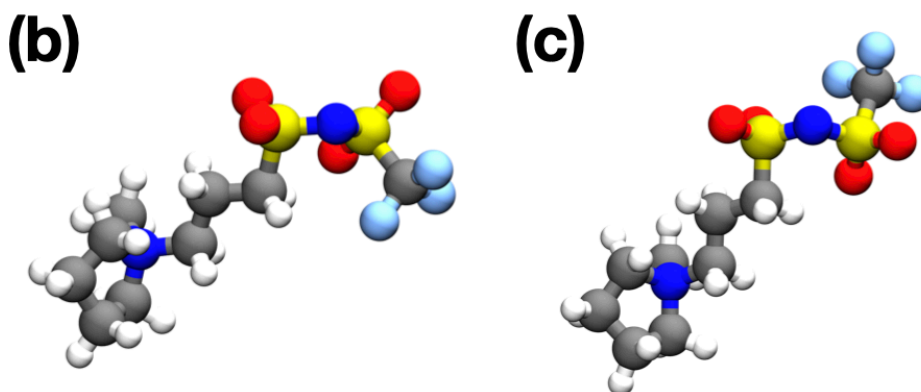
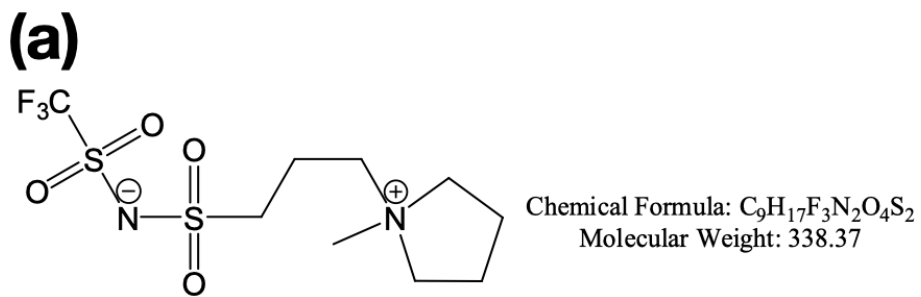


Figure 4-2. (a) Chemical structure and information of the zwitterion. (b), (c) Illustrations of the zwitterion conformers used in partial charge optimization. The anionic functional group forms: (b) *cis* conformer and (c) *trans* conformer.

4.1.2. Procedure to Fit New Force Parameters

Even though most of the force parameters could be transferred from the APPLE&P force field because the atoms in the zwitterion are identical to those of PYR₁₄ or TFSI, the partial charge set should be recalculated entirely because of the change of electron distribution near the molecule. In this study, ESP charge fitting method was used with considering polarizable effects as APPLE&P force parameters developed [30]. Partial charge set could be obtained by minimizing the following objective function χ :

$$\chi^2(\vec{q}) = \sum_i^M \left[\sum_j^{N_{\text{GRID}}} \frac{\omega^\phi}{N_{\text{GRID}}} \left(\phi_{ij}^{\text{QM}} - \phi_{ij}^{\text{FF}}(\vec{q}) \right)^2 + \omega^{\vec{\mu}} \left(\vec{\mu}_i^{\text{QC}} - \vec{\mu}_i^{\text{FF}}(\vec{q}) \right)^2 \right] \quad (11)$$

, where \vec{q} denotes the partial charge set, the superscript of QM and FF denote that the observations come from the quantum mechanics and molecular mechanics by polarizable force fields, respectively. The quantum mechanics calculations were performed on MP2/cc-pvdz level by GAUSSIAN 16 software package [55]. for the representative canonical conformers (denoted as j in the above equation, and the number of conformers = M) of the zwitterion. Many conformers are possible due to the alkyl chain rotation, but in this study, the alkyl chain is supposed to be linear in that two conformers are used to fit the charge set: *cis* and *trans* conformers of the anionic functional group (Figure 4-2 (b, c)). From the results of the MP2 calculation of each conformer, the electrostatic potentials at evenly spaced points ($\sim 10^5 = N_{\text{GRID}}$, denoted as i in the above equation) near the conformers are calculated except for the points within vdW radius of each atom. It is noteworthy that the objective function includes the terms to fit molecular dipole moments as well, denoted as $\vec{\mu}$ in the above. In contrast with the fitting procedure for non-polarizable force fields,

intramolecular polarization effects are counted in the charge fitting procedure, and the calculation could be done by solving analytic equations or iterative ways [56]. As the point dipoles obtained from the intramolecular polarization also influence molecular dipole moments, the explicit fitting term for molecular dipole moments should be included to make the partial charge set predict the molecular dipole moments well with polarization effects in MD simulations. In this study, the iterative method was used to include intramolecular polarization effects while fitting the partial charge set. Table 4-1 shows the fitted partial charge set of the zwitterion.^⑨

^⑨ Distribution of publication of the force parameters in APPLE&P force fields is prohibited by the license agreement of the force field.

Table 4-1. Partial charge set optimized by induced point dipole polarization model

Atom Label	<i>q</i>	Atom Label	<i>q</i>
N ⁺	0.2750	N ⁻	-0.8221
C(N ⁺)	0.1615	S(-CH ₂ -)	1.0674
C(ring)	0.0501	S(-CF ₃)	1.1322
C(CH ₃ -)	-0.2937	O(S(-CH ₂ -))	-0.5078
C(R)	0.0426	O(S(-CF ₃))	-0.5620
C(S)	-0.2508	Lp	-0.2159
C(CF ₃ -)	0.9760	F	-0.3280
H	0.0000		
H(C(CH ₃ -))	0.1410		
H(C(R))	0.1025		

In addition to the partial charge set, there are a few missing force parameters for intramolecular bonded potentials relevant to the connecting covalent bond, and the related bonded atom sets are described in Figure 4-3 (a). Fortunately, the parameters for bond and angle potentials could be transferred from those of similar structures in APPLE&P force field except for the [N]-S-C(alkyl chain) angle. The obtained optimal angle from the *ab initio* calculation was about 10 degrees higher than the other side^⑩ due to the different electron densities of the carbon. There were also no possible parameters to be transferred for the torsional angle potentials of N-S-C-C and N-S-C-H, hence their force parameters were fitted by the following procedure. Relaxed potential energy surfaces (PES) by each torsional angle were obtained from the GAUSSIAN 16 software package and steepest descent algorithm with the polarizable force field without the target torsional potential, respectively. Subsequently, the difference between two PES is fitted to the following periodic torsional potential equation:

$$U(r) = \frac{1}{2} \sum_n k_n (1 - \cos(n\phi - \phi_s)) \quad (12)$$

, where n denotes periodicity, k_n denotes the force constant for n -th cos function, and ϕ_s denotes the shift angle.^⑪ Figure 4-3 (b) and (c) plot the fitted PES to those from the *ab initio* calculations.

^⑩ The other carbon has fluorenes, whereas this carbon has an alkyl group and hydrogens.

^⑪ In APPLE&P, the values of shift angles are always 0 for all dihedral parameters.

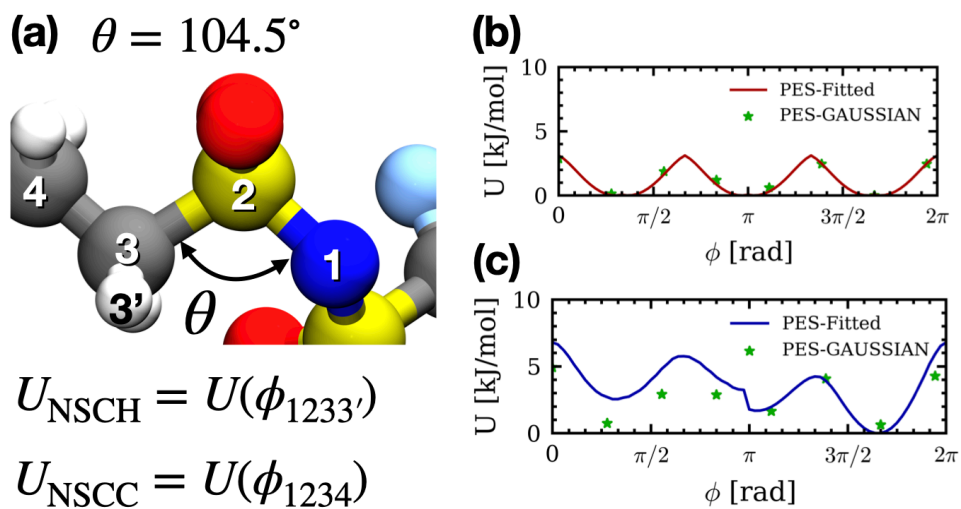


Figure 4-3. (a) Information about missing force parameters. (b), (c) Torsional potential of NSCH and NSCC, respectively, which parameters fitted to the results of *ab initio* calculation.

4.2. Computational Method

4.2.1. Modification of OpenMM Software Package

Instead of WMI-MD, a modified OpenMM software package was used in this chapter to implement polarizable MD simulations with APPLE&P force field with GPU acceleration. OpenMM is a software package for molecular dynamics simulations [57], and it was developed in recent days^⑫ compared to other software such as LAMMPS or GROMACS. It features a collection of APIs mainly written in C++, allowing users to customize conveniently and develop their own simulation packages. OpenMM supports Python wrappers to implement MD simulations conveniently for users who are not interested in development. It also has an advantage in more efficient parallelization, especially GPU utilization.

The modification was conducted by building a new plugin of OpenMM for APPLE&P force field based on the previous plugin in OpenMM for the AMOEBA force field which is also known as one of the polarizable force fields with induced point dipoles. Parallelization kernels were well developed in that the modification was conducted on device-level functions. In the nonbonded interaction, 12-6 Lennard-Jones potential was replaced with Buckingham potential with a switch function to make the potential smoothly converged to zero at cutoff distance. Electrostatic interactions by fixed molecular multipoles are unnecessary in APPLE&P force field hence they are eliminated to increase performance. Figure 4-4 shows the benchmarks and simulation results for LiX/PYR₁₄X [X=TFPI, FSI, and BF₄] electrolyte systems at 363 K compared to WMI-MD. This suggests that modified OpenMM produces accurate results in a shorter time.

^⑫ Early 2010

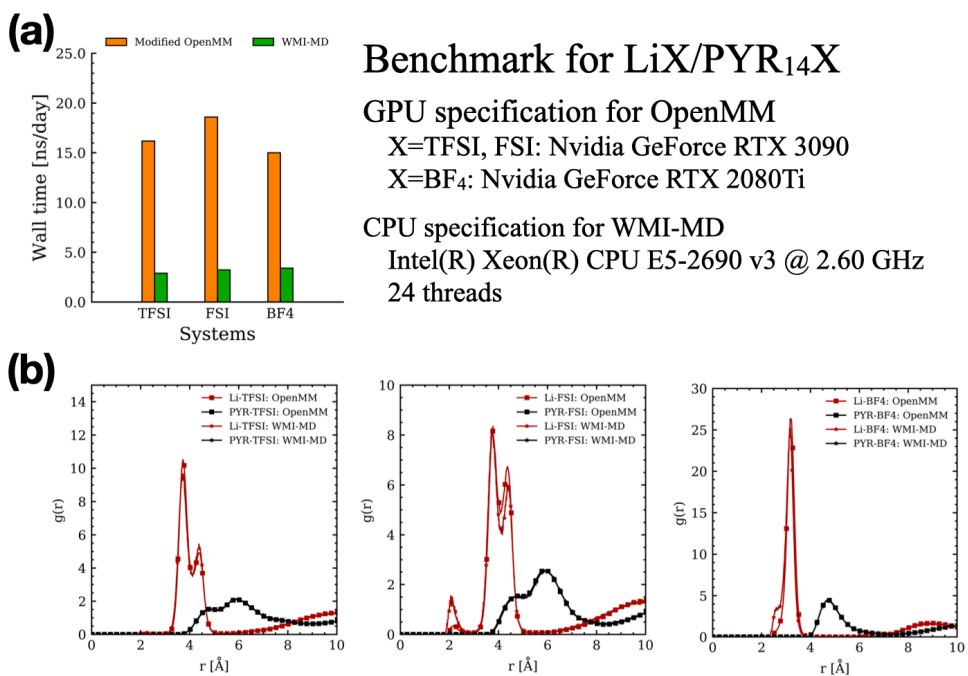


Figure 4-4. Benchmark and validation results for the modified OpenMM: (a) Benchmark result and information (b) Comparison of radial distribution functions of Li-X and PYR₁₄-X

4.2.2. Polarizable Molecular Dynamics Simulation

For binary electrolytes, 30 LiX salts and 180 PYR₁₄X [X = TFSI or FSI] ionic liquids were located in three-dimensional periodic simulation cells. For electrolytes with zwitterions, 5, 10, and 15 of ionic liquids were replaced with zwitterions to compensate for the number of functional groups in each system. As the cation of ionic liquids is fixed to PYR₁₄, abbreviated notation with the first letter of Li⁺, anions, and zwitterions would be used in this study for convenience, i.e., LTz5 = LiTFSI/PYR₁₄TFSI with 5 zwitterions.

Most force parameters were transferred from the APPLE&P force field except those discussed in the previous section. In contrast with Chapter 3, the long-range electrostatic interactions were evaluated as particle mesh Ewald (PME) summation for not only charge–charge, and charge–induced dipole, but also induced dipole–induced dipole. Nose-Hoover integrator was used to perform time integration every 1.5 fs and keep the temperature of the systems to 333, 363, 393, and 423 K. After energy minimization procedure, equilibration was done for about 10 ns at NPT ensemble with Monte Carlo barostat to optimize simulation boxes. Additional 30–60 ns NVT simulations from the equilibrated structures were performed for data production.

4.3. Structural Properties

As mentioned in Chapter 3, ion transport and coordination structures are strongly related. In the present section, the densities and the pair distributions between all possible pairs of the electrolytes are compared to elucidate the contribution of the zwitterions. In addition, statistical analysis for each ion cluster in the electrolytes

was performed via cluster analysis.

4.3.1. Density of the Electrolytes

Figure 4-5 plots the density profiles as the function of temperature of LTz and LFz electrolytes. The densities show almost linear relationships with temperatures and tend to increase with the fraction of zwitterions in each electrolyte. However, the degree of increment varies depending on the anions. LTz electrolytes, where the negative functional group of zwitterions is identical to the TFSI anions, are less sensitive for the number of zwitterions, and LTz5 electrolytes show equivalent density profiles to the binary electrolytes. On the other hand, the density profiles of LFz electrolytes distinctly increased by the zwitterions. This can be caused by the heterogeneity of components or heavy molar weights of zwitterions, yet the contribution of zwitterions is vague hence further investigation on structural properties is required.

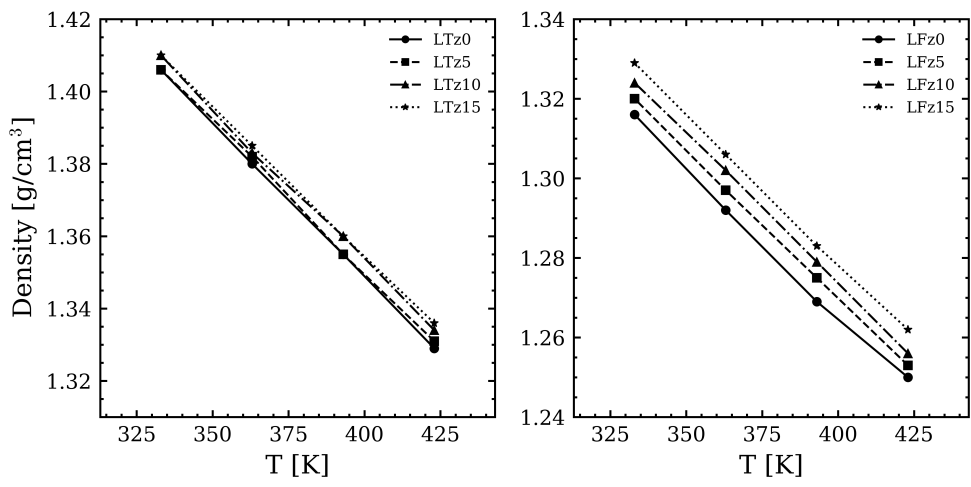


Figure 4-5. Density of the electrolytes as the function of temperatures. Left: LTz, and Right: LFz.

4.3.2. Pair Distribution Functions

In Chapter 3, angle radial distribution functions were used to investigate local environments near Li^+ ions. More specifically, the results showed how Li^+ ions coordinate with their counter-charged atoms or molecules by pair distances and angles to the cylindrical geometry. On the other hand, the systems in the present chapter are isotropic, and the pair correlations are also expected to be equivalent by the angle of pair vectors. The following equation indicates radial distribution function (RDF), $g(r)$:

$$g(r) = \frac{1}{\langle \rho \rangle_{\text{local}}} \sum \frac{\delta(r_{ij} - r)}{4\pi r^2} \quad (13)$$

. With $g(r)$, the first coordination shell of Li^+ could be investigated. Figure 4-6 and Figure 4-7 show the RDFs of Li^+ - N_{anion} , ($g^{\text{Li}^+-\text{N}_{\text{TFSI}}}(r)$ or $g^{\text{Li}^+-\text{N}_{\text{FSI}}}(r)$), Li^+ - N_{zwit} ($g^{\text{Li}^+-\text{N}_{\text{zwit}}}(r)$), and Li^+ - Li^+ ($g^{\text{Li}^+-\text{Li}^+}(r)$) for LTz and LFz electrolytes, respectively. As known already, $g^{\text{Li}^+-\text{N}_{\text{TFSI}}}(r)$ and $g^{\text{Li}^+-\text{N}_{\text{FSI}}}(r)$ show two distinct peaks which indicate bidentate (~ 3.5 Å) and monodentate (~ 4.5 Å) coordination phases, respectively. For LTz electrolytes, the magnitude of the former peaks is greater than the latter peaks, whereas the two peaks are similar or the latter peaks are greater than others in LFz electrolytes. This suggests that the two electrolytes have different distributions of coordinate phases of Li^+ with anions. Once a Li^+ -anion complex, $[\text{LiX}_n]^{-(n-1)}$, tries to make additional coordination with another anion, FSI⁻ can infiltrate and eventually make new coordination due to the low steric hindrance compared to TFSI⁻. With the negatively charged functional group, the zwitterions can also coordinate with Li^+ ions at slightly shorter distances than anions. It is noted that the magnitudes of $g^{\text{Li}^+-\text{N}_{\text{zwit}}}(r)$ are much greater than $g^{\text{Li}^+-\text{N}_{\text{TFSI}}}(r)$ or

$g^{\text{Li}^+-\text{N}_{\text{FSI}}}(r)$, which means the higher potential of mean force of Li-zwitterions than Li-anions. As mentioned in Section 4.1.1. Chemical Information, the results of *ab initio* calculations indicate strong molecular dipole moments of zwitterions, and the dipole moments were included in the partial charge fitting. This can explain the higher magnitudes of partial charges of the zwitterions compared to the anions. The outline of $g^{\text{Li}^+-\text{N}_{\text{zwit}}}(r)$ graphs can be found in the inset plots of Figure 4-6 and Figure 4-7. It is interesting that the relative peak magnitudes for bidentate and monodentate are different in each electrolyte though the same zwitterions are introduced. This is also can be attributed to the low bulkiness of FSI compared to TFSI.

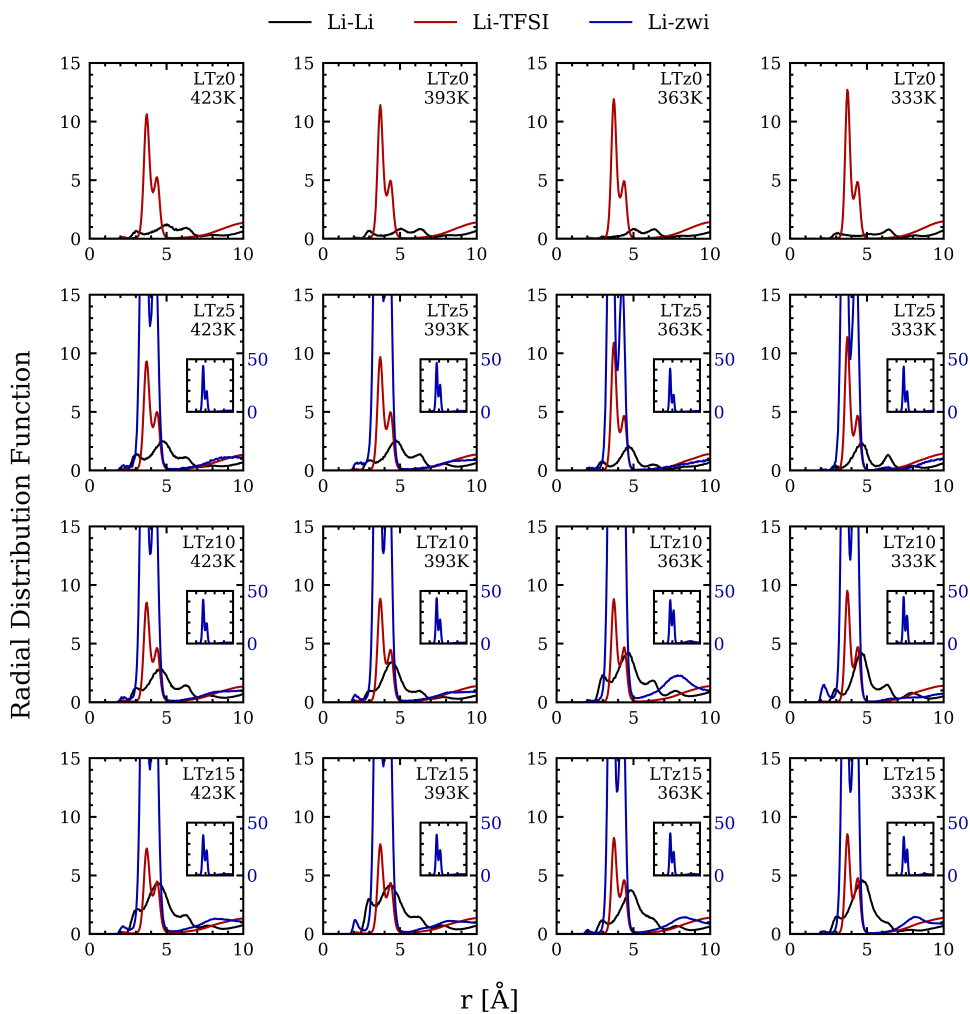


Figure 4-6. Radial distribution functions between Li^+ ions to other molecules in LTz electrolytes. Insets: Radial distribution functions between Li^+ ions to zwitterions.

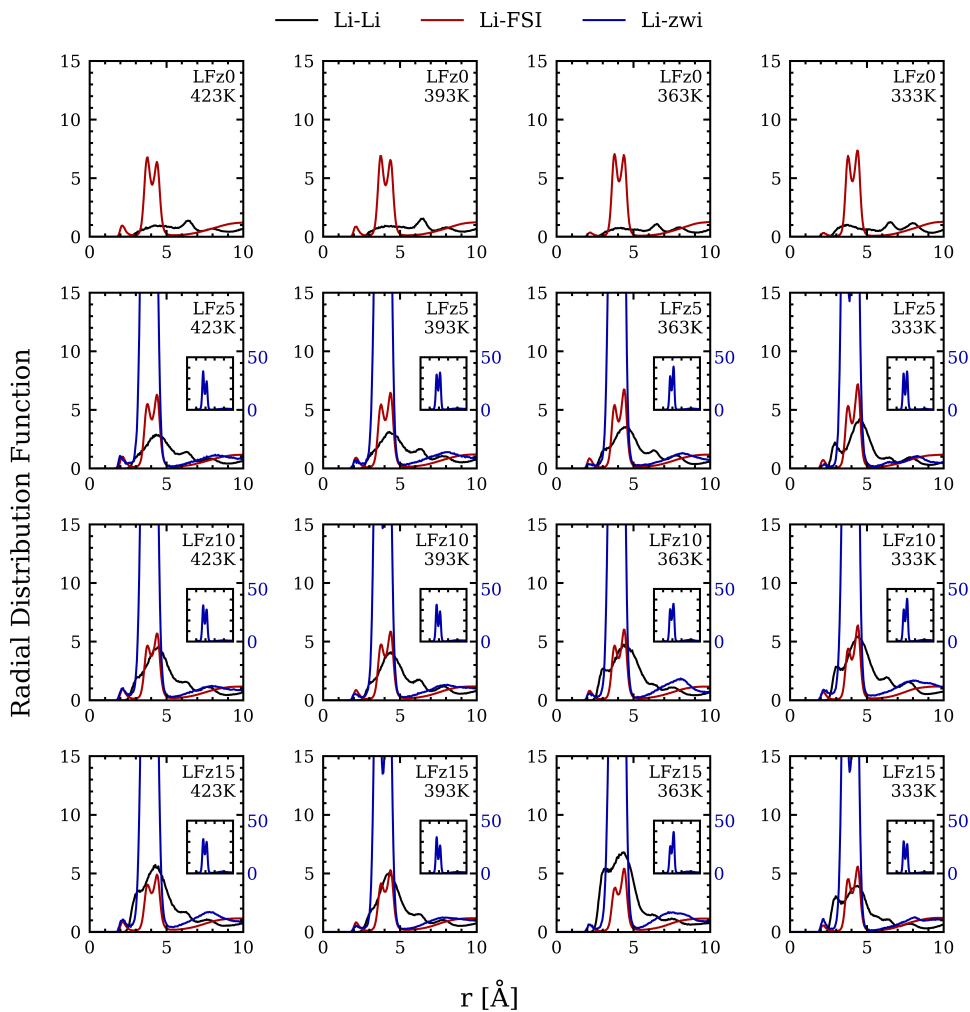


Figure 4-7. Radial distribution function between Li^+ ions to other molecules in LFz electrolytes. Insets: Radial distribution functions between Li^+ ions to zwitterions.

The introduction of the zwitterions changes all the RDFs related to Li^+ ions of electrolytes. More specifically, the first coordination shells of Li^+ ions are transformed to facilitate the formation of large ion clusters. The presence of monodentate encourages the anions to coordinate with two Li^+ ions. In this regard, the ratio of the magnitude of second peaks to first peaks of $g^{\text{Li}^+-\text{N}_{\text{TFSI}}}(r)$ or $g^{\text{Li}^+-\text{N}_{\text{FSI}}}(r)$ are plotted by the number of zwitterions in electrolytes in Figure 4-8. The ratio tends to increase with the fraction of zwitterions, and the gradient is more remarkable in LFz electrolytes. Especially, the peaks for monodentate are greater than bidentate in most of the LFz electrolytes. It is also interesting that the temperature dependent is opposite for both electrolytes, which means the bidentate is more stable than monodentate in the LTz electrolytes and not in the LFz electrolytes. This argument can be supported by confirmation of $g^{\text{Li}^+-\text{Li}^+}(r)$ by the concentration of zwitterions. Figure 4-9 shows the RDF of Li^+-Li^+ at 423 K for the two electrolytes. The values increase with the fraction of zwitterions, and the differences are more distinct in the LFz electrolytes compared to the LTz electrolytes.

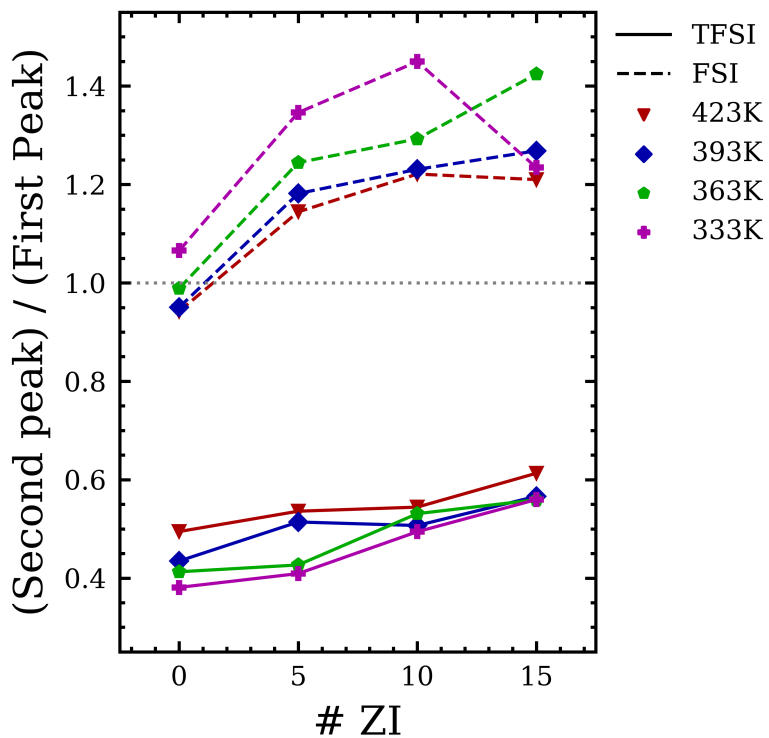


Figure 4-8. Ratio of second peaks to first peaks of radial distribution functions of Li-TFSI (solid lines) and Li-FSI (dashed lines). The grey line indicates that the two peaks are identical.

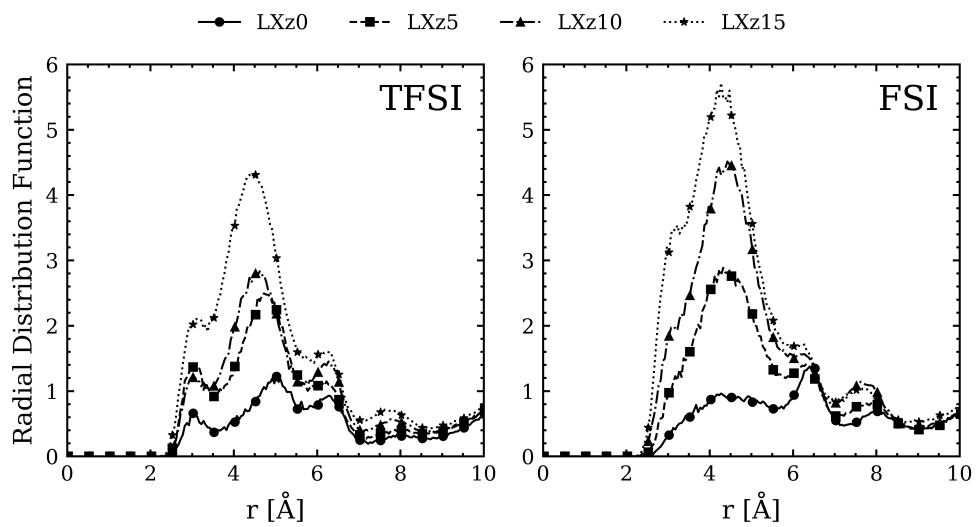


Figure 4-9. Radial distribution functions of Li-Li at 423 K for LTz electrolytes (Left) and LFz (Right) electrolytes.

4.3.3. Net charge of ion clusters

A cluster analysis was performed to intensively investigate the local environment of Li^+ ions, which also can be a good insight into uncovering the dynamical behaviors of Li^+ ions. As in Chapter 3, cutoff distances were determined from the RDF of Li^+ ions with anions and zwitterions, and then distance arrays were constructed with the cutoff distance by MDAnalysis software package. Finally, the clustering information was obtained with the distance arrays by NetworkX. The following features were calculated from the cluster analysis: (i) a_{ij} , a matrix that indicates the probability distribution of clusters composed of Li^+ ions (index i) and anions (TFSI or FSI, index j); (ii) net charge of each ion cluster as a function of the number of zwitterions in the cluster; and (iii) the size of the clusters in (ii).

Figure 4-10–Figure 4-13 and Figure 4-14–Figure 4-17 show the matrix a_{ij} at all temperatures for LTz and LFz electrolytes, respectively. The values in each square indicate the probability of the clusters corresponding a_{ij} , and the negative sign is given when $j > i$. It is noted that the distribution was normalized by the fraction of the most prevalent phase, a_{13} , also denoted for $[\text{LiX}_3]^{-2}$. The only a_{ij} greater than 0.001 are presented in the figures. As known in the previous studies, Li^+ ions are present in the form of negatively charged clusters rather than positively charged for all electrolytes. For all cases, the probabilities shift to the left as the number of zwitterions increases, which means the magnitudes of net charge of each ion cluster are reduced by introducing neutral molecules. In addition, for $i \geq 2$ clusters, some ion clusters are positively charged with high fractions of zwitterions in electrolytes. At the same time, the probabilities for the ion clusters of $i \geq 3$ seem to be increased, and thus the average size of ion clusters may be increased. These features are more

prominent in LFz electrolytes in that the electrolytes with only five zwitterions have positive clusters at 423 K, or a higher amount of a_{43} clusters in LFz15 electrolytes at low temperatures are significantly increased compared to other electrolytes.

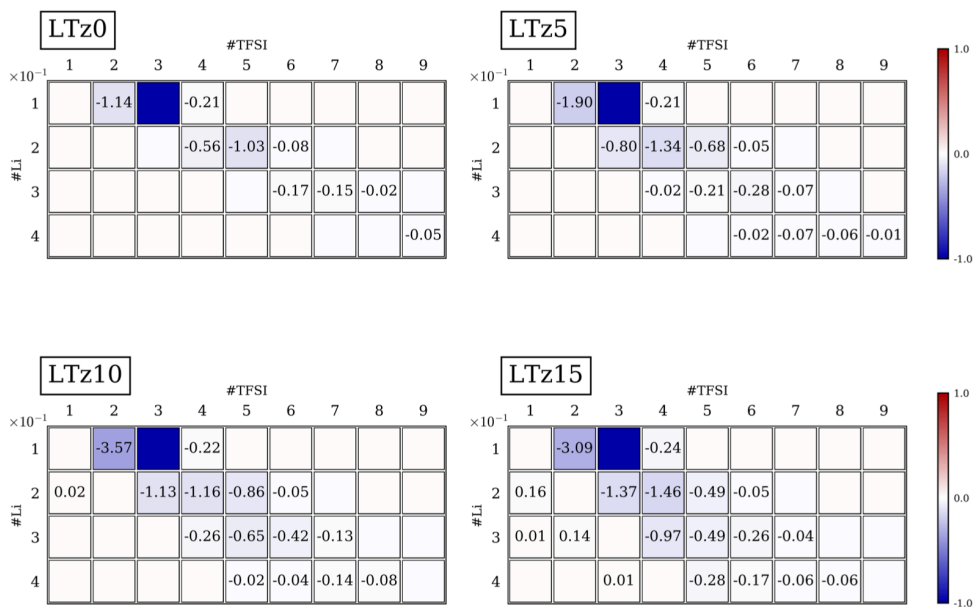


Figure 4-10. Probability distribution array of a_{ij} for $[Li_xTFSI_n]^{-(n-x)}$ clusters in LTz electrolytes at 423 K.

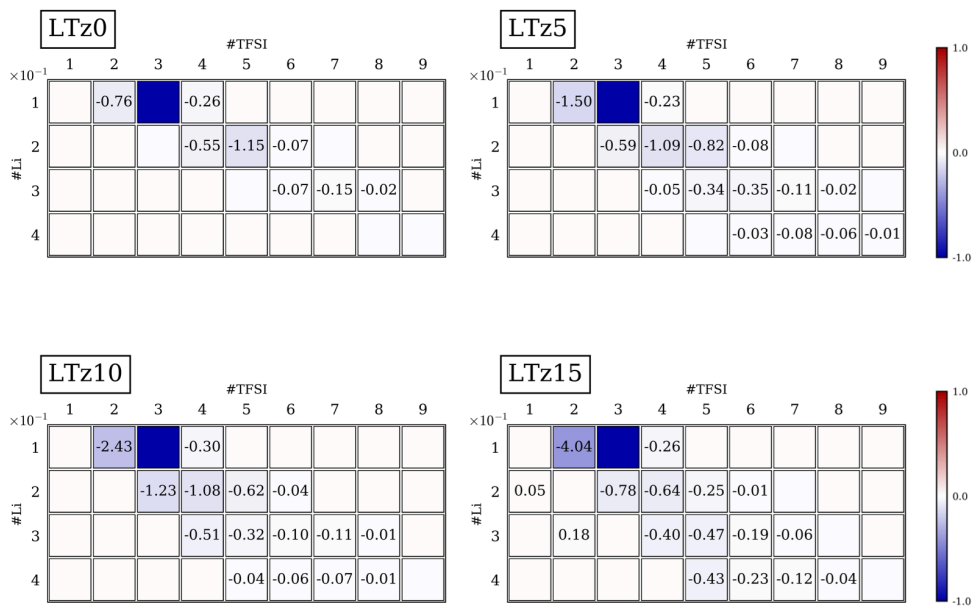


Figure 4-11. Probability distribution array of a_{ij} for $[Li_xTFSI_n]^{-(n-x)}$ clusters in LTz electrolytes at 393 K.

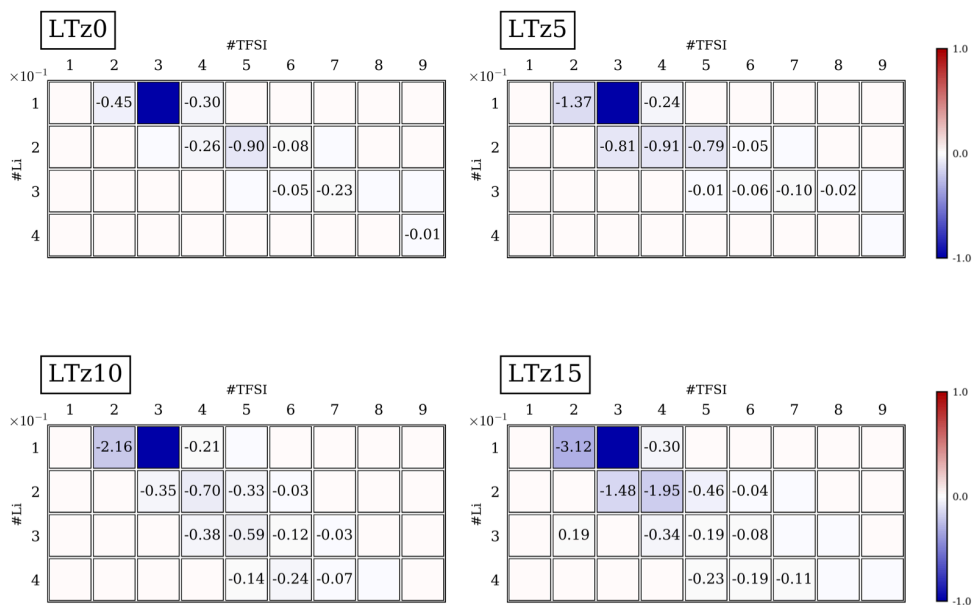


Figure 4-12. Probability distribution array of a_{ij} for $[\text{Li}_x\text{TFSI}_n]^{-(n-x)}$ clusters in LTz electrolytes at 363 K.

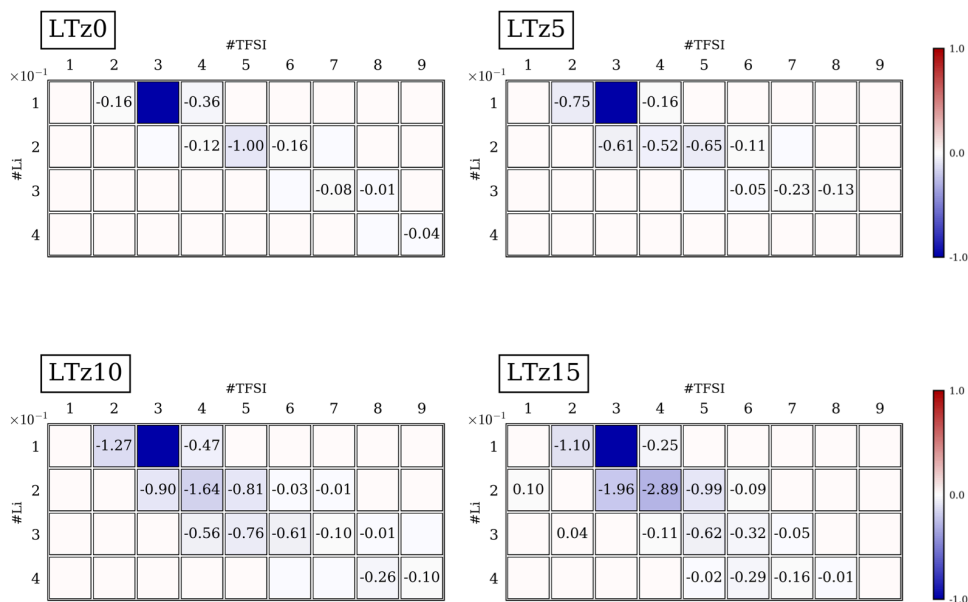


Figure 4-13. Probability distribution array of a_{ij} for $[\text{Li}_x\text{TFSI}_n]^{-(n-x)}$ clusters in LTz electrolytes at 333 K.

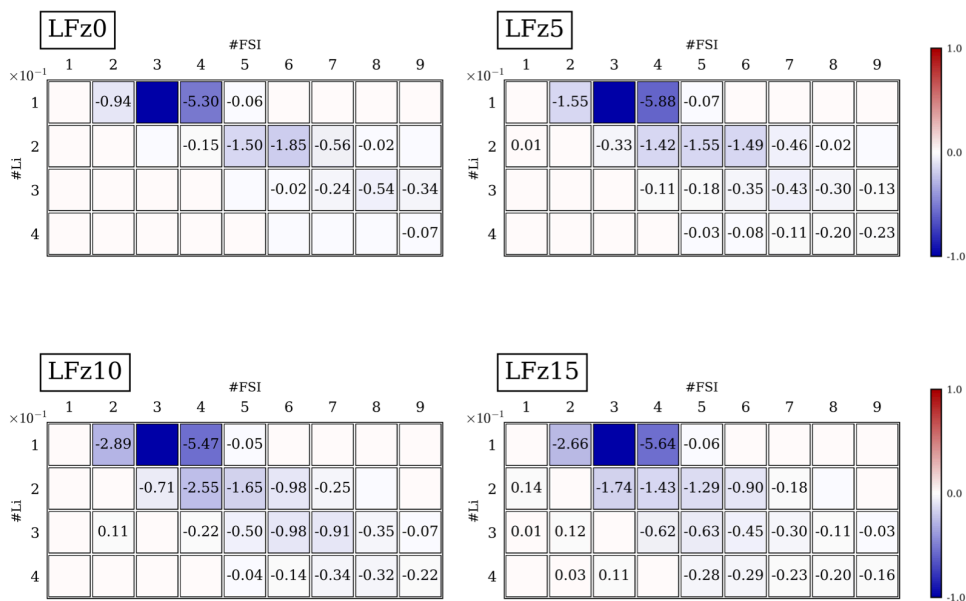


Figure 4-14. Probability distribution array of a_{ij} for $[\text{Li}_x\text{FSI}_n]^{-(n-x)}$ clusters in LFz electrolytes at 423 K.

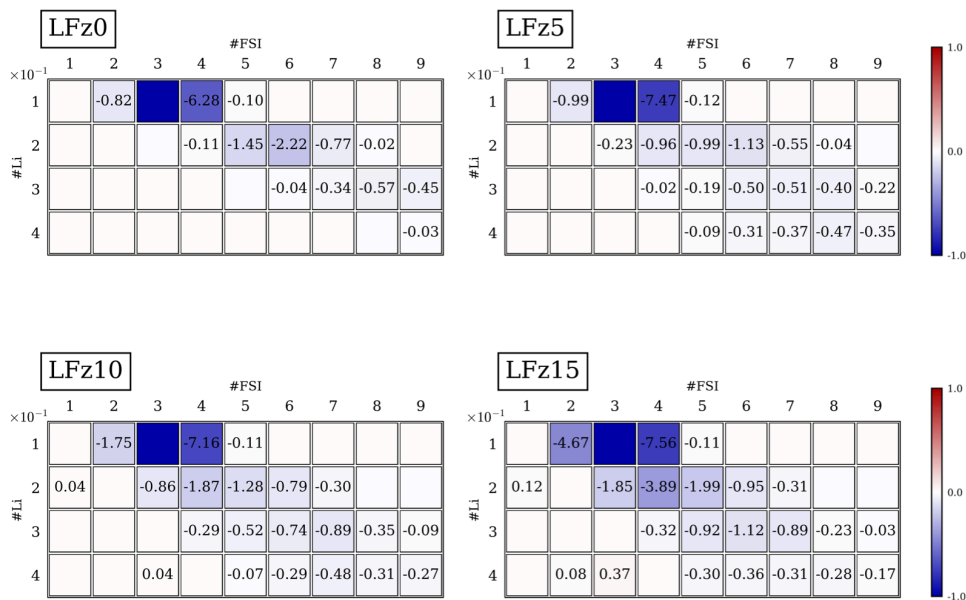


Figure 4-15. Probability distribution array of a_{ij} for $[\text{Li}_x\text{FSI}_n]^{-(n-x)}$ clusters in LFz electrolytes at 393 K.

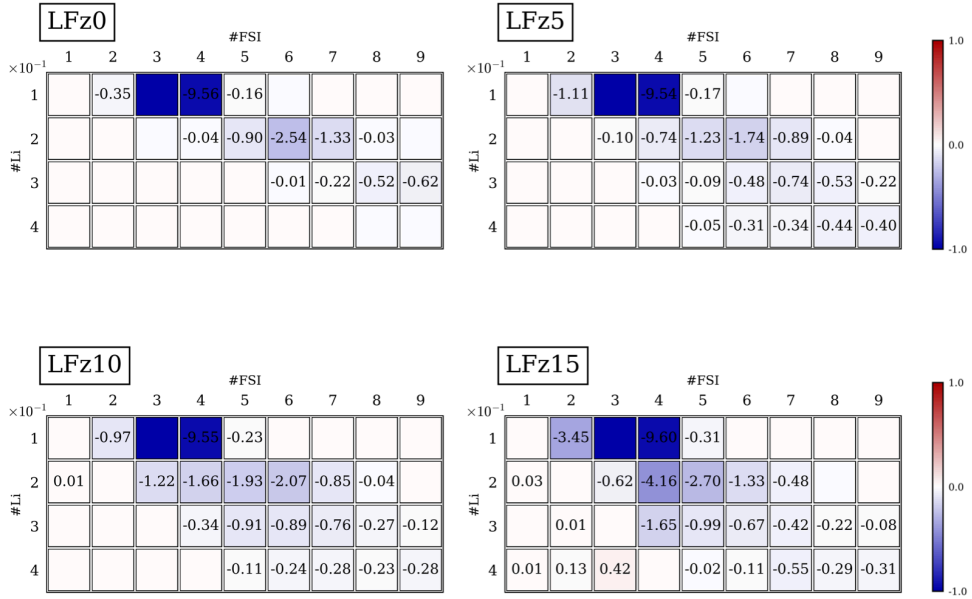


Figure 4-16. Probability distribution array of a_{ij} for $[\text{Li}_x\text{FSI}_n]^{-(n-x)}$ clusters in LFz electrolytes at 363 K.

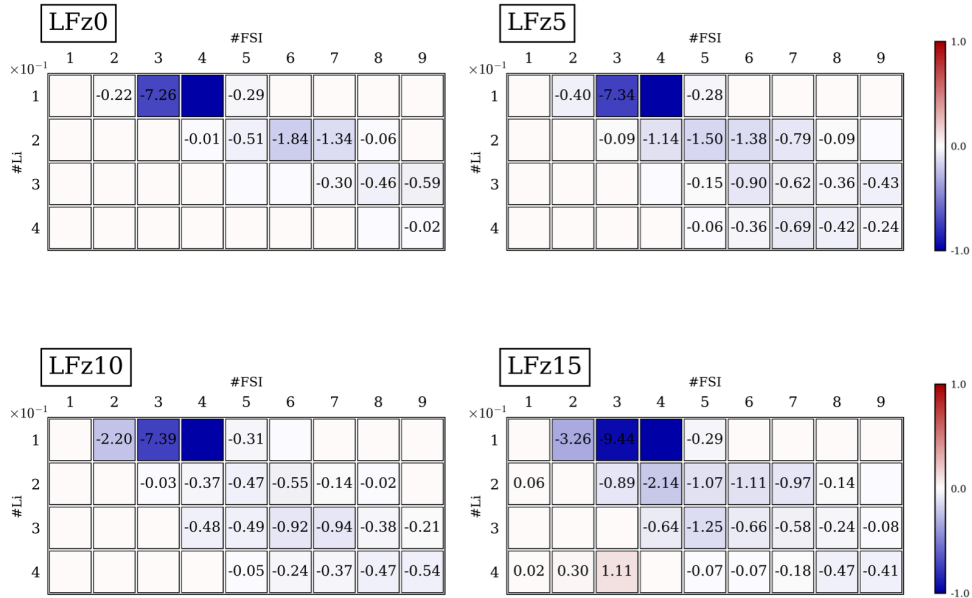


Figure 4-17. Probability distribution array of a_{ij} for $[\text{Li}_x\text{FSI}_n]^{-(n-x)}$ clusters in LFz electrolytes at 333 K.

In order to investigate more clearly, the cluster sizes and net charge of each cluster are calculated as the function of the number of zwitterions, and they are given in Figure 4-18 and Figure 4-19. As expected, the average cluster sizes are increased, and the negative charges of ion clusters are reduced as more zwitterions are substituted in LTz electrolytes. The formation of large clusters with two or more zwitterions is also observed for LTz10 and LTz15 electrolytes but not for LTz5 electrolytes due to the relatively small fraction of zwitterions. In other words, five zwitterions are subtle to perturb thermodynamical behaviors of binary electrolytes for given length scales in that the LTz5 electrolytes are rather close to binary electrolytes than LTz10 or LTz15 electrolytes. This result is in good agreement with Section 4.3.1. Density of the Electrolytes, which suggests the similar density profile of LTz5 to LTz0.

On the other hand, the results for LFz electrolytes show drastic increments of the cluster sizes, and even the net charges are increased for some conditions. This ion clustering suggests how zwitterions affect Li^+ ion transport. The reduced negative charge indicates some fractions of anions are escaped from the ion clusters, whereas the raised negative charge indicates ions are aggregated in the electrolytes. Consequently, it can be deduced that zwitterions can help Li^+ ions dissociate TFSI anions, but not FSI anions. Instead, the zwitterions seem to inhibit the dissociation.

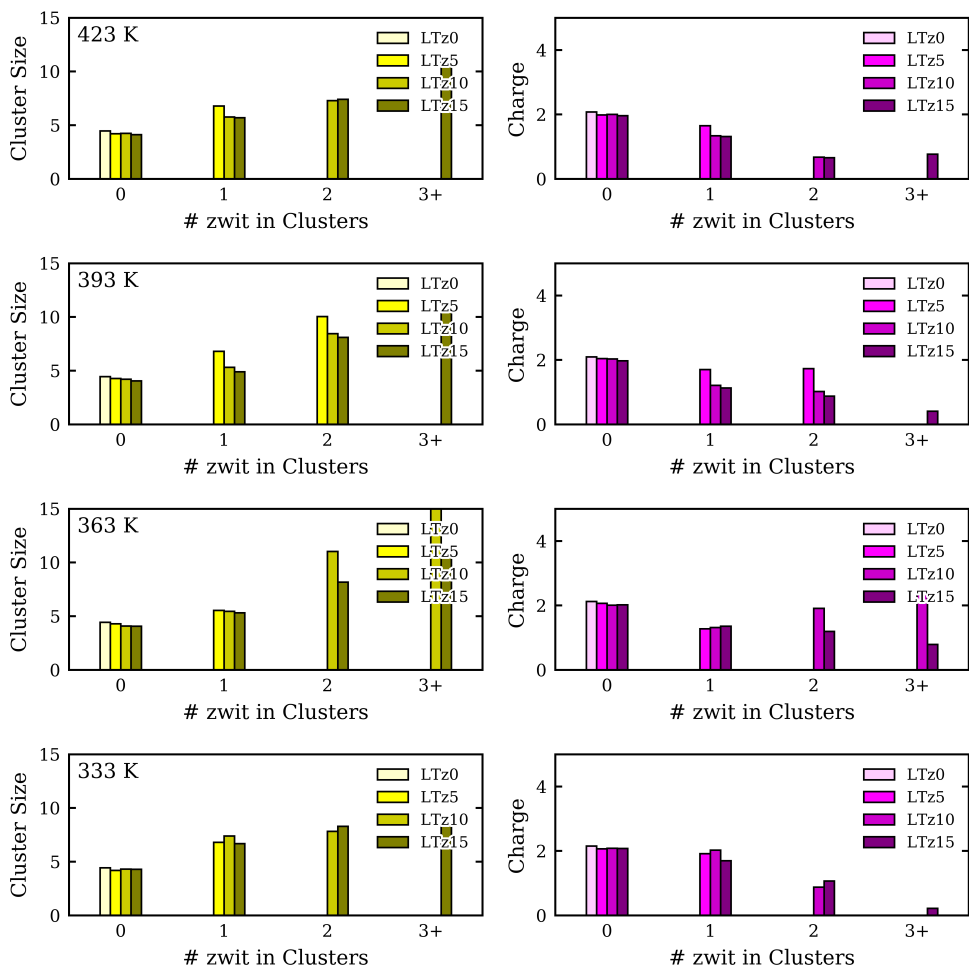


Figure 4-18. Average size and net charge of $[\text{Li}_x\text{TFSI}_n]^{-(n-x)}$ clusters as the function of the number of zwitterions in LTz electrolytes.

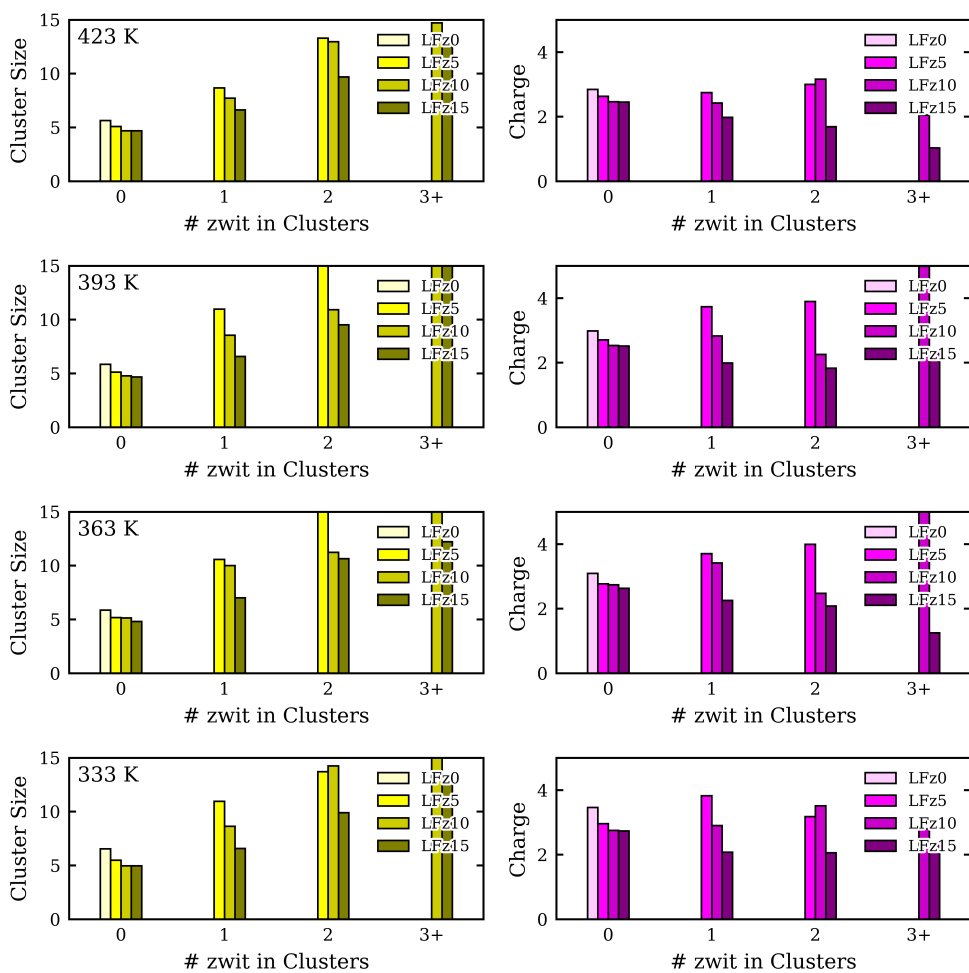


Figure 4-19. Average size and net charge of $[\text{Li}_x\text{FSI}_n]^{-(n-x)}$ clusters as the function of the number of zwitterions in LFz electrolytes.

4.4. Transport Mechanism

In order to elucidate the transport mechanism of Li^+ ions in complex systems, dynamical analysis for ion correlations should be accompanied as well as structural analysis. With zwitterionic additives, dynamical behaviors of Li^+ ions in both LTz and LFz electrolytes are varied. In this section, Li^+ ion correlations with anions and zwitterions are investigated by time-correlation functions of each coordination as conducted in Chapter 3, and various dynamic properties (translational, electrical, and rotational) are predicted from the results of polarizable molecular dynamics simulations. A comprehensive interpretation of the influence of zwitterions on the dynamical behaviors is suggested, and finally, the optimal conditions as electrolytes are evaluated.

4.4.1. Ion Coordination and Transport Mechanism

Details for the coordination time are in Section 3.4.1. Residual Time of Li^+ ions. (Equation (9) and (10)).

As mentioned previously, Li^+ ions can coordinate with negatively charged oxygens of $-\text{SO}_2$ groups in anions or zwitterions. Figure 4-20 shows the autocorrelation functions (ACF) plots of neighbor functions between Li^+ ions and anions or zwitterions in LTz and LFz electrolytes at 423 K. The functions decay as stretched exponential functions for the coordination with the two molecules, and the magnitudes for zwitterions are greater than those of anions. This indicates Li^+ ions are more tightly bound to zwitterions than anions, which is consistent with the results of RDFs in Section 4.3.2. Pair Distribution Functions. The ACFs for Li^+ -anions decay faster in LFz electrolytes than those in LTz electrolytes, while the situation is opposite for Li^+ -zwitterions. The two electrolytes show different manners for a

fraction of zwitterions. With zwitterions, the correlation functions for Li^+ -zwitterions converge to zero for a longer time as more zwitterions are replaced with ionic liquids in both electrolytes. However, LTz0 electrolytes show the slowest relaxation for the Li^+ -anion coordination, whereas LFz0 electrolytes show the fastest relaxation.

In order to compare the data more clearly, quantification was performed by integration of the fitted functions to calculate the lifetime, and weight average of the lifetime for each coordination:

$$\tau = \int_0^{\infty} A \exp\left(-\frac{t}{\tau_{\text{KWW}}}\right)^{\beta} dt \quad (14)$$

$$\tau_{\text{avg}} = \omega_{\text{Anion}} \tau_{\text{Anion}} + \omega_{\text{ZI}} \tau_{\text{ZI}} \quad (15)$$

. The predicted lifetimes for 423 K and 393 K^⑬ are given in Table 4-2. For LTz5 electrolytes, both lifetimes for anions and average are smaller than those of LTz0, and the average lifetimes are optimal points in terms of the fraction of zwitterions. In contrast, the lifetimes of LFz electrolytes are increased with the fraction of zwitterions. These results show consistency with the results from cluster analysis. According to Section 4.3.3. Net charge of ion clusters, the net negative charge of ion clusters is reduced in LTz electrolytes with the increment of zwitterions in individual clusters. This can be attributed to the reduced τ_{Anion} due to zwitterions, and also causes the establishment of optimal condition at LTz5 electrolytes. In contrast, the amount of negative charge is maintained or increased in LFz electrolytes. This indicates ions aggregate around zwitterions and increased τ_{Anion} prove it. Consequently, it is summarized that the zwitterions contribute in a different way depending on anions, even though their chemical compositions and force parameters

^⑬ Due to lack of statistics, the lifetimes for 363 K and 333 K cannot be obtained correctly in the simulation time.

are similar. A more detailed discussion of the dynamic properties is followed in the next section.

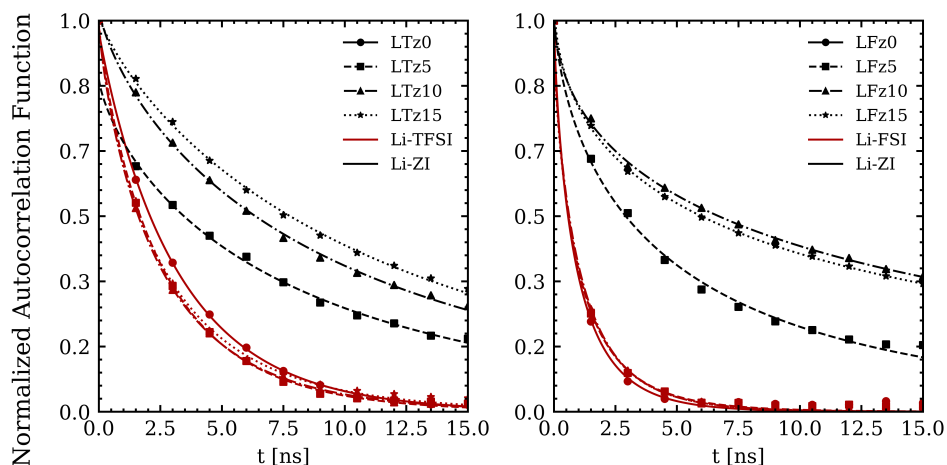


Figure 4-20. Normalized autocorrelation function of neighbor function at 423 K of Li-TFSI (red lines) and Li-Zwitterions (black lines) for LTz and LFz electrolytes; Left: LTz electrolytes, Right: LFz electrolytes.

Table 4-2. Average and individual lifetimes [nanoseconds] of coordination with anions and zwitterions in LTz and LFz electrolytes.

$\tau_{\text{avg}} (\tau_{\text{Anion}}, \tau_{\text{ZI}})$	X = TFSI		X = FSI	
	423 K	393 K	423 K	393 K
LXz0	3.20	5.85	1.09	2.02
LXz5	3.07 (2.79, 8.32)	5.71 (5.05, 18.2)	1.51 (1.21, 7.28)	2.78 (2.20, 13.8)
LXz10	3.71 (2.79, 12.0)	6.70 (4.94, 22.5)	3.54 (1.21, 24.5)	5.41 (2.32, 33.2)
LXz15	4.55 (2.97, 13.5)	12.2 (4.90, 53.7)	4.67 (1.19, 24.4)	13.9 (2.25, 79.8)

4.4.2. Diffusion Coefficient and Conductivity

Details for the calculation of diffusion coefficients are in Section 3.3.1. Diffusion Coefficient. (Equation (5)).

Self-diffusion coefficients as a function of temperatures for Li^+ , PYR_{14} , anions (TFSI or FSI), and zwitterions are plotted in Figure 4-21. For LTz electrolytes, the order of diffusion coefficients for each component is following: $D_{\text{PYR}} \geq D_{\text{TFSI}} > D_{\text{Li}^+} > D_{\text{ZI}}$. On the other hand, anions are the fastest component in LFz electrolytes: $D_{\text{FSI}} > D_{\text{PYR}} > D_{\text{Li}^+} > D_{\text{ZI}}$, due to the lower molar mass of anions. In this regard, D_{Li^+} in ionic liquids with FSI anions are greater than those with TFSI anions as the Li^+ ions can coordinate with lighter anions [58]. Since translational dynamics of zwitterions are significantly slower than other molecules in both electrolytes, it is suggested that the dynamics of Li^+ ions bound to the zwitterions would be slower than other Li^+ ions. With the increment of the fraction of zwitterions, the smaller diffusion coefficients are observed for Li^+ . Cations and anions also seem to be influenced, but the degrees are marginal.

In order to demonstrate the dynamical behavior of liquids or super-cooled liquids, temperature dependence is commonly examined [59,60]. Two representative relationships are well-known to express temperature dependence of diffusion coefficients: Arrhenius relationship and Vogel-Fulcher-Tammann (VFT) relationship, and the equations are following:

$$D = D_0 \exp\left(-\frac{E_a}{RT}\right) \quad (16)$$

$$D = D_0 \exp\left(\frac{V}{T - T_0}\right) \quad (17)$$

, where D_0 , E_a , V , and T_0 are material-dependent parameters. E_a indicates activation energy needed for the diffusion of materials, and T_0 is known as correlated with the glass transition temperatures of the material. In general, when ionic transport is governed by intermolecular ion hopping, the temperature dependence follows Arrhenius law, and if solvent mobility affects the ion transport, the temperature dependence follows a super-Arrhenius behavior, VFT relationship [61]. The dynamics of Li^+ ions and ionic liquids are known to be fitted to the VFT relationship. However, the Arrhenius law is sometimes applied to obtain physical information from activation energy [62,63].

It is noted that the shapes of $\log D_{\text{Li}^+}$ vs. $1/T$ graphs are more linear for the electrolytes with zwitterions than pure binary electrolytes for both LTz and LFz electrolytes, which indicates the contribution of ionic hopping (i.e., structural diffusion mechanism) to Li^+ ion dynamics is increased by the presence of zwitterions in the electrolytes. There are two possible scenarios: (i) More frequent anion exchange; or (ii) Suppression of vehicular diffusion. The former is favorable for Li^+ ion transportation, and the latter inhibits Li^+ dynamics. It was figured out that both two situations corresponded for LTz electrolytes from the fact of decreased τ_{Anion} for LTz5 electrolytes and slow dynamics of zwitterions binding Li^+ ions for an extended time. Thus, despite the slower dynamics at the high temperatures for LTz electrolytes with zwitterions than pure binary electrolytes, the predicted diffusion coefficient of LTz5 electrolyte at 333 K is greater than LTz0 electrolyte, and enhanced dynamics at lower temperatures are expected by extrapolation. On the other hand, zwitterions in LFz electrolytes leading to the ion aggregation cause fewer anion exchanges, and it is confirmed by time-correlation functions in Section 4.4.1.

Ion Coordination and Transport Mechanism As a result, Li^+ dynamics are gradually

decreased by the fraction of zwitterions.

The impact of zwitterions on the temperature dependence could be quantified through the activation energies of Li^+ ions in Arrhenius law. Figure 4-22 shows the fitted activation energies for diffusion coefficients of Li^+ ions in the explored temperature range. As expected, the activation energies of Li^+ ions of LTz electrolytes have a minimum at LTz5, and the values are increased with the fraction of zwitterions. LFz electrolytes also showed decreased activation energies. This is due to the suppression of vehicular motion as described above, and exceptionally decreased activation energy for LTz15 electrolytes is attributed to extraordinarily large ion clusters, which can cause the motion of Li^+ to be glassy.

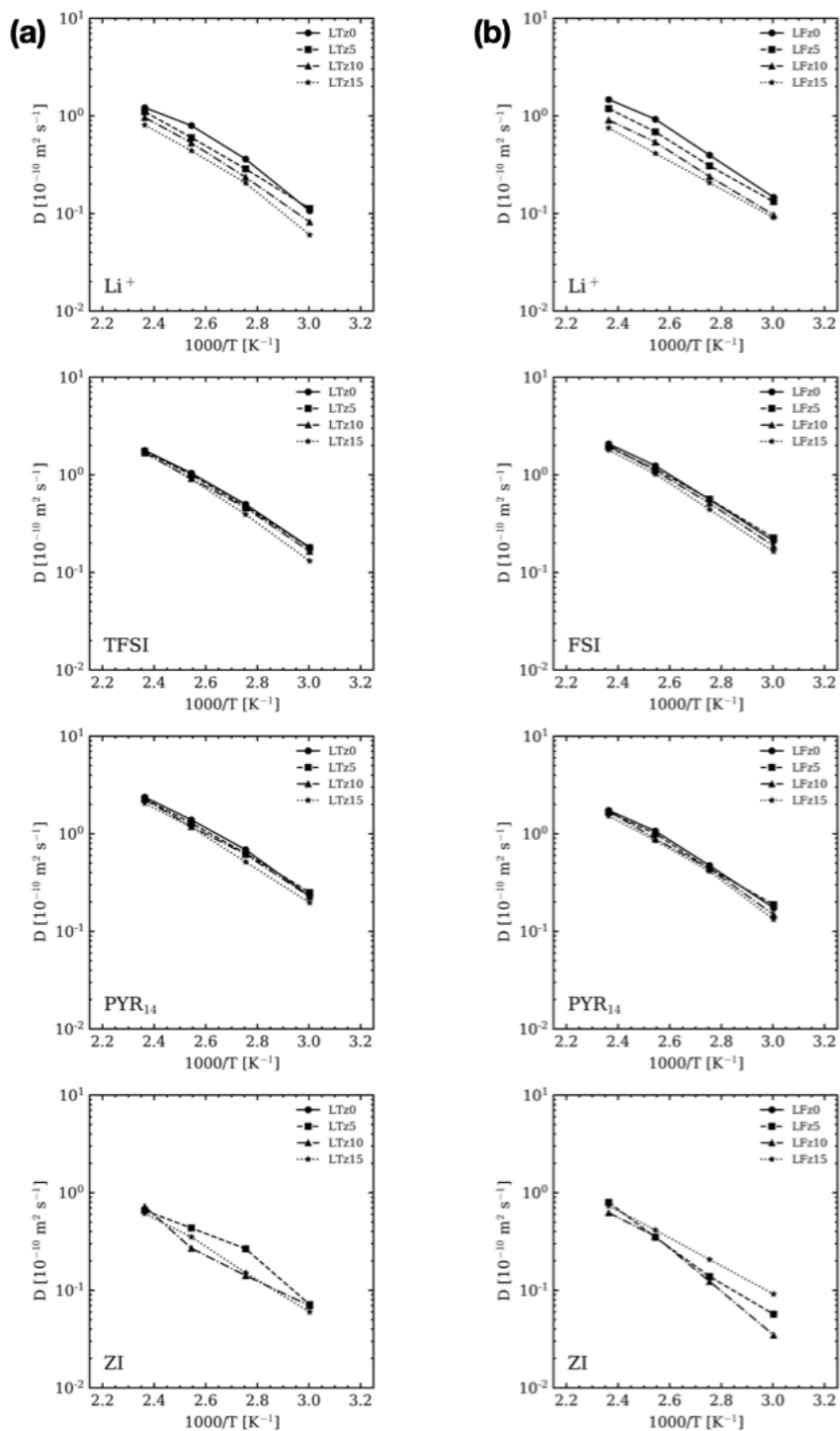


Figure 4-21. Diffusion coefficients as a function of temperatures for each component. Left: LTz, and Right: LFz.

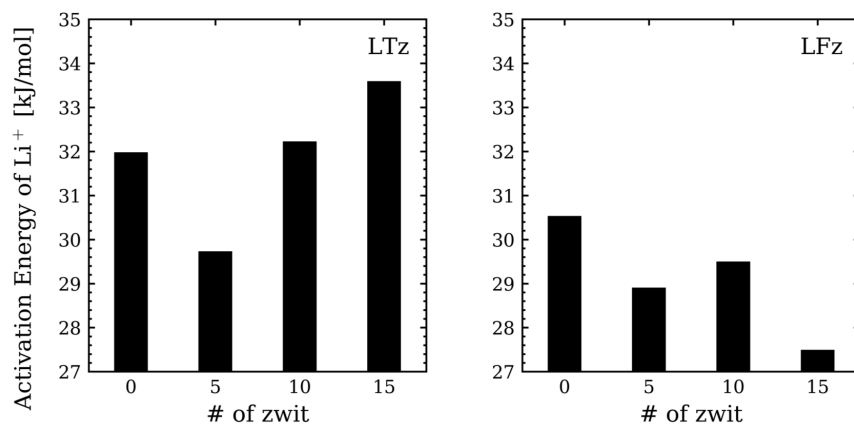


Figure 4-22. Activation energies for diffusions of Li⁺ ions. Left: LTz, and Right: LFz.

The electrical conductivities of LTz and LFz electrolytes are calculated by the same procedure with Section 3.3.2. Ionic Conductivity and plotted in Figure 4-23 and Figure 4-24, respectively. In addition, the degrees of ion dissociation for the electrolytes are shown in Table 4-3 and Table 4-4. Since α for the electrolytes are in the range of 0.6–0.9, it can be considered that the magnitude is large enough to apply Equation (7) and (8). The magnitudes in LFz electrolytes are greater than LTz electrolytes. However, the LFz electrolytes seem to be more sensitive to the presence of zwitterions than LTz electrolytes. The temperature dependence of conductivities of electrolytes and Li^+ are not too deviated from the previous as they are relevant to diffusion coefficients.

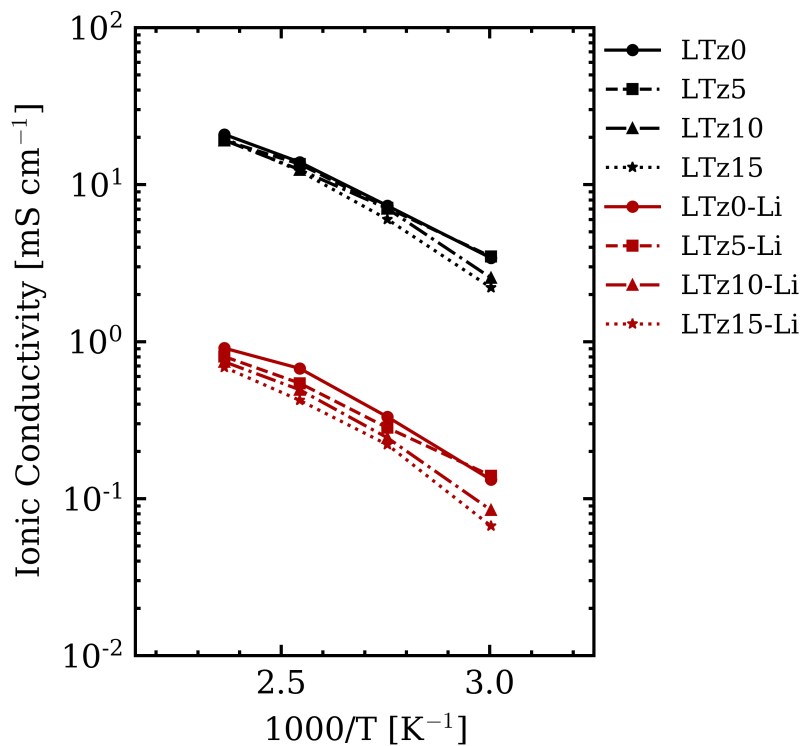


Figure 4-23. Ionic conductivities of electrolytes and Li ions for LTz electrolytes

Table 4-3. The degree of ion dissociation for LTz electrolytes

	423 K	393 K	363 K	333 K
LTz0	0.60	0.62	0.61	0.74
LTz5	0.58	0.66	0.65	0.74
LTz10	0.61	0.67	0.68	0.61
LTz15	0.67	0.69	0.70	0.65

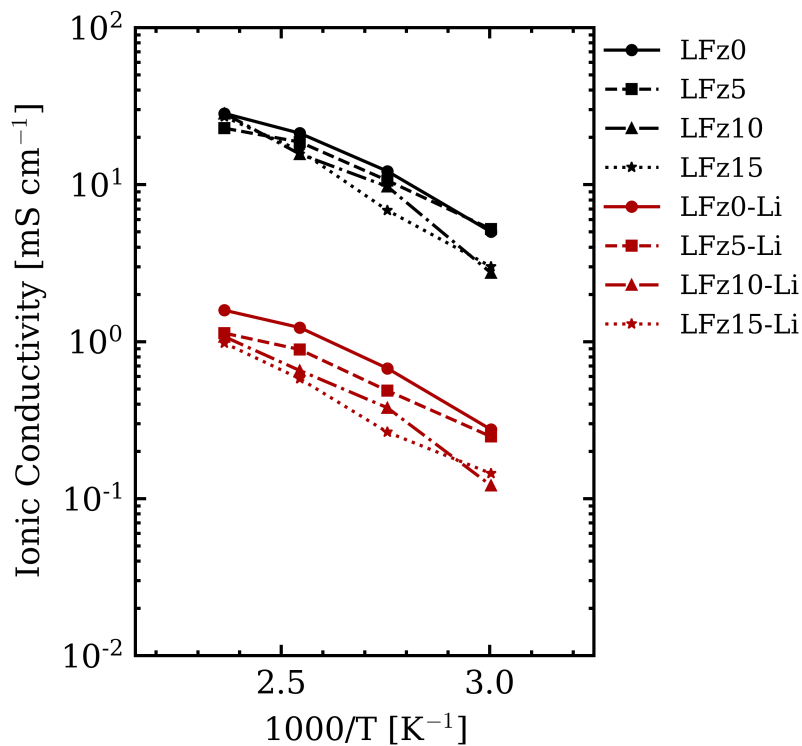


Figure 4-24. Ionic conductivities of electrolytes and Li ions for LFz electrolytes

Table 4-4. The degree of ion dissociation for LFz electrolytes

	423 K	393 K	363 K	333 K
LFz0	0.69	0.78	0.91	0.90
LFz5	0.61	0.76	0.84	0.90
LFz10	0.76	0.71	0.84	0.60
LFz15	0.83	0.82	0.68	0.76

4.4.3. Rotational Relaxation

The advantage of the zwitterion is not limited to the electrical properties. Trachenko proposed a theory that VFT relationship can be explained via elastic interaction between local relaxation events (LRE), and he suggested that the fragility of materials is relevant to LREs [64]. According to the theory, local relaxation events mean elementary local structural rearrangements. Since the zwitterions have functional groups with the opposite charge at each end of the molecules, they have a high molecular dipole moment though they are neutral. With a relatively large hydrodynamic radius and a high dipole moment, the zwitterions are expected to have difficult to reorient compared to the ionic liquids. This can be confirmed by rotational relaxation of each component obtained from fitting the second-order Legendre polynomial ($P_2(t) = \langle \frac{3\cos^2(\theta)-1}{2} \rangle$) for the reorientation of representative vectors of the molecules (Figure 4-25) to stretched exponential function (Equation (14)). The fits of rotational dynamics for LTz and LFz electrolytes are plotted in Figure 4-26 and Figure 4-27, and the numerical parameters are listed in Table 4-5 and Table 4-6. The rotational relaxation is in order of $P_2^{ZI}(t) > P_2^{TFSI}(t) > P_2^{PYR}(t)$ in LTz electrolytes, and $P_2^{ZI}(t) > P_2^{FSI}(t) \approx P_2^{PYR}(t)$ in LFz electrolytes. $P_2(t)$ for both electrolytes decay slower as the temperature decrease. From the integration of the fitted functions, rotational relaxation time τ_C could be obtained. As expected, τ_C for zwitterions are extraordinarily greater than other components, which indicates liquid elasticity lengths are also extended according to Trachenko's study. For the same temperatures, extended liquid elasticity lengths enable the materials to be strong [65]. Thus, the enhanced mechanical properties are predicted by zwitterions, which could be advantageous in suppressing Li^+ dendrite charge/discharge processes. This is

remarkable that the LTz5 electrolytes are advantageous in both transport and mechanical aspects.

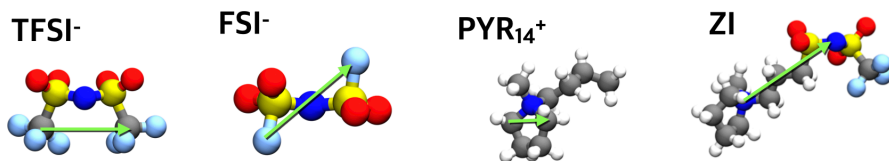


Figure 4-25. Representative vectors of TFSI, FSI, PYR₁₄, and zwitterion to calculate the second order Legendre polynomials

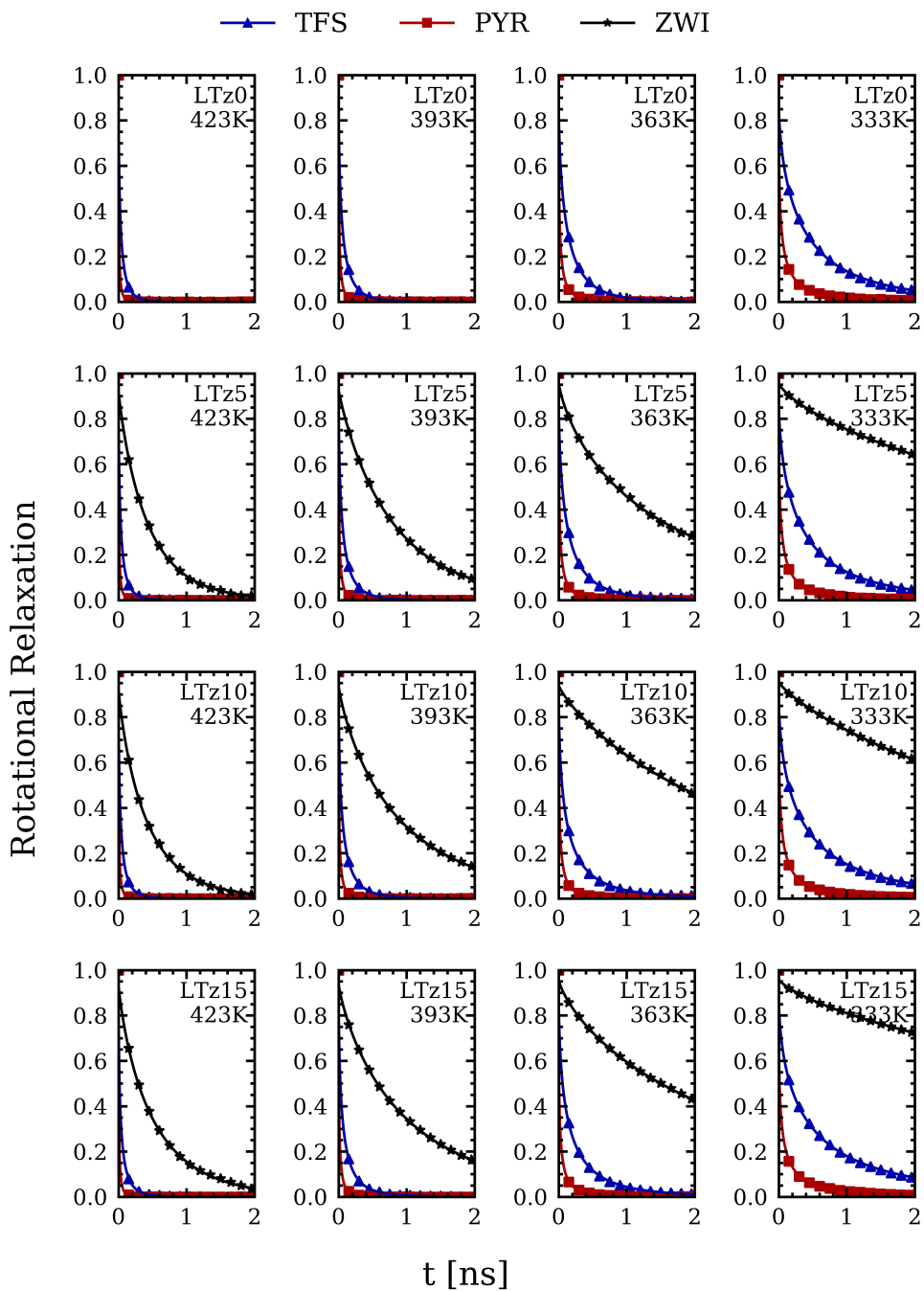


Figure 4-26. Second order Legendre polynomial of each component in LTz electrolytes as temperatures and the fraction of zwitterions.

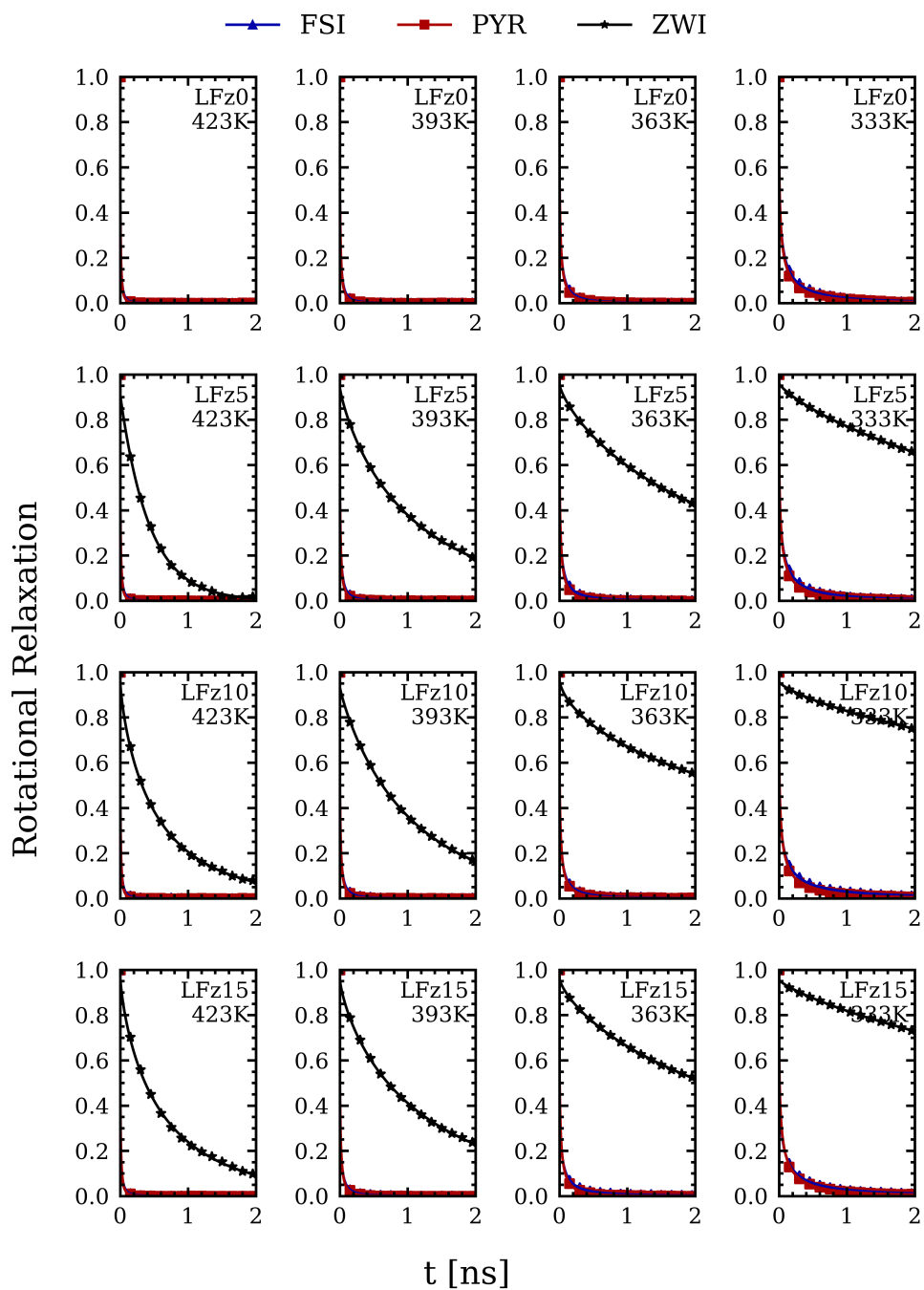


Figure 4-27. Second order Legendre polynomial of each component in LFz electrolytes as temperatures and the fraction of zwitterions.

Table 4-5. Fitted lifetime [nanoseconds] and exponent parameters (in parentheses) to stretched exponential functions for the second order Legendre polynomials of each component in LTz electrolytes for varied temperatures.

		423 K	393 K	363 K	333 K
LTz0	Cation	0.011 (0.49)	0.018 (0.48)	0.035 (0.44)	0.098 (0.40)
	Anion	0.042 (0.61)	0.072 (0.61)	0.149 (0.64)	0.462 (0.62)
	Zwitterion	-	-	-	-
LTz5	Cation	0.011 (0.49)	0.018 (0.47)	0.037 (0.44)	0.090 (0.41)
	Anion	0.043 (0.60)	0.076 (0.60)	0.164 (0.61)	0.432 (0.61)
	Zwitterion	0.414 (0.90)	0.768 (0.92)	1.694 (0.75)	7.769 (0.74)
LTz10	Cation	0.011 (0.49)	0.019 (0.46)	0.037 (0.44)	0.102 (0.40)
	Anion	0.046 (0.59)	0.084 (0.59)	0.186 (0.54)	0.526 (0.57)
	Zwitterion	0.414 (0.87)	0.937 (0.83)	3.078 (0.84)	5.555 (0.83)
LTz15	Cation	0.012 (0.48)	0.020 (0.46)	0.042 (0.42)	0.120 (0.38)
	Anion	0.048 (0.57)	0.087 (0.57)	0.210 (0.56)	0.641 (0.55)
	Zwitterion	0.512 (0.85)	1.037 (0.82)	2.940 (0.77)	12.648 (0.74)

Table 4-6. Fitted lifetime [nanoseconds] and exponent parameters (in parentheses) to stretched exponential functions for the second order Legendre polynomials of each component in LFz electrolytes for varied temperatures.

		423 K	393 K	363 K	333 K
LFz0	Cation	0.010 (0.49)	0.015 (0.46)	0.031 (0.42)	0.089 (0.37)
	Anion	0.010 (0.43)	0.017 (0.41)	0.036 (0.38)	0.110 (0.36)
	Zwitterion	-	-	-	-
LFz5	Cation	0.010 (0.48)	0.016 (0.46)	0.032 (0.42)	0.076 (0.38)
	Anion	0.011 (0.42)	0.019 (0.39)	0.041 (0.36)	0.102 (0.35)
	Zwitterion	0.395 (0.99)	1.172 (0.82)	2.916 (0.77)	7.356 (0.79)
LFz10	Cation	0.010 (0.48)	0.017 (0.45)	0.035 (0.40)	0.093 (0.36)
	Anion	0.011 (0.40)	0.020 (0.38)	0.042 (0.35)	0.139 (0.32)
	Zwitterion	0.642 (0.75)	1.062 (0.88)	6.815 (0.63)	14.495 (0.76)
LFz15	Cation	0.011 (0.47)	0.018 (0.44)	0.036 (0.40)	0.100 (0.36)
	Anion	0.011 (0.40)	0.020 (0.37)	0.049 (0.33)	0.130 (0.32)
	Zwitterion	0.740 (0.74)	1.404 (0.76)	4.503 (0.73)	10.899 (0.80)

4.5. Conclusion

In the present chapter, polarizable molecular dynamics simulations were performed to investigate the Li^+ ion transport mechanism in $\text{LiTFSI}/\text{PYR}_{14}\text{TFSI}$ electrolytes with zwitterions and the impact of the zwitterions, a component composed of the covalent bonded of TFSI and PYR_{14} , and $\text{LiTFSI}/\text{PYR}_{14}\text{FSI}$ for comparison. Once zwitterions were added to the electrolytes, the density values were increased, and LFz electrolytes showed a distinct increment by the fraction of zwitterions compared to LTz electrolytes. Exceptively, LTz5 electrolytes showed a similar density profile to the pure binary electrolytes as the fraction of zwitterions was subtle to change thermodynamic properties. The zwitterions competed with anions in the electrolytes to coordinate with Li^+ ions, and the Li^+ ions tended to more favorably coordinate with zwitterions than anions. The cluster analysis results showed that the zwitterions reduced the net charge of each ion cluster of $[\text{Li}_x\text{TFSI}_n]^{-(n-x)}$ without increasing bulkiness in LTz electrolytes, but they increased the hydrodynamic radius and the net charge of the clusters in LFz electrolytes. This suggested that zwitterions lead to ion aggregation in LFz electrolytes. This idea supported elucidating the dynamical behavior of Li^+ ions in the electrolytes. Correlation times of Li^+ ions between anions τ_{Anion} were decreased in LTz electrolytes by the presence of the zwitterions, whereas they increased in LFz electrolytes. In addition, the weight average lifetimes τ_{avg} were decreased in the LTz5 electrolytes despite the enormous magnitude of τ_{ZI} . This suggested that the required energy for Li^+ ions to escape their coordination shell was decreased, and more structural diffusion would occur in the condition. As a result, the global temperature dependence of Li^+ dynamics was transformed like Arrhenius law, and the activation energy for Li^+ diffusion was dropped down to some

concentration of zwitterions. This was favorable to Li^+ dynamics. When more zwitterions were introduced, however, slow dynamics of the zwitterions suppressed the vehicular motion of Li^+ ions, and this circumstance was more significant in LFz electrolytes in that the ions in the electrolytes aggregated and formed large ion clusters. Increased rotational relaxation time by zwitterions suggested enhanced mechanical properties of the electrolytes. In conclusion, adding a few zwitterions can improve the performance of electrolytes in terms of dynamical and mechanical properties, and the LTz5 showed the optimal conditions of the electrolytes.

Chapter 5. Concluding Remarks

5.1. Summarize of Study

In the present dissertation, molecular dynamics (MD) studies with many-body polarizable force fields based on induced point dipoles were conducted to investigate Li^+ ion transport in the electrolytes for lithium-ion batteries with ionic liquids. The necessity of using polarizable force fields was justified at the beginning of the dissertation by comparison with non-polarizable force fields. With the force fields, modeling and MD simulations for multi-component systems including Li^+ salt, ionic liquids, and polymers in cylindrical confined geometry were performed in Chapter 3, and qualitative analysis on both thermodynamics and kinetics at the atomic scale was conducted intensively. Especially, it was elucidated that change of Li^+ coordination shell and ion cluster population by the presence of branched polymers facilitates more frequent anion exchange leading to structural diffusion of Li^+ ions.

A critical drawback of slow implementation, which limited extensive research on polarizable MD simulations, was overcome by modification OpenMM software package to enable APPLE&P force fields. A new plugin for OpenMM was developed, including the calculation of Buckingham potential and electrostatic potential with induced point dipoles. With the improved implementation, polarizable MD simulations were conducted for the electrolytes with ionic liquids and zwitterion additives. Unique characteristics of the zwitterions from the oppositely charged functional groups at the end of molecules led to positive or negative progress in terms of dynamical and mechanical properties. In compatible solvents, zwitterions helped Li^+ transport in the manner of activating ion dissociation from anions. The reduced net negative charge of Li^+ ion clusters and coordination times with TFSI anions in

LiTFSI/PYR₁₄TFSI electrolytes supported the idea. On the other hand, the zwitterions inhibited Li⁺ transport by ion clustering, and it was proved by increased monodentate phases in LiFSI/PYR₁₄FSI electrolytes and cluster analysis. Nevertheless, the high molecular dipole moment resulted in slow rotational relaxation compared to other components in electrolytes, and the mechanical strengths were reinforced by the zwitterions. Thus, it was possible to obtain the electrolytes with optimal conditions in electrical and mechanical aspects.

In summary, this study suggested how to model and design electrolytes for lithium-ion batteries through a thorough theoretical investigation based on polarizable molecular dynamics simulations. Furthermore, this work contributed to accelerating the implementation of APPLE&P force fields hence following studies can explore more extensive materials than before.

5.2. Limitation and Future Works

Since the objective of OpenMM was not to develop a sophisticated and complete MD software package, there is a lot of limitation to calculation or methodology. One critical example is internal virial calculation. Without the internal virial calculation, pressures could not be obtained, which limits the choice of barostats and calculation of various thermodynamic observations such as stress tensors. In order to complete the analysis for battery systems with polarizable force fields, the limitations should be overcome in future works.

Based on the results of molecular dynamics simulations in this dissertation, machine learning approaches are applied to understand the transport mechanism in terms of the microphase transition of Li⁺ ion clusters. From this investigation, more

specific information could be obtained which cannot be recognized by the perception ability of humans.

Bibliography

1. Osada I, De Vries H, Scrosati B, Passerini S. Ionic-Liquid-Based Polymer Electrolytes for Battery Applications. *Angew Chemie - Int Ed.* 2016;55(2):500-513.
2. Watanabe M, Thomas ML, Zhang S, Ueno K, Yasuda T, Dokko K. Application of Ionic Liquids to Energy Storage and Conversion Materials and Devices. *Chem Rev.* 2017;117(10):7190-7239.
3. Lewandowski A, Świdarska-Mocek A. Ionic liquids as electrolytes for Li-ion batteries-An overview of electrochemical studies. *J Power Sources.* 2009;194(2):601-609.
4. Neyertz S, Brown D. Local structure and mobility of ions in polymer electrolytes: A molecular dynamics simulation study of the amorphous PEOxNaI system. *J Chem Phys.* 1996;104(10):3797-3809.
5. Oldiges K, Diddens D, Ebrahimi M, et al. Understanding transport mechanisms in ionic liquid/carbonate solvent electrolyte blends. *Phys Chem Chem Phys.* 2018;20(24):16579-16591.
6. Allam O, Cho BW, Kim KC, Jang SS. Application of DFT-based machine learning for developing molecular electrode materials in Li-ion batteries. *RSC Adv.* 2018;8(69):39414-39420.
7. Hu L, Zhang SS, Zhang Z. *Electrolytes for Lithium and Lithium-Ion Batteries.* Vol 172.; 2015.
8. Xing L, Vatamanu J, Borodin O, Smith GD, Bedrov D. Electrode/electrolyte interface in sulfolane-based electrolytes for Li ion batteries: A molecular dynamics simulation study. *J Phys Chem C.* 2012;116(45):23871-23881.
9. Kim HI, Shin E, Kim SH, et al. Aqueous eutectic lithium-ion electrolytes for wide-temperature operation. *Energy Storage Mater.* 2021;36(September 2020):222-228.
10. Bates JB, Dudney NJ, Neudecker B, Ueda A, Evans CD. ThinBates, J. B., Dudney, N. J., Neudecker, B., Ueda, A., & Evans, C. D. (2000). Thin-film lithium and lithium-ion batteries. *Solid State Ionics*, 135(1-4), 33–45. doi:10.1016/S0167-2738(00)00327-1-film lithium and lithium-ion batteries. *Solid State Ionics.* 2000;135(1-4):33-45.
11. Monroe C, Newman J. The Impact of Elastic Deformation on Deposition Kinetics at Lithium/Polymer Interfaces. *J Electrochem Soc.* 2005;152(2):A396.
12. Howlett PC, MacFarlane DR, Hollenkamp AF. High lithium metal cycling efficiency in a room-temperature ionic liquid. *Electrochem Solid-State Lett.* 2004;7(5).
13. Galiński M, Lewandowski A, Stepniak I. Ionic liquids as electrolytes. *Electrochim Acta.* 2006;51(26):5567-5580.

14. Welton T. Ionic liquids: a brief history. *Biophys Rev.* 2018;10(3):691-706.
15. Long L, Wang S, Xiao M, Meng Y. Polymer electrolytes for lithium polymer batteries. *J Mater Chem A.* 2016;4(26):10038-10039.
16. Kim J Il, Choi YG, Ahn Y, Kim D, Park JH. Optimized ion-conductive pathway in UV-cured solid polymer electrolytes for all-solid lithium/sodium ion batteries. *J Memb Sci.* 2021;619(August 2020):118771.
17. Joost M, Kunze M, Jeong S, Schönhoff M, Winter M, Passerini S. Ionic mobility in ternary polymer electrolytes for lithium-ion batteries. *Electrochim Acta.* 2012;86:330-338.
18. Wan Z, Lei D, Yang W, et al. Low Resistance–Integrated All-Solid-State Battery Achieved by Li₇La₃Zr₂O₁₂ Nanowire Upgrading Polyethylene Oxide (PEO) Composite Electrolyte and PEO Cathode Binder. *Adv Funct Mater.* 2019;29(1):1-10.
19. Li S, Zhang SQ, Shen L, et al. Progress and Perspective of Ceramic/Polymer Composite Solid Electrolytes for Lithium Batteries. *Adv Sci.* 2020;7(5).
20. Chopade SA, Au JG, Li Z, Schmidt PW, Hillmyer MA, Lodge TP. Robust Polymer Electrolyte Membranes with High Ambient-Temperature Lithium-Ion Conductivity via Polymerization-Induced Microphase Separation. *ACS Appl Mater Interfaces.* 2017;9(17):14561-14565.
21. Ihrner N, Johannisson W, Sieland F, Zenkert D, Johansson M. Structural lithium ion battery electrolytes: Via reaction induced phase-separation. *J Mater Chem A.* 2017;5(48):25652-25659.
22. Mong Anh L, Kim D. Solid Electrolyte Membrane Prepared from Poly(arylene ether sulfone)- g- Poly(ethylene glycol) for Lithium Secondary Battery. *ACS Appl Energy Mater.* 2019;2(4):2585-2595.
23. Fedeli E, Kvasha A, Gignes D, Phan TNT. Synthesis and use of zwitterion bearing sulfonyl(Trifluoromethane sylfonyl)imide anion as additive for polymer electrolytes. *Appl Sci.* 2020;10(21):1-12.
24. Wohde F, Bhandary R, Moldrickx JM, Sundermeyer J, Schönhoff M, Roling B. Li⁺ ion transport in ionic liquid-based electrolytes and the influence of sulfonate-based zwitterion additives. *Solid State Ionics.* 2016;284:37-44.
25. Son CY, Wang ZG. Ion transport in small-molecule and polymer electrolytes. *J Chem Phys.* 2020;153(10):100903.
26. Costa LT, Sun B, Jeschull F, Brandell D. Polymer-ionic liquid ternary systems for Li-battery electrolytes: Molecular dynamics studies of LiTFSI in a EMIm-TFSI and PEO blend. *J Chem Phys.* 2015;143(2).
27. Chaban V. Polarizability versus mobility: Atomistic force field for ionic liquids. *Phys Chem Chem Phys.* 2011;13(35):16055-16062.
28. Casalegno M, Castiglione F, Raos G, et al. Magnetic Resonance Imaging and Molecular Dynamics Characterization of Ionic Liquid in Poly(ethylene oxide)-Based Polymer Electrolytes. *ACS Appl Mater Interfaces.*

- 2020;12(21):23800-23811.
29. Canongia Lopes JN, Deschamps J, Pádua AAH. Modeling Ionic Liquids Using a Systematic All-Atom Force Field. *J Phys Chem B*. 2004;108(6):2038-2047.
 30. Borodin O. Polarizable force field development and molecular dynamics simulations of ionic liquids. *J Phys Chem B*. 2009;113(33):11463-11478.
 31. Borodin O, Smith GD. LiTFSI structure and transport in ethylene carbonate from molecular dynamics simulations. *J Phys Chem B*. 2006;110(10):4971-4977.
 32. Li Z, Smith GD, Bedrov D. Li⁺ solvation and transport properties in ionic liquid/lithium salt mixtures: A molecular dynamics simulation study. *J Phys Chem B*. 2012;116(42):12801-12809.
 33. Maitra A, Heuer A. Cation transport in polymer electrolytes: A microscopic approach. *Phys Rev Lett*. 2007;98(22):1-4.
 34. Diddens D, Heuer A. Simulation study of the lithium ion transport mechanism in ternary polymer electrolytes: The critical role of the segmental mobility. *J Phys Chem B*. 2014;118(4):1113-1125.
 35. Diddens D, Paillard E, Heuer A. Improving the Lithium Ion Transport in Polymer Electrolytes by Functionalized Ionic-Liquid Additives: Simulations and Modeling. *J Electrochem Soc*. 2017;164(11):E3225-E3231.
 36. Chenouard N, Smal I, De Chaumont F, et al. Objective comparison of particle tracking methods. *Nat Methods*. 2014;11(3):281-289.
 37. Kim S, Lee M, Park C, et al. Molecular dynamics study on lithium-ion transport in PEO branched nanopores with PYR 14 TFSI ionic liquid. *Batter Energy*. 2022;1(2):20210013.
 38. Bedrov D, Piquemal JP, Borodin O, MacKerell AD, Roux B, Schröder C. Molecular Dynamics Simulations of Ionic Liquids and Electrolytes Using Polarizable Force Fields. *Chem Rev*. 2019;119(13):7940-7995.
 39. Schröder C. Comparing reduced partial charge models with polarizable simulations of ionic liquids. *Phys Chem Chem Phys*. 2012;14(9):3089-3102.
 40. Momany FA. Determination of partial atomic charges from ab initio molecular electrostatic potentials. Application to formamide, methanol, and formic acid. *J Phys Chem*. 1978;82(5):592-601.
 41. Applequist J, Carl JR, Fung KK. An Atom Dipole Interaction Model for Molecular Polarizability. Application to Polyatomic Molecules and Determination of Atom Polarizabilities. *J Am Chem Soc*. 1972;94(9):2952-2960.
 42. Thole BT. Molecular polarizabilities calculated with a modified dipole interaction. *Chem Phys*. 1981;59(3):341-350.
 43. Borodin O, Smith GD, Bandyopadhyaya R, Bytner O. Molecular dynamics study of the influence of solid interfaces on poly(ethylene oxide) structure and dynamics. *Macromolecules*. 2003;36(20):7873-7883.
 44. Borodin O, Smith GD. Molecular dynamics simulations of comb-branched

- poly(epoxide ether)-based polymer electrolytes. *Macromolecules*. 2007;40(4):1252-1258.
45. Starovoytov ON, Borodin O, Bedrov D, Smith GD. Development of a polarizable force field for molecular dynamics simulations of poly (Ethylene Oxide) in aqueous solution. *J Chem Theory Comput*. 2011;7(6):1902-1915.
 46. Shi Y, Xia Z, Zhang J, et al. Polarizable atomic multipole-based AMOEBA force field for proteins. *J Chem Theory Comput*. 2013;9(9):4046-4063.
 47. Lamoureux G, Roux B. Modeling induced polarization with classical Drude oscillators: Theory and molecular dynamics simulation algorithm. *J Chem Phys*. 2003;119(6):3025-3039.
 48. Striolo A, Chialvo AA, Cummings PT, Gubbins KE. Simulated water adsorption in chemically heterogeneous carbon nanotubes. *J Chem Phys*. 2006;124(7).
 49. Tong J, Wu S, von Solms N, et al. The Effect of Concentration of Lithium Salt on the Structural and Transport Properties of Ionic Liquid-Based Electrolytes. *Front Chem*. 2020;7(February):1-10.
 50. Haskins JB, Bennett WR, Wu JJ, et al. Computational and experimental investigation of li-doped ionic liquid electrolytes: [pyr14][TFSI], [pyr13][FSI], and [EMIM][BF4]. *J Phys Chem B*. 2014;118(38):11295-11309.
 51. Eduardo J, Ugarte M. Étude operando des accumulateurs au lithium par couplage de spectroscopie à photoémission des rayons X et spectroscopie d'impédance In operando study of lithium batteries by coupling X-ray photoelectron spectroscopy and impedance spectroscopy JORGE EDUA. Published online 2016.
 52. Hagberg AA, Schult DA, Swart PJ. Exploring network structure, dynamics, and function using NetworkX. *7th Python Sci Conf (SciPy 2008)*. 2008;(SciPy):11-15.
 53. Chapman N, Borodin O, Yoon T, Nguyen CC, Lucht BL. Spectroscopic and Density Functional Theory Characterization of Common Lithium Salt Solvates in Carbonate Electrolytes for Lithium Batteries. *J Phys Chem C*. 2017;121(4):2135-2148.
 54. Beltrop K, Meister P, Klein S, et al. Does Size really Matter? New Insights into the Intercalation Behavior of Anions into a Graphite-Based Positive Electrode for Dual-Ion Batteries. *Electrochim Acta*. 2016;209:44-55.
 55. Frisch MJ, Trucks GW, Schlegel HB, et al. G16_C01. Published online 2016:Gaussian 16, Revision C.01, Gaussian, Inc., Wallin.
 56. Antila H. Electrostatics of a polarizable force field based on the Thole point dipole model. Published online 2011.
 57. Eastman P, Swails J, Chodera JD, et al. OpenMM 7: Rapid development of high performance algorithms for molecular dynamics. *PLOS Comput Biol*. 2017;13(7):1-17.

58. Solano CJF, Jeremias S, Paillard E, Beljonne D, Lazzaroni R. A joint theoretical/experimental study of the structure, dynamics, and Li⁺ transport in bis([tri]fluoro[methane]sulfonyl)imide [T]FSI-based ionic liquids. *J Chem Phys.* 2013;139(3).
59. Shah JK, Marin-Rimoldi E, Mullen RG, et al. Cassandra: An open source Monte Carlo package for molecular simulation. *J Comput Chem.* 2017;38(19):1727-1739.
60. Smith GD, Borodin O, Magda JJ, et al. A comparison of fluoroalkyl-derivatized imidazolium: TFSI and alkyl-derivatized imidazolium: TFSI ionic liquids: A molecular dynamics simulation study. *Phys Chem Chem Phys.* 2010;12(26):7064-7076.
61. Kim H, Koo B, Lee H. Comparison of Arrhenius and VTF Description of Ion Transport Mechanism in the Electrolytes. *J Korean Electrochem So.* 2020;23(4):81-89.
62. Castiglione F, Famulari A, Raos G, et al. Pyrrolidinium-based ionic liquids doped with lithium salts: How does Li⁺ coordination affect its diffusivity? *J Phys Chem B.* 2014;118(47):13679-13688.
63. Castiglione F, Ragg E, Mele A, Appetecchi GB, Montanino M, Passerini S. Molecular environment and enhanced diffusivity of Li⁺ ions in lithium-salt-doped ionic liquid electrolytes. *J Phys Chem Lett.* 2011;2(3):153-157.
64. Trachenko K. The Vogel-Fulcher-Tammann law in the elastic theory of glass transition. *J Non Cryst Solids.* 2008;354(32):3903-3906.
65. Angell CA. Formation of glasses from liquids and biopolymers. *Science (80-).* 1995;267(5206):1924-1935.

요약 (국문초록)

리튬 이온 전지와 관련된 연구에 대한 수요가 증가함에 따라, 좋은 성능을 가지는 리튬 이온 전지를 개발하기 위한 광범위하고 폭넓은 연구들이 진행되어왔다. 여기서 말하는 좋은 성능의 기준이란 전기적인 기능성 뿐만 아니라 안정성의 측면을 아우른다. 전지의 핵심 구성 물질 중 하나인 전해질은 이러한 성능에 매우 큰 영향을 미친다. 액체 전해질의 경우 높은 전기전도도를 가지지만 그와 동시에 화학적으로, 또 기계적으로 불안정한 성질을 가진다. 반면에, 고체 전해질을 사용하면 수화 반응이나 누액 등, 안정성에 관한 우려는 할 필요가 없지만 상대적으로 낮은 전기전도도를 띤다. 이러한 맥락에서 볼 때, 리튬 이온 전지를 위한 우수한 전해질을 개발하기 위해서는 구조적, 동역학적 성질에 대한 깊은 이해가 수반되어야 한다.

편극성 분자동역학 시뮬레이션은 리튬 이온 전지에 쓰이는 전해질의 거동을 정확하게 묘사하는 것으로 알려져있다. 특히, 유도 쌍극자 모델을 기반으로 한 APPLE&P 라는 역장은 다른 어떤 모델보다도 이온성 액체나 고분자 전해질 내에서의 리튬 이온의 동역학을 잘 예측한다. 비록 편극성 분자동역학 시뮬레이션을 실행하는데 소요되는 시간이 상당하다 할지라도, 다른 모델들이 예측하는 부정확한 결과들을 고려하였을 때 이 모델을 사용했을 때 얻는 가치는 상당하다.

본 학위논문에서는, APPLE&P 역장을 필두로 한 다체 편극성 분자동역학 시뮬레이션을 이용하여 이온성 액체 기반 전해질에서의 리튬

이온의 수송 메커니즘을 분석하였다. Poly-(ethylene oxide) (PEO) 고분자 사슬이 달려있고 [1-butyl-1-methylpyrrolidinium][bis(trifluoromethanesulfonyl)imide] (PYR₁₄TFSI) 형태의 이온성 액체가 채워진 이온 채널 기반 전해질과, PYR₁₄ 양이온 및 TFSI 음이온의 공유결합으로 이루어진 양쪽성이온을 (zwitterions) 포함한 이온성 액체 형태의 전해질, 총 두 가지 전해질을 사례로 들어 이에 대한 이온 수송 메커니즘을 규명하였으며, 이를 위해 전해질 내 구조적, 동역학적 물성이 연구되었다. 원자쌍 결합거리 분포 및 이온 군집 분석을 이용한 세밀한 분석을 통해 리튬 이온이 전해질 내에서 가지는 배위 결합 구조를 밝혀내었다. 전해질 내에 도입된 제 3의 물질이 구조적인 물성에 변화를 주었고 이는 곧 리튬 이온의 이동에 영향을 주었다. 이온 채널을 가진 전해질의 경우, PEO 고분자로 인해 리튬과 TFSI 음이온의 군집 분포가 [LiTFSI₃]² 형태를 가지는 군집이 억제되고, 리튬 이온의 구조 전이 확산 메커니즘에 크게 기여를 할 수 있는 [LiTFSI₂] 군집이 전해질 내 가장 많이 분포하게 되었다. 양쪽성이온이 도입된 전해질의 경우, 양쪽성이온의 고유한 성질로 인해 이온성 액체기반 전해질의 성능이 향상되었다. 양쪽성이온이 포함된 LiTFSI/PYR₁₄TFSI 전해질에 대해, 리튬 이온 수송에 필요한 활성화에너지의 값이 감소하여 음이온 교환이 활발히 이루어지고 이로 하여금 리튬 이온의 동역학적 물성이 향상되었다. 이런 장점은 일정 농도까지만 효과가 있고 특정 음이온에만 유효하기 때문에, 본 연구에서는 최적의 조건을 제시하였다.

유도쌍극자 모델을 실행하는데에 필요한 많은 컴퓨터 계산량을 극복하기 위해, 상용 소프트웨어인 OpenMM을 개량하였다. 유도쌍극자 모델 실행을 가능하게 하는 OpenMM의 새로운 플러그인을 개발하기 위해 코드 이식을 진행하였고, 이로 인해 정확하고 빠른 편극 분자 모델이 도입된 분자동역학 시뮬레이션 계산이 가능하게 되었다.

주요어: 리튬 이온 전지; 편극성 역장; 분자동역학 시뮬레이션; 이온성 액체; 고분자전해질; 수송 메커니즘

학 번: 2016-21012